

A Study of Wave Induced Electron Precipitation at Low and Middle Latitudes

REINER HANS-WALTER FRIEDEL

Submitted in partial fulfilment of the
requirements for the degree of
Doctor of Philosophy
in the
Space Physics Research Institute
of the
Department of Physics,
University of Natal.

Durban
December 13, 1991

Preface

The work described in this thesis was carried out at the Space Physics Research Institute of the Department of Physics, University of Natal, Durban, Republic of South Africa, from January 1988 to August 1991, under the supervision of Dr. A. R. W. Hughes. Data used for this thesis were recorded at the South African National Antarctic Station SANAE in 1982, and at Durban in 1989 and 1991.

These studies represent original work by the author and have not been submitted in any form to any other university. Where use has been made of the work of others, it has been duly acknowledged in the text.

Acknowledgements

The author wishes to thank the following persons and organisations:

- My supervisor, Dr. A. R. W. Hughes, for introducing me to trimpi events and wave particle interaction work, and for giving me almost unlimited freedom and plenty of support when needed.
- The Space Physics Research Institute, U.R.S.I. and the University of Natal for financial assistance to attend the URSI-WIPP'89 conference in Dunedin, New Zealand, February 1989, the URSI General Assembly in Prague, August 1990 and the IUGG'91 conference in Vienna, Austria, August 1991.
- Members of the S.P.R.I. for assistance, discussions and patience.
- The staff of the Physics Department Electronic Workshop for help with hardware problems (and for helping me keeping my Mini going!).
- Mr. Willhelm de Beer of the Physics Department Mechanical Workshop for all his assistance and help.
- Ms. Terri Holloway for the help in the many battles with various computers and devices.
- The financial support of the F.R.D. for their postgraduate bursary scheme.
- A very special thank you to Queen Esmé for always lending an ear and in general being a ball of fun. Keep the jokes rolling!
- And finally a big hug to Ilse for proofreading the manuscript and providing at least some style. And a thanks to you and Gabriella for putting up with me.

Abstract

Wave induced electron precipitation (WIEP) can modify the ionosphere above a sub-ionospherically propagating VLF signal in such a way as to perturb the amplitude and phase of the signal: The “Trimpi Event”.

In this thesis trimpi events are used in a study of WIEP events and in the responsible mechanism: The gyroresonant interaction. Trimpi activity at middle latitudes (SANAE, Antarctica, $L = 4.02$) and low latitudes (Durban, RSA, $L = 1.69$) together with the corresponding theory for the gyroresonant interaction is examined and compared.

A newly developed computerised system for the detection and analysis of trimpi events has been developed in Durban. This system has been used to analyse tape data recorded at SANAE. Trimpi events were found on various transmitter paths to SANAE and a complete study of 1982 data has led to the establishment of trimpi characteristics as seen at SANAE: an absence of positive events and causative whistlers, a preference for short duration events ($t < 25\text{s}$), the occurrence of some very large events (up to 90% signal attenuation), two minima in occurrence near 0015 and 0400 h Local Time, low occurrence and occurrence rate of events and evidence that interactions with non-ducted whistlers are of importance.

The computerised system was then extended to collect data at Durban simultaneously from up to 20 transmitters worldwide. Examination of data from this survey showed very low occurrence rates of trimpis but yielded some daytime events for which the effectiveness of the gyroresonance interaction, which successfully explains the trimpi event at middle and low latitudes, had to be questioned.

Thus a fully relativistic test particle simulation of the gyroresonant interaction was used to examine the effectiveness of gyroresonance at low L for producing trimpi events. This simulation was run for a wide range of interaction parameters and yielded the following constraints for effective pitch angle scattering (and hence precipitation) of electrons at low L : wave intensities in excess of 150 nT, wave frequencies in excess of 10 kHz and background electron densities at least one order of magnitude higher than normal.

First data from the OMSKI project, a sophisticated VLF receiver operated at Durban as part of an international project, shows further evidence of low-latitude trimpi activity. A survey of one month’s continuous data is presented.

In face of the evidence that trimpi events that occur at low L have the same signature as those at middle L but that the standard gyroresonance interaction is insufficient to cause them, alternate scenarios that could enhance the interaction were sought. In particular distortions in the ambient magnetic field (eg. PC-5 pulsations) were modelled using a new dipole-like background field model. This

simulation showed that distortions which tend to reduce magnetic field curvature along field lines can significantly enhance the gyroresonant conditions and hence the interaction. A new set of conditions for effective gyroresonance at low L is thus established and contrasted with the more lenient conditions at middle L .

A study of “frequency tracking” as a means to prolong resonance showed that natural whistlers do not possess the required frequency/time characteristics for this mechanism, and that artificial waves in a narrow range around the equatorial resonance frequency would be well suited for this purpose.

An overview of the status of worldwide Trimpi detection networks together with the S.P.R.I.’s role in this regard is presented.

Contents

Preface	i
Acknowledgements	ii
Abstract	iii
Contents	v
List of Figures	ix
List of Tables	xiv
1 Introduction	1
1.1 Characteristics of a Trimpi Event	1
1.2 Overall Scenario	2
1.3 Experimental Methods, Analysis and Simulation	5
1.4 Outline of this Thesis	7
1.5 Contributions	7
2 Background	9
2.1 The Magnetosphere	9
2.2 The Physics of the Trimpi Process	11
2.2.1 The Model Magnetosphere	12
2.2.2 Sources of VLF waves	14
2.2.3 The Whistler Mode	14
2.2.4 Dynamics of Radiation Belt Particles	16
2.2.5 The Basic Gyroresonance Interaction	21

2.3	Calculation of Precipitation Fluxes	22
2.4	Ionospheric Response to Electron Precipitation	23
2.5	A Very Complicated Problem	24
2.6	VLF Earth-Ionosphere Propagation	25
2.7	Modelling Trimpi Mechanisms	26
2.7.1	Two Dimensional:“On Path Trimpi”	27
2.7.2	Three Dimensional:“Off Path Trimpi”	28
2.8	History of Trimpi Observation	31
3	Trimpi Events Recorded at SANAE, Antarctica, 1982	33
3.1	Data Source	33
3.2	The Analysis System Hardware	37
3.3	Trimpi Detection	38
3.4	The Occurrence of Trimpi Events	41
3.5	The Causative Whistler	45
3.6	Location of WIEP Regions	47
3.7	Summary of Results	48
4	A System for Receiving Trimpi Events at Durban	50
4.1	The Receiving System	50
4.2	Data Source	52
4.3	Problems	55
4.4	Example of Data	56
4.5	Uses for this System	57
5	Trimpi Events on Low Latitude Paths: Investigation of Gyroresonance at Low L-values	59
5.1	The Relativistic Gyroresonance Condition	60
5.1.1	Derivation of Relativistic Correction	61
5.1.2	Dependence of Resonance Condition on L -value	62

5.2	The Relativistic Equations of Motion	64
5.3	Sample Electron Trajectories	66
5.4	Interaction Parameter Dependence on L -value	68
5.4.1	Calculations for Various B_w	69
5.4.2	Calculations for Various ω_w	70
5.4.3	Calculations for Various n_{eq}	71
5.4.4	“Positive Mode” at Low n_{eq} - a New Result	72
5.5	Lightning as a Wave Source at Low L ?	74
5.6	Discussion	77
6	First Observations of Trimpi Events at Durban using an OMSKI Receiver	80
6.1	The OMSKI System at the S.P.R.I	80
6.2	VLF Signal Paths to Durban	83
6.3	Data Collection	85
6.4	The 27 June – 27 July 1991 Data Set	86
6.4.1	Classic Event Amplitude/Phase Plots	88
6.4.2	Dome Events - a New Type of Trimpi?	89
6.4.3	High Activity Data Subset on NAA	91
6.4.4	Daytime Events	93
6.5	Problems	94
7	The Effect of Magnetic Field Distortions on Gyroresonance at Low L-values	95
7.1	Why Model Ambient Field Distortions?	95
7.2	A New Background Magnetic Field Model	97
7.3	Resonance Condition along a Field Line under the New B -Field Model	101
7.4	Test Particle Simulation Results at $L = 1.7$ under the New B -Field Model	102
7.5	Resonant Frequency along a Field Line	104

8	Conclusion and Future Research	109
8.1	Comparison of Trimpi Activity at SANAE and Durban	109
8.2	Comparison of Gyroresonance at High and Low Latitudes	110
8.3	Future Research	111
8.3.1	Planned Deployment of the S.P.R.I. OMSKI Units	111
8.3.2	The Status of Worldwide Trimpi Networks	112
8.3.3	Other Uses for Trimpi-Nets	114
A	Equations of Motion	117
A.1	Derivation of the Equations	117
A.2	The Relativistic Correction	120
A.3	Interpretation of Terms in Equations of Motion	120
A.4	Total Change in v_{\parallel} and v_{\perp}	121
A.5	Method of solution	122
	Bibliography	123

List of Figures

1.1	A classic amplitude and phase trimpi event observed on 22.3 kHz NWC-Durban Path at 20:39:26 UT on 22/04/91	2
1.2	Cross-sectional view of subionospheric propagation between transmitter and receiver in the presence of a localised precipitation region . . .	3
1.3	Trimpi event scenario	4
2.1	The earth's magnetosphere - general outline	10
2.2	Radial density profile of thermal plasma (Carpenter and Park, 1973)	11
2.3	Particle flux contours in the radiation belts for electron energies greater than 40 keV and 1.6 MeV (Hargreaves, 1979)	12
2.4	Coordinate system for dipole geometry and DE model [Park, 1972] .	13
2.5	Helical locus of the tip of the wave magnetic field vector. The corresponding wave electric field is similar but 90° out of phase such that $\mathbf{E}_w \times \mathbf{B}_w$ is in the direction of k at each point.	16
2.6	Particle motion in a homogeneous static magnetic field	17
2.7	The trajectory of an energetic particle trapped in the earth's magnetic field	18
2.8	Plot of α_{eq}^{lc} as a function of L -value for $h_m = 0, 100, 200, 400$ and 800 km	20
2.9	Spiral motion of whistler and electron about the geomagnetic field. v_p and $v_{ }$ must be opposite and parallel for effective interaction (Hargreaves, 1978)	21
2.10	The computed precipitated energy flux versus time as would be observed in the northern hemisphere after the injection of the impulse wave energy at $t = 0$ in the same hemisphere at $L = 4$.(Figure 6(a) from Chang et al. [1985])	23

2.11	Modified electron density profiles for ionisation enhancement regions resulting from the indicated spectra. Background nighttime exponential profile is for a reflection height of 87 km and electron density gradient of $\beta = 0.47 \text{ km}^{-1}$	24
2.12	Amplitude effects of ionisation enhancement regions on NSS, NAA, NLK and NPM signals at Palmer (Tolstoy et al., [1986]).	29
2.13	Scenario for "Echo Trimpi" (Dowden and Adams [1988])	30
3.1	Great circle paths from VLF transmitters to SANAE	35
3.2	Distribution of the hours of data recorded with respect to observed frequency	36
3.3	Distribution of hours of data recorded with respect to local time of data in 15 min intervals	36
3.4	Analysis System Block Diagram	37
3.5	Trimpi detection template used in automatic trimpi searches	39
3.6	Series of typical trimpi events detected on day 90 on NAA 17.8 kHz signal. Each of the five events was detected by its corresponding template. Obtained from broadband 0–20 kHz data after band pass filtering, rectification and low pass (anti-aliasing) filtering (time constant 0.5 s). Digitised at 5 Hz. Amplitude is in relative units (volts of filter output)	40
3.7	Large trimpi event detected on day 90 on NAA 17.8 kHz signal. Depth 95%, Length 52 s	42
3.8	Distribution of trimpi events. Detection template set to depths between 10–95% for all event lengths	43
3.9	Distribution of trimpi events in local time in 15 min intervals (4 per hour) normalised with respect to total data hours available in each bin	44
3.10	Distribution of number of trimpi events at each observed frequency normalised with respect to data hours available at each frequency	45
3.11	Scenario for a large trimpi event. Here the wave particle interactions are between non-ducted whistler mode waves and energetic electrons, across several L-shells near the equator	46
4.1	Multi-channel computerised VLF receiving system	51
4.2	Spectrum Averager – PC timing and data collection loop	51
4.3	Great circle paths from VLF transmitters to Durban in 1990	54

4.4	Low-latitude transmitter paths to Durban ($L=1.7$, 29°S 32°E) from NWC ($L=1.45$, 22°S 114°E) and La-Reunion ($L=1.36$, 21°S 55°E). Some L-shells in the vicinity of these paths are indicated	56
4.5	Trimpi event observed at Durban on OMEGA signal from La-Reunion. On day 283 (October 10, 1989) at 13:24:24 UT (LT = UT+2hr). The signal (12.3 kHz, Ω La Reunion unique frequency) shows the typical OMEGA on/off modulation (see Figure 6.1)	57
4.6	Example of VLF "Quicklook" data produced with this system. SANA data from 1989 one in five recordings, day 318 from 08:10–12:10 UT. Each panel shows spectra in the 0–8 kHz range. The horizontal lines are fixed frequency calibration signals occurring every minute, with longer bars every 10 min and the longest every hour	58
5.1	Plasma and electron frames of reference	61
5.2	Simple equatorial electron density (n_{eq}) model from satellite observations Carpenter and Smith, 1964, profile III scaled up and down by two orders of magnitude to give five profiles I – V. The curve fit equation used here is $n_{eq} = 10.5 \times 10^4 \times L^{-4.26} \text{cm}^{-3}$ (profile III)	63
5.3	Relativistic resonant velocity (v_r/c , left axis, smooth curves) and total resonant energy (E_k , right axis, dashed curves) as a function of L -value for particles on the loss cone, at the equator. For frequencies 1, 5, 10 and 50 kHz	64
5.4	Single particle trajectory. Change in equatorial pitch angle ($\Delta\alpha_{eq}$, left axis; smooth curve) and % away from resonance ($\epsilon = \frac{ v_{ }-v_r }{v_r} \times 100$, right axis; dashed curve) as a function of geomagnetic latitude θ , distance from equator and interaction time. Particle started at resonance, at the equator. Other interaction parameters shown on the graph	67
5.5	Final pitch angle scattering as a function of initial phase ϕ for the test particle of Figure 5.4. Interaction parameters shown on graph	68
5.6	L -dependence of the RMS $\Delta\alpha_{eq}$ (full lines, right y-axis) and S_L (dotted lines, left y-axis) as a function of wave intensity B_w (50 to 300 pT in 50 pT steps). Also shown are the loss cone angle and resonant energies for the L -values chosen	69
5.7	L -dependence of the RMS $\Delta\alpha_{eq}$ (full lines, right y-axis) and S_L (dotted lines, left y-axis) as a function of wave frequency ω_w (1, 4, 10 and 40 kHz)	70

5.8	<i>L</i> -dependence of the RMS $\Delta\alpha_{eq}$ (full lines, right y-axis) and S_L (dotted lines, left y-axis) as a function of equatorial electron density n_{eq} . The multiplication factors on each graph represent the factors by which the “normal” profile III of Figure 5.2 is scaled	71
5.9	Final pitch angle scattering as a function of initial phase ϕ for the conditions in Figure 5.5. Each graph uses a different multiplication factor for the standard electron density model of Figure 5.2 (Profile III) and plots the curves for several <i>L</i> -values. [a] - positive mode, [d] - “linear” mode, [f] - trapped mode	73
5.10	Peak spheric electric field amplitude as a function of frequency in a 1 kHz bandwidth 10 km from the source (H. Volland, 1982)	75
5.11	Ionospheric penetration losses as a function of frequency for 90 ⁰ magnetic dip for both day and night at 0 ⁰ and 80 ⁰ incidence	75
5.12	Combined source- and transmission spectrum at the top of the ionosphere as a function of frequency normalised to 1 kHz	76
6.1	OMEGA signal transmission format	81
6.2	Frequency response of the OMSKI VLF pre-amplifier	82
6.3	Implementation of the OMSKI system at the S.P.R.I. in Durban	83
6.4	Great circle paths of OMEGA (Table 6.1) and MSK (Table 6.2) stations to Durban on an azimuthal equidistant projection centered on Durban. Stations underlined are used in this study	84
6.5	Signal amplitude (left axis, solid line) and standard deviation (right axis, dashed line) averaged over ten minute bins plotted against universal time for a 24 hour period	85
6.6	Statistics of various event types. All percentages shown are percentage out of total events. The unshaded area refers to classic events, the dotted area to dome events and the hatched area to other events. Each area is further subdivided according to station.	87
6.7	Amplitude/phase plots for classic events observed on NAA, NWC, ARG and LAR	88
6.8	Dome-shaped event observed on NAA-Durban path at 09:04:45 UT on 01 July 1991 (+6.5 dB, -27°, duration 80s)	89
6.9	Amplitude/phase plots for dome events observed on NAA and NWC	90
6.10	OMSKI data for NAA, 02:50–03:20 UT on 13 July 1991. Each panel is individually scaled, amplitude plots have a 2 dB range and phase plots a 20° range	91

6.11	Detailed analysis of active NAA data set. [a] shows the number of events at a range of amplitude perturbations, and [b] the number of events at a range of phase perturbations	92
6.12	Distribution of events in UT for the 27 June – 27 July dataset. The dark bars show the distribution excluding the high activity period on NAA, which is shown superimposed with the dotted bars	94
7.1	Plot of $r = r_o \cos^\mu \theta$ at $L = 2$	98
7.2	Variation of B along a field line normalised with respect to B_{eq} as a function of latitude for a range of new field parameter μ	99
7.3	Variation of $\frac{db}{Bdl}$ along a field line (normalised with respect to B) as a function of latitude for a range of new field parameter μ	100
7.4	Resonance condition ϵ along a magnetic field line as a function of latitude for $L = 1.2$ [a] and $L = 2.0$ [b] for various values of new field parameter μ . The dipole case $\mu = 2$ lies between the curves for $\mu = 1.5$ and $\mu = 2.5$	101
7.5	Plot of change of equatorial pitch angle as a function of ϕ_0 for various values of new field parameter μ	103
7.6	μ -dependence of the RMS $\Delta\alpha_{eq}$ (full line, right y-axis) and S_L (dotted line, left y-axis)	104
7.7	Local resonant frequency as a function of geomagnetic latitude. The top x-axis shows electron travel time with $t = 0$ at the mirror point in the southern hemisphere (non-linear scale). Numbers correspond to numbers in figure 7.8	105
7.8	Frequency/time format of the required input wave in the northern hemisphere to be in resonance with the electron of figure 7.7. The solid curve is plotted against the left y-axis showing the frequency of the wave, and the dashed curve against the right y-axis, showing at which latitude that frequency is resonant. $t = 0$ at electron mirror point in southern hemisphere. Numbers correspond to numbers in figure 7.7	106
8.1	Great circle paths of the various world-wide trimpi networks. The network planned by the S.P.R.I. includes the stations Durban, Marion Is., Gough Is., and SANAE	115
A.1	Coordinate system for the equations of motion. The z-axis is everywhere aligned with the magnetic field	118
A.2	Coordinate system for the orbit of an electron in the x-y plane	119

List of Tables

2.1	Amplitude change codes for Figure 2.12	28
3.1	List of VLF transmitters observed at SANAE in 1982	34
4.1	Maximum spectrum rates available for different averaging settings	52
4.2	List of VLF/LF transmitters observed at Durban in 1990	53
5.1	Variables influencing gyroresonance	60
6.1	OMEGA transmitting stations	81
6.2	OMEGA and MSK stations as seen at Durban	84
6.3	Classification of events for the 27 June – 27 July data set	86
7.1	List of parameters used for new <i>B</i> -field test particle simulation	102
8.1	Sites for the planned S.P.R.I. net of trimpi receivers	112

Chapter 1

Introduction

In this chapter a broad overview of wave induced electron precipitation (WIEP) with the resulting trimpi phenomenon and the physical processes involved is given. The remainder of this thesis is outlined and the main achievements of this work are summarised.

1.1 Characteristics of a Trimpi Event

Trimpi events are perturbations of signals propagating in the earth-ionosphere waveguide. They have been observed on frequencies from 3 kHz to 800 kHz, and are characterised by a sudden change of the received amplitude and/or phase, with onset times of typically 1–5 seconds, followed by a recovery to pre-disturbed values over a period of 10–100 seconds. These changes in signal amplitude and phase may be positive or negative, in any combination, and do not necessarily accompany each other. A typical trimpi signature is shown in Figure 1.1.

Amplitude changes of up to 15 dB and phase changes of up to 10° , with occurrence rates as high as 80 per hour have been observed on a variety of transmitter signals at stations all over the world in the middle to high latitude regions.

Trimpi events are almost exclusively seen at times of local darkness and when most of the transmission path to the receiver is darkness, and in the recovery period after a magnetic storm. The characteristic “Trimpi behaviour” of a specific signal path and frequency is normally unique. Trimpi events have been linked to whistlers observed at about the same time as the onset of the event, suggesting a wave-particle interaction mechanism. The gyroresonance interaction between whistler-type waves and particles has become the accepted mechanism causing trimpi events.

For further details on trimpi observation history refer to section 2.8.

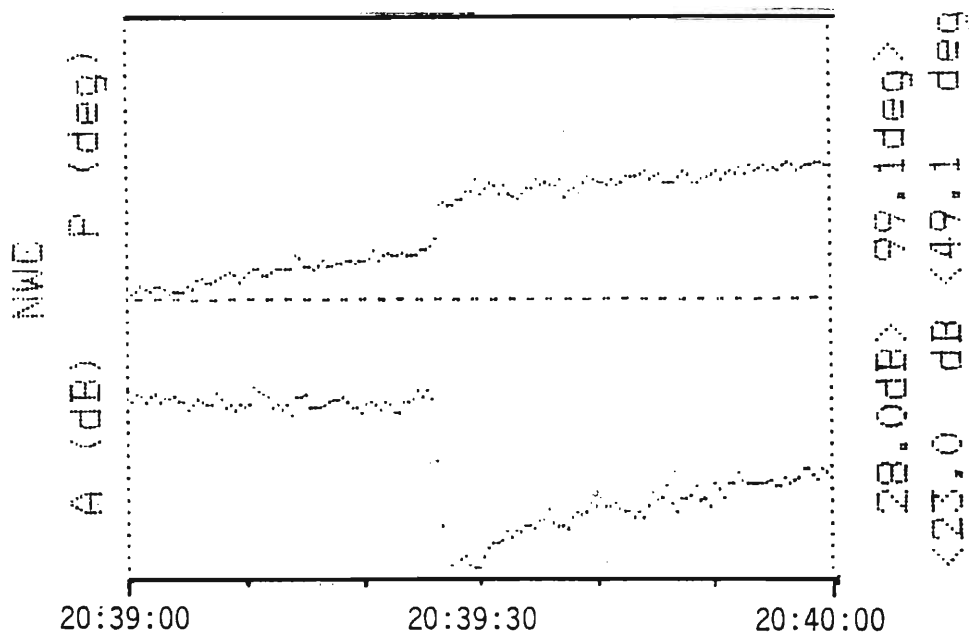


Figure 1.1: A classic amplitude and phase trimpi event observed on 22.3 kHz NWC-Durban Path at 20:39:26 UT on 22/04/91

1.2 Overall Scenario

Wave-particle interactions are of general interest in plasma physics. Through these mechanisms significant amounts of energy and momentum can be transferred between particles and waves, leading to either wave growth and particle scattering, or wave attenuation and particle acceleration. In space plasmas, where energetic particles are confined by the geometry of earth's dipole magnetic field to the radiation belts of the inner magnetosphere, such an interaction may alter the dynamics of some particles in such a way that they are no longer confined and are lost from the radiation belts, precipitating into the ionosphere and giving rise to trimpi events.

Wave-particle interactions in the inner magnetosphere involve resonances between electromagnetic waves and energetic radiation belt particles. The interaction is believed to be most effective near the geomagnetic equator.

Once particles are lost from the radiation belts and are deposited in the ionosphere they form a patch of enhanced ionisation which locally alters the properties of the earth-ionosphere waveguide. This patch dissipates as a result of recombination as the ionosphere returns to equilibrium.

The amplitude and phase of a received VLF signal can be thought of as the sum of several modes travelling in the earth-ionosphere waveguide (Figure 1.2). For simplicity the diagram shows only two dimensions, although the perturbation is in general three dimensional and need not necessarily lie on the transmitter path. A localised disturbance in the waveguide can alter the existing mode patterns or introduce new modes and thus alter the amplitude and phase of the signal at the

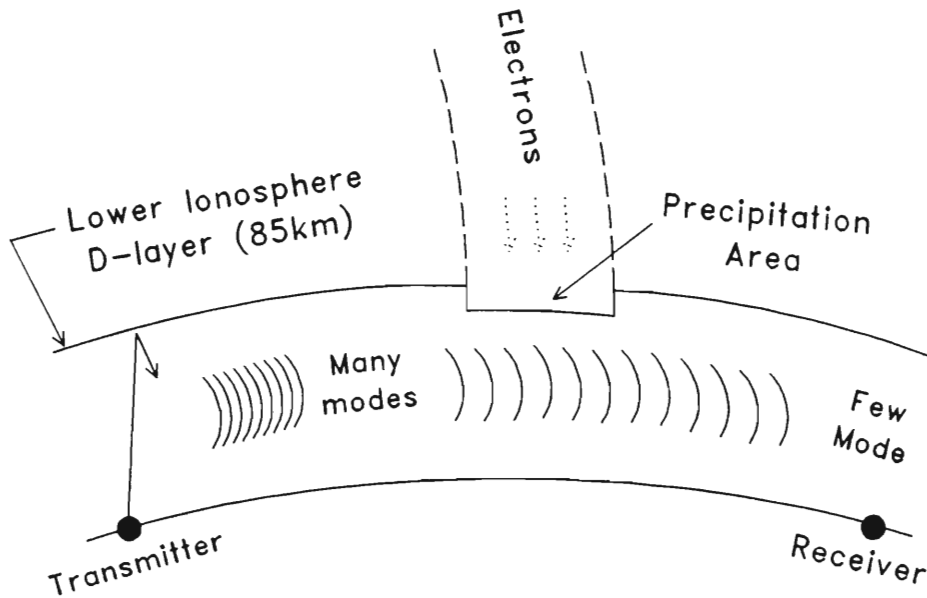


Figure 1.2: Cross-sectional view of subionospheric propagation between transmitter and receiver in the presence of a localised precipitation region

receiver, giving rise to a trimpi event.

In the generally accepted view the chain of events leading to a trimpi event is as follows (Figure 1.3):

A source of electromagnetic waves (a lightning strike, or VLF transmitter) near one end of the a field line leads to a magnetic field aligned wave travelling towards the equatorial plane. In that region the wave interacts with counter streaming energetic electrons and scatters some of these into the losscone of the geomagnetic mirror such that they are lost from the radiation belts and are precipitated into the ionosphere. The VLF wave propagating beneath the area where the electrons precipitate is affected giving rise to the typical trimpi signature observed at receiver R.

This chain of events can thus be split into several separate processes:

- (a) The injection of a wave train into the magnetosphere
- (b) The wave particle interaction
- (c) Electron precipitation into the ionosphere causing enhanced ionisation thus modifying the earth-ionosphere waveguide
- (d) The effect of the modified waveguide on the VLF signal propagating in it leading to a trimpi signature at the receiver.

Part A depends on the types of sources available (lightning, transmitters, power

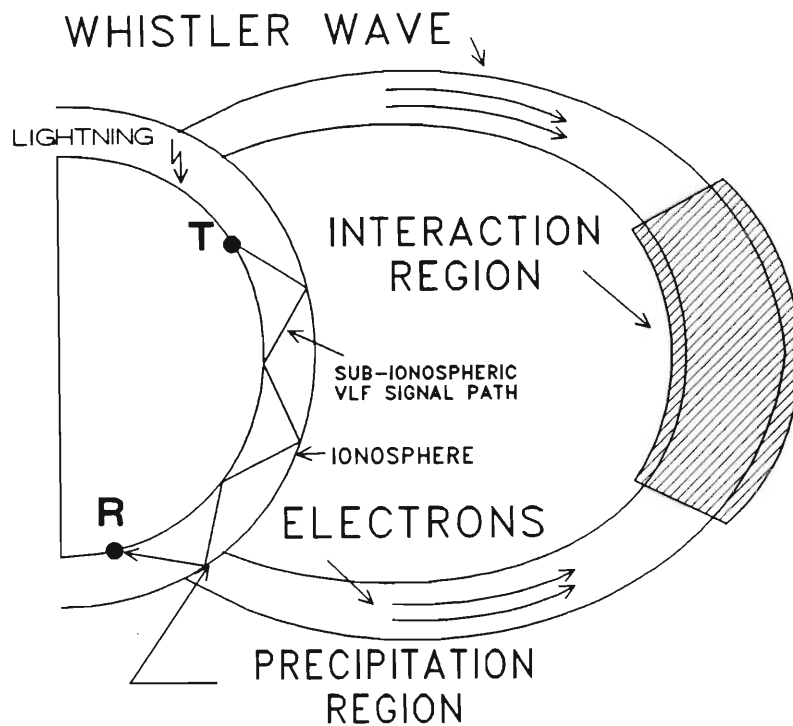


Figure 1.3: Trimpi event scenario

grids, natural VLF such as discrete chorus and hiss) and on the coupling mechanism into the ionosphere.

Part B depends on the properties of the local environment, in particular the geometry and strength of the magnetic field, the energy and distribution of the electron population, and the wave spectrum as a function of time as determined in part A. From that knowledge a time series of the energy spectrum of the precipitated electrons can be calculated.

Part C depends on the particular state of the ionosphere which is in general a function of height, local time and geographic position. In particular the ionisation, recombination, diffusion and drift time constants, and the composition of the ionosphere needs to be known to predict the size and depth of the ionisation patch caused by the precipitating electrons as given by Part B.

Part D depends on the VLF propagation characteristics of the earth-ionosphere waveguide, which in turn is unique for different signal paths, and the way it is altered under the disturbance as found in part C. Furthermore the location of the ionisation path with respect to the signal path and the receiver is crucial in determining the type of event which is observed.

1.3 Experimental Methods, Analysis and Simulation

An important step in understanding in detail this chain of events is to obtain some idea of the size, location and dynamics of these precipitation patches and to obtain some statistics on the types of events caused by them. This thesis attempts to answer these questions with regard to observations made at SANAE in 1982.

At the heart of the trimpi event scenario lies the gyroresonant interaction. This thesis reports on trimpi events observed at low latitudes (Durban) and examines the interaction in detail for the case of low latitude events, to establish the conditions for effective interactions in the inner radiation belts.

The projects for this thesis were started from scratch, with no instruments or methods for identifying trimpi events in existence at the Space Physics Research Institute in Durban. The first task was therefore to develop a system to extract data in a meaningful way from existing VLF recordings, and then to search for trimpi events in this data.

Since it was envisaged that a large volume of data would be handled, the choice was made to computerise the whole system, both for data acquisition and further analysis. The system should have one input : the audio data tape; and one output: a computer file containing all the information on any trimpi event detected in the data.

The system developed here enables one to obtain the digital time series of the amplitude only for a selected VLF station frequency as recorded at SANAE. It was not possible to obtain signal phase as well since no reliable reference phase signal was recorded with the existing data.

Using this system a broad database from 1982 SANAE recordings was established. Further digital methods for analysing this database were developed, including a trimpi search routine to automatically detect and record different types of trimpi events. In this way some basic statistics regarding the occurrence of trimpi events at SANAE were established.

In order to find the location and size of precipitation patches, a simple geometrical method was used. Assuming that precipitation patches affect only signal paths beneath them or very close to them (ignoring the effect of so called "echo trimpis" [Dowden and Adams, 1989]), the presence or absence of events on adjacent paths given some indication of position and size of the patch. Since events are known to occur in the night-time D-layer only [Leyser et al, 1984] the day/night terminator at D-layer heights (80 km) further limits the possible location of the precipitation patch. Finally, since whistlers have been firmly linked with trimpi events, the precipitation will occur along the same field aligned duct which guides the whistler. The L-value of the accompanying whistler then yields a line of geomagnetic lat-

itude (at D-layer heights) along which the field aligned electrons precipitate. Direction finding techniques could be used to find the whistler duct exit point, however the data used here was not recorded with a goniometer system. These lines are then plotted onto a projection of the area around SANAE, and serve to demarcate the area of the precipitation. Depending on the actual geometry the location of the precipitation patch may be estimated and some dimensional limits may be imposed onto the size of the patch.

From a survey of accompanying VLF broadband data some information is gained on the type of electromagnetic wave responsible for the wave particle interaction which lead to the trimpi event. In particular the presence or absence of nearby whistlers yields information on whether the interaction took place with ducted or non-ducted waves, whereas the level of broadband hiss is indicative of the general level of waveparticle interaction activity in the magnetosphere.

This trimpi detection system was extended to enable “live” data collection at Durban. A VLF antenna/preamplifier system was established on the Physics Department roof connected to a spectrum analyser and averager which was interfaced to a personal computer, creating in effect a computer controlled multi-channel receiver. Up to 20 stations were simultaneously logged (amplitude only) using this system and a small database of trimpi activity at Durban was established. Occurrence of events is low at Durban, but include some daytime events, which indicates very high energy precipitation.

To establish whether the gyroresonance mechanism “works” at Durban latitudes a fully relativistic test-particle simulation of the gyroresonance interaction was employed. Building on existing work [Inan et al., 1978], [Inan et al., 1982] and [Chang and Inan, 1983], [Chang and Inan, 1985] the simulation was extended to cover high energy electrons at extremely low L ($L = 1.2 - 2.0$) and the parameters needed for a strong interaction were sought. This study yielded basic unfavorable conditions for gyroresonance interactions at low L.

At the same time the existing Durban trimpi receiver was “modernised”. The S.P.R.I. joined an international net of receivers of the OMSKI-type (Omega and MSK Instrument), build by the University of Otago in New Zealand. This is a joint project between Dick Dowden, Dept. of Physics at Otago and Andy Smith of the British Antarctic Survey. This new receiver is capable of tracking the OMEGA signal pattern and can demodulate the American Navy MSK signals to provide both amplitude and phase information. This thesis reports on the first observations and trimpi statistics obtained with this system.

In a final study enhancements of the gyroresonance interaction were sought to explain the growing evidence of “typical” trimpi events at low L, as observed at Durban. A new magnetic field model for the earth was developed which enables modelling of various background field distortions such as are present in the real magnetosphere (e.g. dayside compression, cavity mode oscillations, pc4 – pc5 pulsations). Incorporating this model into the test particle simulation of the interaction, new conditions for “strong” gyroresonance interactions are derived.

1.4 Outline of this Thesis

In the previous sections a broad overview of the processes involved in trimpi work were given together with type of research attempted in the current work.

The remainder of the thesis is organised as follows :

Chapter 2 describes the basic background knowledge required for this work. A brief outline of magnetospheric physics is followed by a more detailed account of the physics involved in the chain of processes leading to a trimpi event. Also included is an account of the history of trimpi observations, and previous work done in this field to understand and model the mechanisms involved.

Chapter 3 deals with the equipment designed to extract trimpi data from existing VLF recordings and presents a survey of 1982 SANAE data.

Chapter 4 describes the trimpi receiver developed for live data capture at Durban and presents the results of a brief survey of Durban data.

Chapter 5 deals with the gyroresonance interaction in detail, leading up to a fully relativistic test particle simulation of the interaction and presents the results of this simulation at low L.

Chapter 6 describes the new joint OMSKI-net project which was started at Durban in April 1991. The results of one month's continuous operation are presented with first statistics of trimpi activity at Durban.

Chapter 7 extends the test particle simulation of chapter 5 to include a new dipole-like magnetic field model which enables one to model magnetic field distortions and their effect upon the gyroresonance interaction.

Chapter 8 summarises the work done and compares the results obtained here for low L (Durban) trimpi events with previous studies and the results from SANAE. Suggestions for further research are made, in particular with regard to world-wide trimpi networks and their use for other related research topics.

1.5 Contributions

The main achievements are as follows:

- (a) A complete data acquisition and analysis system to detect and extract trimpi events from existing Sanae data was set up and used for a survey of 1982 SANAE data
- (b) The analysis system used here was presented in a paper at the 34th SAIP conference in Grahamstown, July 1988

- (c) The first results of a survey of 1982 SANAE data were presented at the URSI WIPP'89 conference in Dunedin, New Zealand, February 1989
- (d) The outline of the new OPAL/OMSKI project was presented in a paper at the 35th SAIP conference in Pretoria, July 1989
- (e) The complete results of the 1982 SANAE data survey were published in a paper [Friedel and Hughes, 1990], "Characteristics and frequency of occurrence of trimpi events recorded during 1982 at SANAE, Antarctica", *Journal of Atmospheric and Terrestrial Physics*, Vol.52, No.5, pp329-339, May 1990
- (f) A new computer controlled multi-channel receiver and VLF antenna system was set up at Durban and used for data capture at Durban. This system has consequently been used for the generation of "Quicklook" VLF spectrogram data [Friedel and Smith, 1991]
- (g) A paper on the investigation of gyroresonance at low L-values was presented at the XXIII General Assemble of URSI in Prague, Czechoslovakia in September 1990
- (h) A paper entitled "Trimpi events on low latitude paths - an investigation of gyroresonance at low L-values" has been submitted to *Journal of Atmospheric and Terrestrial Physics* for publication
- (i) The first of two OMSKI receivers has been set up in Durban in April 1991 as part of an international joint project. The second receiver is due in Durban at the end of 1991 and will be sent to SANAE at the end of 1992.
- (j) A paper on the effect of magnetic field distortions on gyroresonance at low L-values was presented at the XX General Assembly of IUGG (IAGA) in Vienna, Austria in August 1991
- (k) A poster on the data of the first month of continuous operation of the OMSKI receiver at Durban was presented at the XX General Assembly of IUGG (IAGA) in Vienna, Austria in August 1991
- (l) The last two items are also in preparation for publication

Chapter 2

Background

2.1 The Magnetosphere

The magnetosphere surrounding the earth is a region of space contained within an outer layer, a boundary called the magnetopause, that separates the interplanetary magnetic field from earth's geomagnetic field. The supersonic solar wind interacts with the dipole-like geomagnetic field and gives the magnetosphere its large scale structure as shown in Figure 2.1.

In the sunward direction the field is compressed by the solar wind and extends out to about $10 R_e$ (earth radii). In the anti-sunward direction the field is drawn out into a long tail extending several hundred R_e . At high latitudes (above approximately 75° geomagnetic latitude) the field lines extending into the magnetotail do not close back onto the earth. The wave particle interaction under consideration in this thesis occurs on closed field lines. Consequently the description of the magnetosphere in this thesis is limited to that region. The inner boundary of the magnetosphere is taken approximately 100 km above the surface of the earth (the level of the ionosphere) [Lyons and Williams, 1984].

The inner magnetosphere can be approximated by a distortion free dipole (see Section 2.2.1) field and is roughly defined by geomagnetic field lines with $L < 6$ (lines which cross the geomagnetic equator at a distance of less than 6 earth radii). The magnetoplasma in this region is composed of electrons and ions of a wide energy range, which falls broadly into two groups, a cold "thermal" background plasma and a hot "energetic" plasma.

The thermal plasma consists of particles with energies in the range 0.1–1 eV and originates in the upper layer (the F-region) of the ionosphere from where it diffuses upwards along magnetic field lines. The thermal plasma density decreases with radial distance from the earth until a sharp decrease in plasma density occurs at the plasmopause [Carpenter, 1963] where the density drops by as much as two orders of magnitude over a distance of $< 2 L$. Plasmopause location varies from 2–7 L depending on geomagnetic activity [Carpenter and Park, 1973]. A typical

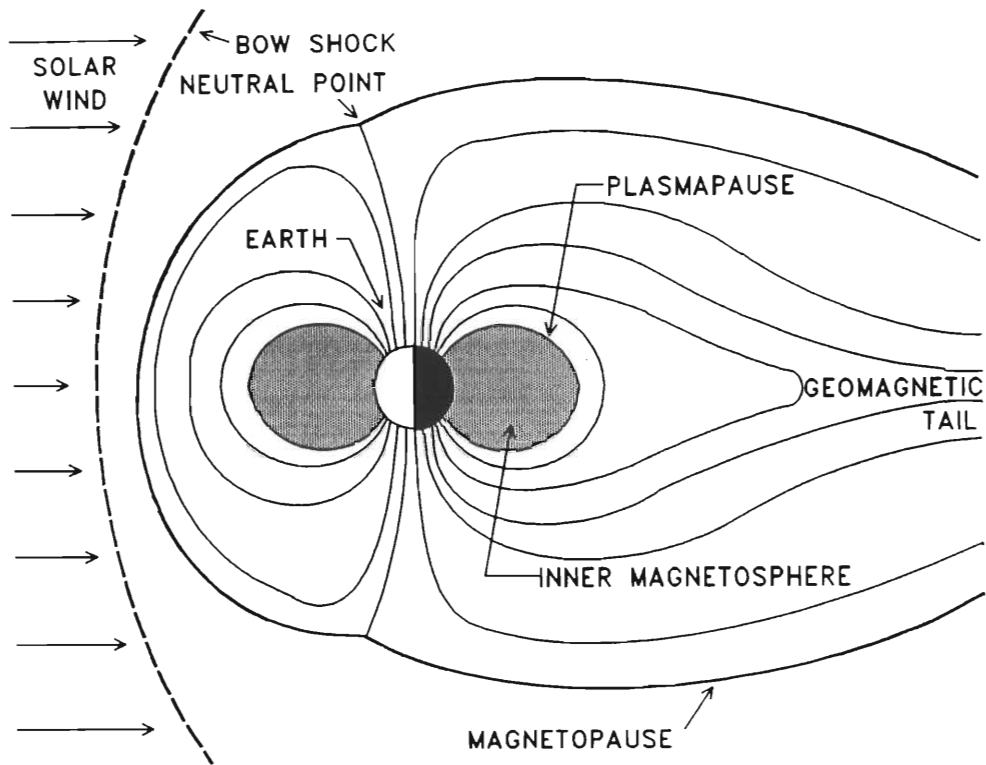


Figure 2.1: The earth's magnetosphere - general outline

density profile is shown in Figure 2.2.

In addition to thermal particles the magnetoplasma in the closed field line region includes the Van Allen radiation belts - electrons and ions in the energy range of 10 keV–100 MeV. These particles are trapped in the magnetic mirror formed by the geometry of earth's dipole field. Particle fluxes maximise in two regions known as the inner and outer radiation belts [Hargreaves, 1979]. Inner belt fluxes peak inside an equatorial distance of $2 L$ and are quite stable. The outer belt fluxes peak near the plasmopause during geomagnetically quiet conditions but during magnetic storms both the outer belt electrons and the plasmopause move towards the earth [Lyons and Thorne, 1973]. Figure 2.3 shows the distribution of trapped electrons at two energies.

The trajectory of a given particle in this region of the magnetosphere can be described as a superposition of three simple motions: a gyromotion of the particle around the field line, a bounce motion along the field line between hemispheres, and a drift motion around the earth. The theory of particle motion in the earth's magnetic field is well developed and described in many textbooks eg. [Hargreaves, 1979, Schulz and Lanzerotti, 1973]. An outline of the dynamics is given in Section 2.2.4.

Particle-particle collisions are rare in the radiation belts. Particles are lost by interaction with the ionosphere at either end of their bounce if they penetrate

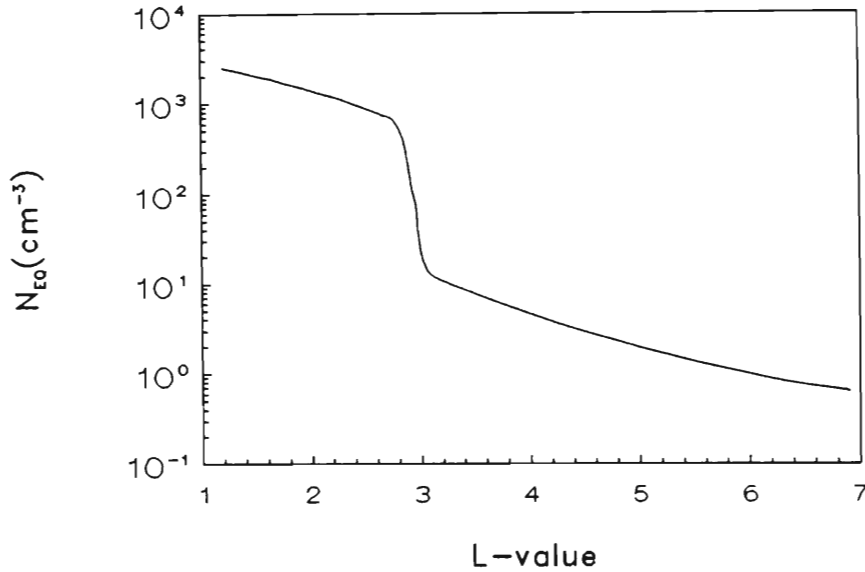


Figure 2.2: Radial density profile of thermal plasma (Carpenter and Park, 1973)

too low before being mirrored. Their mirroring height is a function of equatorial pitch angle (the angle between the particle's velocity vector and the direction of the magnetic field at the geomagnetic equatorial plane). This leads to the concept of a loss cone, a range of pitch angles from which particles are lost because they mirror too low. Particles would remain outside the loss cone indefinitely (ie. remain trapped) in the absence of any other scattering processes. Interactions with plasma waves thus provide an important mechanism for scattering and loss of radiation belt particles.

A variety of plasma wave modes are supported in the magnetosphere. The observed modes and characteristic spectrum varies considerably with location, due to the spatial variations in magnetic field strength and plasma density. The plasmapause tends to be an important dividing boundary for distinctly different wave activity [Carpenter et al., 1968]. The type of wave of importance to this thesis is the whistler mode wave which is further described in Section 2.2.3.

2.2 The Physics of the Trimpi Process

In this section the underlying physical processes and environmental conditions as introduced in section 1.2 are examined in detail. Refer to figure 1.3.

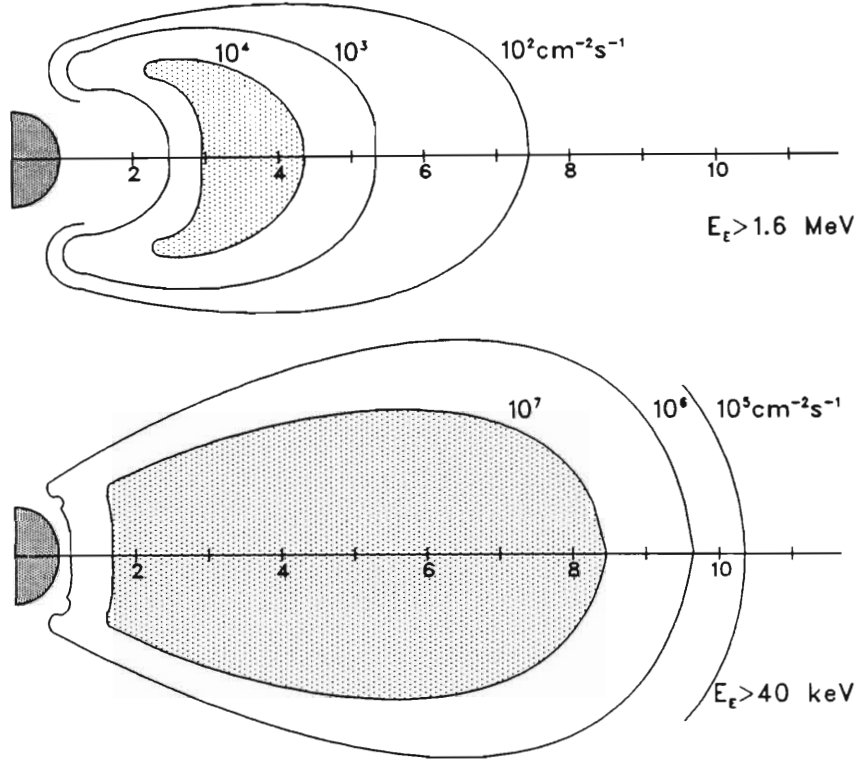


Figure 2.3: Particle flux contours in the radiation belts for electron energies greater than 40 keV and 1.6 MeV (Hargreaves, 1979)

2.2.1 The Model Magnetosphere

In the inner magnetosphere the earth's magnetic field is well approximated by a centred dipole inclined at about 11° to the axis of rotation. The expression for the magnetic field strength then becomes

$$B_o = 0.312 \times 10^{-4} \left(\frac{R_o}{R} \right)^3 (1 + 3 \sin^2 \lambda)^{\frac{1}{2}} \frac{\text{wb}}{\text{m}^2} \text{ Tesla} \quad (2.1)$$

where λ is the geomagnetic latitude, R is the geocentric distance and R_o is the mean diameter of the earth (6370 km). Figure 2.4 shows the dipole geometry and the symbols commonly used.

Field lines in any meridional plane can be uniquely identified by McIlwain's parameter L which for a dipole field can be written as

$$L = \frac{R_{eq}}{R_o} = \frac{1}{\cos^2 \lambda_o} \quad (2.2)$$

where R_{eq} is the distance from the center of the earth to the apex of the field line, which for a dipole field is at the magnetic equator.

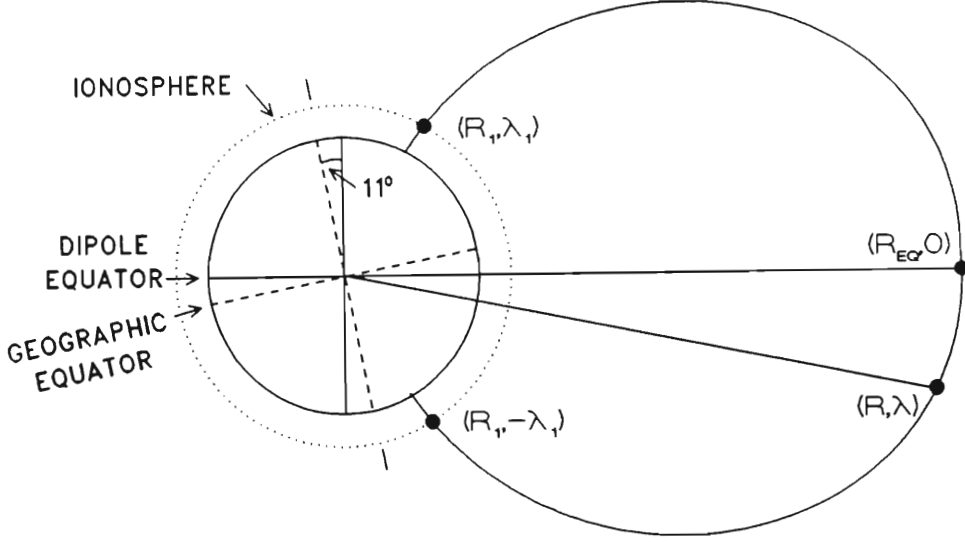


Figure 2.4: Coordinate system for dipole geometry and DE model [Park, 1972]

As far as the distribution of cold plasma along the field lines of the inner magnetosphere is concerned, a diffusive equilibrium model [Angerami and Thomas, 1964] which takes account of the influence of the earth's gravitational and centrifugal forces can be used. In this model the neutral isothermal mixture of electrons and positive ions is in diffusive equilibrium along magnetic field lines. The electron density can then be expressed as [Park, 1972]:

$$\begin{aligned}
 n_e &= n_1 \left[\sum_i c_i \exp \left(-\frac{z_G}{H_i} \right) \right]^{\frac{1}{2}} \\
 z_G &= R_1 - \frac{R_1^2}{R} - \frac{\Omega^2}{2g_1} (R^2 \cos^2 \lambda - R_1^2 \cos^2 \lambda_1) \\
 H_i &= \frac{k_b T_p}{m_i g_1}
 \end{aligned} \tag{2.3}$$

where c_i is the fractional abundance of the ionic species, n_e is the electron density, R is the geocentric distance, Ω is the angular velocity of the earth, g is the acceleration of gravity, λ is the dipole latitude, k_b is Boltzman's constant, m_i is the ionic mass and T_p the plasma temperature. Subscript i refers to the i th ionic species and subscript 1 refers to a reference altitude of 1000 km. The geopotential height z_G includes the variation of gravitational and centrifugal forces with distance. Equations 2.4 refer to a simplified version of the diffusive equilibrium model in which the electron and ion temperatures are equal ($T_i = T_e$) and do not change along the field line [Angerami and Thomas, 1964]. This model breaks down at high latitudes and outside the plasmopause.

2.2.2 Sources of VLF waves

Part of the chain of events leading to a trimp event is the interaction of a VLF wave with energetic particles. For this interaction to be effective (see Section 2.2.5) waves and particles have to move along the same field line for some length of time, which limits the type of VLF waves that can partake in this interaction to waves which for a significant part of their propagation are field aligned: an important class of waves satisfying this condition are so called “whistler mode” waves. Whistlers are generally thought to travel along field-aligned density enhancements in the magnetosphere called “ducts”. The theory of ducted propagation is not fully established but there is a large volume of experimental data which is well explained by such propagation [Helliwell, 1965]. The trimp event is transient, caused by a shower of precipitation over a period of one to three seconds, which indicates an interaction with a brief burst of VLF activity. In order for the precipitation to affect sub-ionospheric VLF signals a large number of electrons need to precipitate. However each whistler mode frequency interacts with only a small range of energies of electrons, so that a broad frequency pulse is needed. These conditions are best met by whistlers, although some other discrete VLF emissions might have the right spectral characteristics, such as discrete chorus.

Trimpis have mostly been associated with whistlers [Helliwell et al., 1973], although associations with other types of natural emissions have been reported [Hurren et al., 1986]. However an absence of an associated whistler is no guarantee that the event was caused by a different type of emission, since there are many possible reasons for a whistler not being observed at a particular station (see Section 3.5).

Whistlers originate in natural lightning, and the intensity variations with frequency of most whistlers are controlled largely by the spectrum of the strike [Helliwell, 1965]. The actual source is difficult to identify because of the relative abundance of atmospherics, and the fact that whistler mode energy may enter the magnetosphere as far as several hundred kilometres from the actual strike. Using a lightning detection and direction finding network it has been shown that trimp events occur within $\approx 150\text{km}$ of the lightning discharges [Inan et al., 1988b].

Other types of emissions are generated by wave-particle instabilities in the magnetosphere and their origin is very difficult to determine. The generation region is likely to be near the magnetic equator since wave growth maximises at low B [Kennel and Petschek, 1966].

2.2.3 The Whistler Mode

For the magnetospheric environment the medium can be considered homogeneous, ie. the medium varies slowly over several wavelengths, and the collision frequency is small.

The dispersion relation for electromagnetic waves in a cold, collisionless, homo-

geneous, infinite plasma with a homogeneous static magnetic field \mathbf{B}_0 is given by the well-known Appleton-Hartree equation [Ratcliffe, 1959]:

$$n^2 = 1 - \frac{\frac{\omega_p^2}{\omega^2}}{1 + \frac{\omega_H^2 \sin^2 \theta}{2(\omega_p^2 - \omega^2)} \mp \left[\left(\frac{\omega_H^2 \sin^2 \theta}{2(\omega_p^2 - \omega^2)} \right)^2 + \frac{\omega_H^2}{\omega^2} \cos^2 \theta \right]^{\frac{1}{2}}} \quad (2.4)$$

where n is the refractive index, ω_p is the electron plasma frequency, ω_H is the electron gyrofrequency, ω is the wave frequency and θ is the angle between the wave normal and the magnetic field vector. The two characteristic waves, corresponding to the two signs before the square root, are elliptically polarised. The minus sign corresponds to the *whistler mode* and the *R* wave at frequencies above the *R*-cut off. Both phase and group velocities of whistler mode waves are below the vacuum velocity of light, while for the *R* wave they are above the vacuum velocity of light. Equation (2.4) simplifies considerably when it is assumed that $\mathbf{k} \parallel \mathbf{B}_0$ (i.e. θ in 2.4 = 0, the "longitudinal approximation"). Exact longitudinal propagation is unlikely to occur, but in the light of the duct theory of whistler propagation [Smith, 1961] it is a reasonable approximation. Under this assumption (2.4) becomes

$$n^2 = 1 - \frac{\frac{\omega_p^2}{\omega^2}}{1 - \frac{\omega_H}{\omega}} \quad (2.5)$$

In the inner magnetosphere $\omega_p^2 \gg \omega_H^2$ and for $\omega < \omega_H$ we can rewrite (2.5)

$$n = \frac{kc}{\omega} \cong \omega_p \left[\frac{1}{\omega(\omega_H - \omega)} \right]^{\frac{1}{2}} \quad (2.6)$$

where c is the speed of light and k is the wave number in the medium. Other useful expressions that can be derived from (2.6):

$$k = \frac{\omega_p}{c} \left(\frac{\omega}{\omega_H - \omega} \right)^{\frac{1}{2}} \quad (2.7)$$

$$v_p = \frac{\omega}{k} = c \frac{\omega^{\frac{1}{2}} (\omega_H - \omega)^{\frac{1}{2}}}{\omega_p} \quad (2.8)$$

$$v_g = \frac{d\omega}{dk} = 2c \frac{\omega^{\frac{1}{2}} (\omega_H - \omega)^{\frac{3}{2}}}{\omega_p \omega_H} \quad (2.9)$$

where v_p is the phase velocity and v_g is the group velocity. The whistler mode waves are right-hand circularly polarised (for $\theta = 0$ only) and the wave field vectors rotate in the same sense as the electrons. This together with the low phase velocity of the waves makes it possible for them to resonate with particles

such as electrons. Both the wave electric and magnetic fields are transverse to \mathbf{B}_0 . The wave vectors traverse a helix as shown in Figure 2.5.

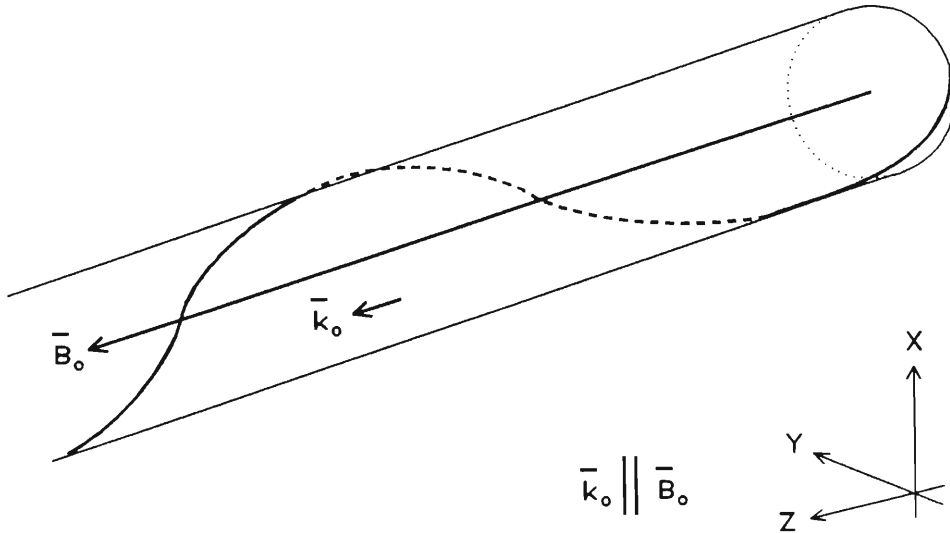


Figure 2.5: Helical locus of the tip of the wave magnetic field vector. The corresponding wave electric field is similar but 90° out of phase such that $\mathbf{E}_w \times \mathbf{B}_w$ is in the direction of k at each point.

The magnetic medium is inhomogeneous, but since the variations in ω_H and ω_p within the space of one wavelength are negligible, the W.K.B. approximation [Budden, 1961] can be used and the wave fields can still be expressed as progressive waves as follows:

$$\begin{aligned} \mathbf{B}_w &= B_w \left[\mathbf{a}_x \cos(\omega t - \int_0^z k dz) + \mathbf{a}_y \sin(\omega t - \int_0^z k dz) \right] \\ \mathbf{E}_w &= \frac{\omega}{k} B_w \left[\mathbf{a}_x \sin(\omega t - \int_0^z k dz) - \mathbf{a}_y \cos(\omega t - \int_0^z k dz) \right] \end{aligned} \quad (2.10)$$

2.2.4 Dynamics of Radiation Belt Particles

Motion of charged particles in a static magnetic field

In a static magnetic field the motion of a charged particle is the superposition of its motion parallel to the field (v_{\parallel}) and its gyration in the plane perpendicular (v_{\perp}) to the magnetic field. This motion is thus a helix as shown in Figure 2.6.

The gyrofrequency ω_H , the gyroradius r_H and gyroperiod T_H are given by

$$\omega_H = \frac{|q| B_0}{m}; \quad T_H = \frac{2\pi}{\omega_H}; \quad r_H = \frac{mv_{\perp}}{qB_0} = \frac{mv \sin \alpha}{qB_0} \quad (2.11)$$

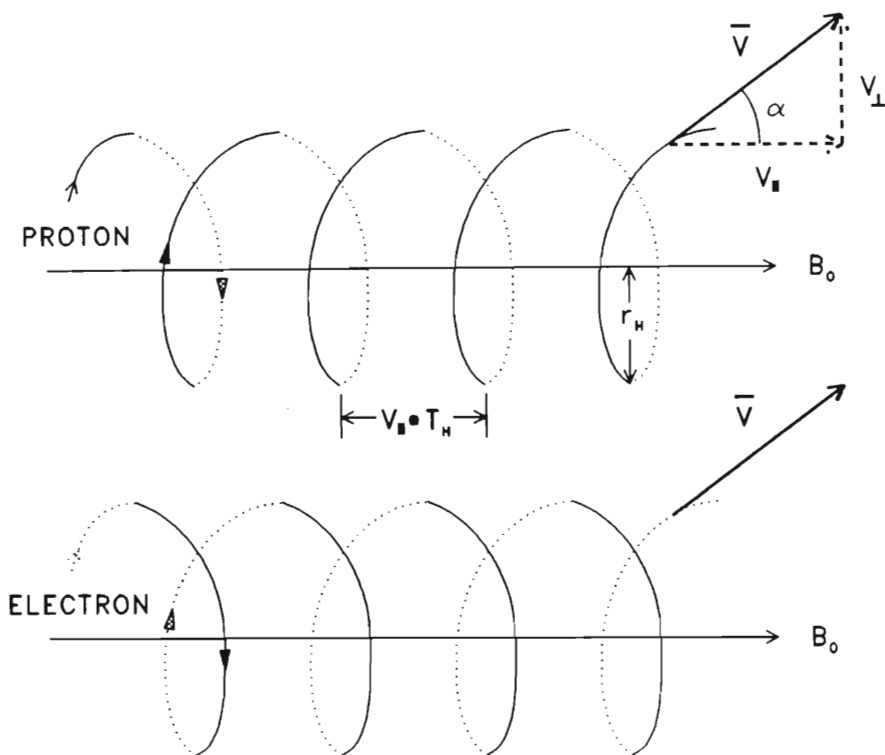


Figure 2.6: Particle motion in a homogeneous static magnetic field

where $\alpha = \tan^{-1}(v_{\perp}/v_{\parallel})$ is the pitch angle of the particle. The force on the charged particle is perpendicular to its motion $q(\mathbf{v} \times \mathbf{B}_0)$ and the direction depends on the sign of q . Electrons and protons thus gyrate in opposite directions as shown in Figure 2.6. This force can do no work on the particle, and the total kinetic energy ($1/2 mv^2$) is conserved along the trajectory. For a spatially changing magnetic field such as the earth's this implies that the particle orbit, given by ω_H and r_H , must adjust in such a way as to conserve total kinetic energy - i.e. the magnetic flux linking the orbit is constant, hence

$$\text{Flux} = B_0 r_H^2 = B_0 \left(\frac{mv \sin \alpha}{qB_0} \right)^2 = \text{constant} \quad (2.12)$$

Since energy is conserved, v is constant, and one can write

$$\frac{\sin^2 \alpha}{B_0} = \frac{v_{\perp}^2}{B_0} = \mu = \text{constant} \quad (2.13)$$

and the pitch angle must change as the magnetic field varies. The derivation presented here is approximate and heuristic, a more rigorous derivation can be found in [Chen, 1974]. In order for (2.13) to apply, the particle must go through many gyrations in a distance over which the magnetic field varies little, a condition which can be written as

$$\left(\frac{T_H v_{\parallel}}{B_o} \right) \frac{dB_o}{dz} \ll 1 \quad (2.14)$$

where z is the distance along the field line. This is known as the *adiabatic approximation*, and the quantity μ in (2.13) is called *the first adiabatic invariant*. Condition (2.14) is well satisfied in the inner magnetosphere. Equation (2.13) shows that α increases as B_o increases, and at the point where $\alpha = 90^\circ$ we have $v_{\parallel} = 0$ and the particle "mirrors". Figure 2.7 shows a portion of the trajectory of a typical particle in a dipole field. Since this field is symmetrical about the magnetic equator the particles mirror at conjugate points as they bounce between hemispheres.

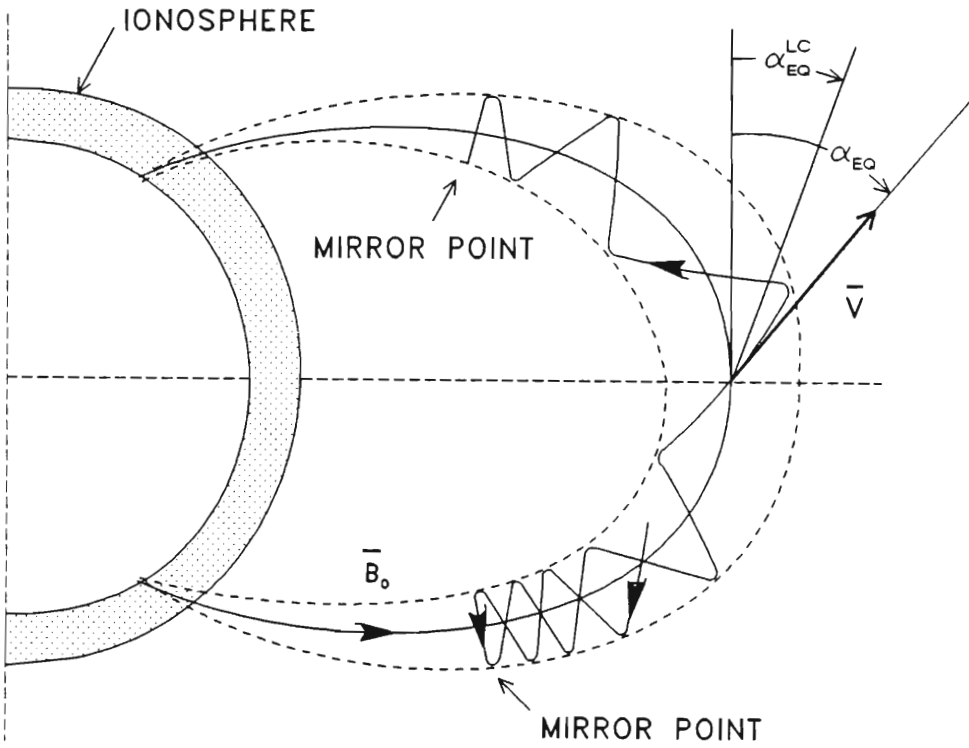


Figure 2.7: The trajectory of an energetic particle trapped in the earth's magnetic field

The location of the mirror point is uniquely determined by the equatorial pitch angle α_{eq} through (2.13), but the bounce period τ_B (the time taken to return to a mirror point) depends on both v (and thus energy) and the distance along the magnetic field line between the mirror points (and hence α_{eq}), and is given by

$$\tau_B = 2 \int_{z_m}^{z'_m} \frac{dz}{v_{\parallel}(z)} \quad (2.15)$$

where z is the distance along the field line and the subscript m refers to the mirror

points. This integral has been numerically evaluated [Liemohn, 1961] and can be written as a function of equatorial pitch angle

$$\tau_B = \frac{4R_o L}{v} f(\alpha_{eq}) \quad (2.16)$$

The value of $f(\alpha_{eq})$ varies from 0.75 to 1.4 for α_{eq} varying from 90° to 0° . A good approximation for $40^\circ \leq \alpha_{eq} \leq 90^\circ$ is

$$f(\alpha_{eq}) \cong 1.30 - 0.56 \sin \alpha_{eq} \quad (2.17)$$

In addition to the gyro and bounce motions energetic particles undergo azimuthal and radial drift across field lines. Gradient curvature drift is caused by the inhomogeneity of the field lines, causing electrons to drift eastwards and protons westwards. Drift periods vary from ~ 5 days for 10 keV electrons to ~ 15 minutes for 1 MeV electrons near $L=4$. Radial electric fields cause $E \times B$ drift which is in the same direction for both electrons and protons. For a more detailed discussion of cross field drifts see [Chen, 1974]. For radiation belt particles τ_B ranges from one tenth of a second to a few seconds. In comparison, gyroperiods are in the range of 10^{-5} - 10^{-3} seconds, thus the three motions (gyro, bounce and drift) are almost completely separable, which is the basis of the adiabatic approximation.

The loss cone and particle precipitation

As we have seen the particle's mirror point is determined by α_{eq} . If the altitude of the mirror point is lowered into regions of higher atmospheric density (below ~ 200 km) the chances of the particle colliding with neutral constituents and being absorbed are increased. This leads to a removal or *precipitation* of the particle and it is lost from the radiation belts.

We can define a pitch angle for a particle at the equator (where the pitch angle is at a minimum) for which the mirror point is at some height h_m where the particle is most likely to be lost. This pitch angle defines a cone in the particle velocity space and is called the *loss cone angle* α_{eq}^{lc} . The height h_m is called the lowest mirror height, and any particles within the loss cone are not able to mirror and are precipitated. Defining a normalised lowest mirror geocentric radius as

$$\xi_m = \frac{R_o + h_m}{R_o} \quad (2.18)$$

and using the dipole geometry and first adiabatic invariant we can write

$$\sin(\alpha_{eq}^{lc}) = \left[\frac{\xi_m^3}{L^2 \sqrt{4L^2 - 3\xi_m L}} \right]^{\frac{1}{2}} \quad (2.19)$$

It is clear that α_{eq}^{lc} depends strongly on L and thus the particular field line, but is fairly insensitive to h_m as can be seen in figure 2.8 which gives the equatorial loss cone angle as a function of L for various values of h_m .

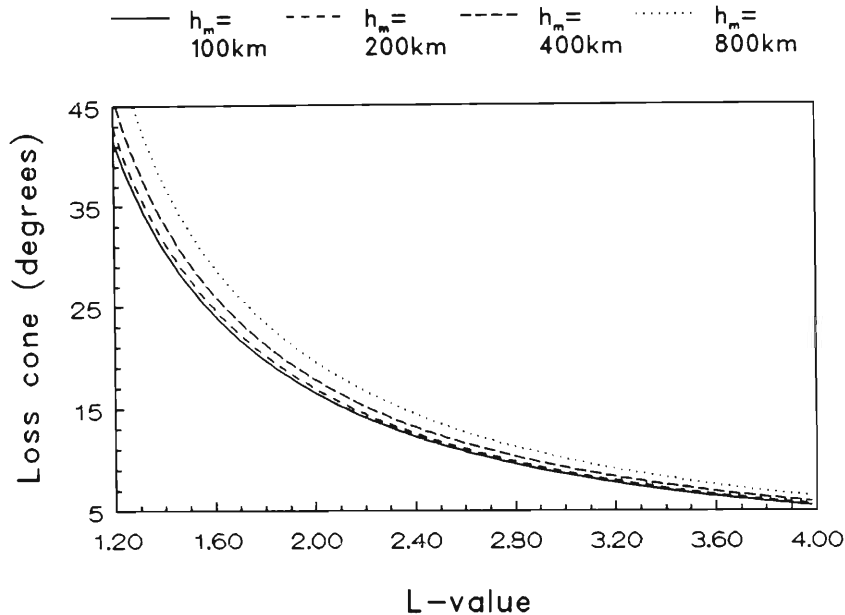


Figure 2.8: Plot of α_{eq}^{lc} as a function of L -value for $h_m = 0, 100, 200, 400$ and 800 km

In the absence of any forces which may alter α_{eq}^{lc} particles may be trapped from an hour to a few days, while some are stably trapped [Roederer, 1970]. Particles can be detrapped when their azimuthal cross field motion causes them to drift to the sunlit side of the magnetosphere where the solar wind induces distortions of the field lines. The only way in which particles can be lost on a short time scale is when α_{eq}^{lc} is significantly altered, which may happen through wave-particle interactions. The trimp event under study in this thesis is a manifestation of such an interaction. Precipitation by pitch angle scattering from wave-particle interactions is one of the main loss mechanisms for radiation belt particles.

Figure 2.8 also shows an important difference in the amount of pitch angle change needed to precipitate a particle at low L compared to one at high L . At high $L = 4$ a pitch angle change of $\sim 1^\circ$ changes the reflection height from 800 km (tenuous ionosphere) to 100 km (dense ionosphere). At $L = 1.7$ (Durban) the change required is $\sim 4^\circ$, which increases to ~ 9 degrees at $L = 1.3$. Thus as one moves to lower L -values a progressively larger change of α_{eq} is required to successfully precipitate electrons. This effect is partly offset by the smaller magnetic dip at low L which increases the distance electrons travel between any two ionospheric heights, which in turn increases the probability of a collision.

2.2.5 The Basic Gyroresonance Interaction

Wave-particle interactions in the inner magnetosphere involve resonances between energetic charged particles and waves. Resonance occurs when the Doppler shifted wave frequency seen by the particles is an integer multiple of the particle gyrofrequency. For electrons, the resonance condition is given by

$$\omega - \mathbf{k} \cdot \mathbf{v}_{\parallel} = m\omega_H \quad m = 0, \pm 1, \pm 2, \pm 3, \dots, \quad (2.20)$$

where ω is the wave frequency, \mathbf{k} is the wave vector, \mathbf{v}_{\parallel} is the parallel component of the electron velocity and ω_H is the electron gyrofrequency. The two conditions in (2.20) of primary interest are the $m=0$ longitudinal (Landau) and $m=1$ cyclotron resonance. In longitudinal resonance wave phase velocity (v_p) is nearly equal to the particle parallel velocity (v_{\parallel}) and both are in the same direction. Longitudinal resonance has been proposed as the mechanism responsible for auroral hiss [Maggs, 1976] and has been used to explain the observed lower frequency cutoff of plasmaspheric hiss [Thorne et al., 1973]. However it plays a minor role in wave-particle interactions associated with ducted waves.

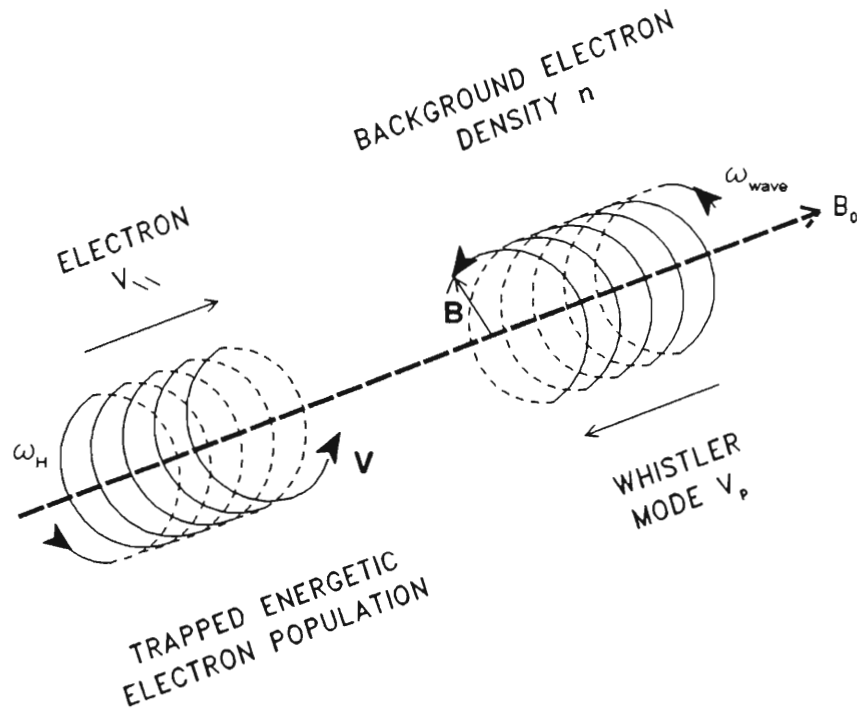


Figure 2.9: Spiral motion of whistler and electron about the geomagnetic field. v_p and v_{\parallel} must be opposite and parallel for effective interaction (Hargreaves, 1978)

For cyclotron resonance to occur with whistler-mode waves ($\omega < \omega_H$) the whistler frequency needs to be translated upwards to match the gyrofrequency, which

requires waves and electrons to be counter-streaming (Figure 2.9).

The resonance phenomenon in the magnetosphere is complicated by the complexity of the boundary conditions imposed by the ionosphere and the environment, with its spatial variation of magnetic field and plasma population. A change in magnetic field strength changes the electron gyrofrequency, so that the resonance condition (2.20) can only be satisfied locally. Since inhomogeneity of both field and plasma is at a minimum along a magnetic field line near the equator, the spatial extent of the interaction region is largest in that region. This fact is used by most theories on cyclotron resonance by assuming that the interaction is limited to an *interaction region*, and that any changes to the particle dynamics or wave spectrum due to the interaction occur in this region only.

One possible effect of the interaction is the lowering of the pitch angle of the interacting particle. Such a particle will then be lost into the ionosphere within the next few bounces. The detailed derivation of the equations of motion for this interaction is given in Chapter 5.

2.3 Calculation of Precipitation Fluxes

The equations of motion for the gyroresonant interaction have been studied in some detail for the region of $L=2-4.5$. The low L region from $L=1.2-2$ is studied here in more detail in Chapters 5 and 7. The original work by [Inan et al., 1978] considers the effect of a 5 kHz continuous wave on an equatorial test-particle distribution $f_{eq}(v_{||eq}, \alpha_{eq})$ and calculates the resulting fluxes at $L=4$. Energetic (1–2 keV) electron fluxes in the order of $\sim 10^{-1}$ erg/cm²s can be precipitated by a CW wave of 10 m γ amplitude. In a further study, [Inan et al., 1982] extend this model to calculate the fluxes produced by short duration VLF pulses (such as those which make up a whistler), also at $L=4$. For a pulse of a given length and frequency the effect on a full test-particle distribution at each point along a field line is calculated, and the results are summed together to obtain a total precipitated flux as a function of time.

Finally, [Chang and Inan, 1985] extend the model to include the effects of changing frequency and dispersion within a variable frequency wave packet such as a whistler to quantitatively determine the temporal profile of whistler induced fluxes as a function of L -shell. This study uses idealised whistlers and energetic particle populations but is useful in indicating what kind of precipitating fluxes can be expected. An example of this is shown in Figure 2.10. The total flux of precipitating particles at $L=4$ is shown, using a particle population with a steep, initially empty losscone and an energy distribution function $f(E, \alpha) \propto E^{-3}$. $T = 0$ represents the injection of the the whistler.

The [Chang and Inan, 1985] study only considers interactions down to $L = 2$, but shows clearly that at lower L the precipitated flux is almost entirely due to electrons with energies $E_e \geq 50$ keV, that the precipitated flux pulses get

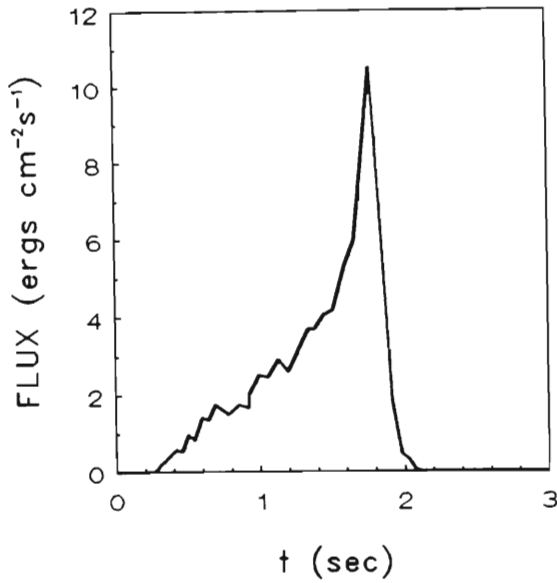


Figure 2.10: The computed precipitated energy flux versus time as would be observed in the northern hemisphere after the injection of the impulse wave energy at $t = 0$ in the same hemisphere at $L = 4$. (Figure 6(a) from Chang et al. [1985])

narrower in time and decrease in intensity. The study presented in chapter 5 will show how this trend is continued and magnified at extremely low L .

2.4 Ionospheric Response to Electron Precipitation

The precipitating electrons interact with the lower ionosphere where they produce numerous secondary electrons and create an impulsive ionisation enhancement throughout the volume of the precipitation region. As a result the ionospheric conductivity in the same volume is greatly enhanced. Higher energies penetrate to lower altitudes and enhanced ionisation at low heights can form a disturbance of the earth-ionosphere waveguide for VLF signal propagation (section 2.6).

Experimental data on flux and spectra of precipitated electrons are usually not available. [Tolstoy et al., 1986] made use of a computer program based on the work of [Rees, 1963] to calculate the modified profiles of electron density as a function of incident energies and fluxes. Figure 2.11 shows the modified electron density profile for mono-energetic electron spectra of 50–150 keV energy and fluxes in the range 10^{-7} – 10^{-3} erg cm $^{-2}$ s $^{-1}$. These spectra are considered to be representative of the trimpi effect (see Section 2.5).

The actual enhancement profile (as a function of time) can be estimated from the

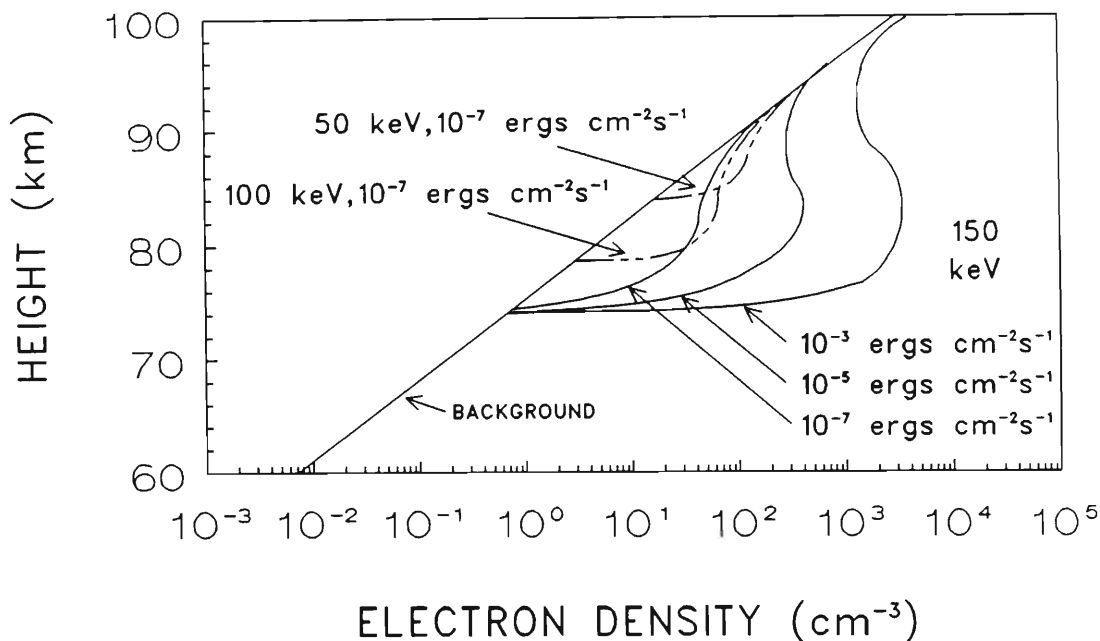


Figure 2.11: Modified electron density profiles for ionisation enhancement regions resulting from the indicated spectra. Background nighttime exponential profile is for a reflection height of 87 km and electron density gradient of $\beta = 0.47 \text{ km}^{-1}$

precipitation fluxes as calculated (See Section 2.3). During the timescale of the precipitation (up to $\approx 4 \text{ s}$) we can ignore diffusion and recombination rates in the ionosphere and the total ionisation enhancement is then simply a superposition of the individual energy ionisation responses.

After precipitation has occurred the ionosphere relaxes back to normal conditions. The relaxation time is equal to the combined recombination and diffusion time constants and is in the order of tens of seconds [Ratcliffe, 1972].

A detailed study of the modification of the ionosphere due to wave-induced electron precipitation is beyond the scope of this work and the reader is referred to the excellent work by [Doolittle, 1982] on this topic.

2.5 A Very Complicated Problem

As can be seen from the previous sections the problem of determining the kind of precipitation patch/area one is likely to see as the result of a WIEP event is a broad one. We have presented the mechanics of the gyroresonant interaction, and have pointed towards the kind of precipitated fluxes produced by short VLF mono-frequency pulses, and have shown the kind of ionospheric response one may expect for given energy fluxes.

In the case of lightning induced precipitation (by a whistler) the approach needed is to consider the superposition of all the precipitation effects due to all the separate whistler frequencies travelling through the magnetosphere with their own characteristic delay times. To do this even the definition of the initial wave pulses that make up the whistler as it is launched into its ducted path becomes problematic, both the exact wave intensity profile as a function of frequency and the length of wave pulses as a function of frequency are not well known. However these parameters could be approximated from spheric measurements on low orbiting satellites, even though the exact measurements of these parameters for the lightning strike/whistler responsible for a particular WIEP event remains unlikely simply because of the scale of the phenomena and the low density of data coverage both spatially and temporally.

Of crucial importance to the precipitated fluxes is the energetic particle distribution in the radiation belts, in itself not a static quantity. Again, one is unlikely to have available good data from satellites at exactly the time and place when an event is observed.

Finally the shape, size and duration of a WIEP-patch in the ionosphere (which ultimately determines the shape and duration of the trimpi event) is not only a function of the precipitated flux profile (both in energy and time) but also a function of the state of the ionosphere at that particular time and location. Unless one is fortunate to have an ionosonde exactly under the precipitation patch or data from rocket flights at the time of an event the state of the ionosphere can at best be inferred from the large body of data accumulated at different places and times. Diffusion and transport mechanisms which determine the dynamics of a precipitation region as it decays are further a function of electric and magnetic fields in the ionosphere and thus depend on the magnetosphere-ionosphere system as a whole.

The next link in the trimpi process, the effect of such a precipitation patch upon sub-ionospheric VLF propagation, has not been touched upon yet. A complete analysis of sub-ionospheric propagation in the presence of a dynamically disturbed wave-guide is beyond the scope of this present work, but has been the topic of extensive studies and simulations by other authors [Tolstoy et al., 1986, Poulsen et al., 1990, Dowden and Adams, 1988, Dowden and Adams, 1989]. In the next two sections a few of the approximate mechanisms used to derive the trimpi disturbance on VLF signals are presented.

2.6 VLF Earth-Ionosphere Propagation

The topic of VLF propagation in the earth-ionosphere waveguide is one of the oldest and best studied topics in radio-wave propagation theory ([Wait, 1970]). VLF signal paths are in general not subjected to the same type of variations as the paths taken by HF radio, and thus make very reliable communications possible

(be it at a low data transfer rate), and enable accurate navigation around the clock (OMEGA system, [Garrison, 1986]). The absence of other disturbances also enables the detection of trimpi events.

In general, several conceptual models are used to describe VLF radio propagation, for distances of more than one wavelength from the transmitter, so that near-field effects can be neglected. We can consider three primary methods of propagation:

- (a) Ground Wave : Based on the assumption of a spherical earth with homogeneous electrical characteristics and devoid of any surrounding ionosphere.
- (b) Sky Wave : Uses conventional ray theory which treats the ionosphere as a sharp boundary. The problem becomes mainly a geometrical one fitting ray paths with multiple reflections to a signal path.
- (c) Waveguide Mode Theory : Electromagnetic waves are guided between the earth and the ionosphere and the propagation may be described in terms of waveguide theory.

The total field can be expressed as the sum of a ground wave and a sky wave or as the sum of a number of modes in which electromagnetic energy is propagated between two boundaries. Both ground and sky wave concepts are useful at small <2000 km distances, and at higher VLF and LF frequencies. At frequencies such that the distance from the surface of the earth to the ionospheric reflection height becomes comparable to a wavelength it is no longer valid to employ simple ray concepts, and waveguide mode theory has to be employed. Since this is the case for the frequencies considered in trimpi-related work mode theory is generally used. Mode theory is also the most appropriate when considering the effect of ionisation enhancements on the signal (Section 2.7.1) since the shape and impedance of the bounding surfaces is a major factor in determining the modes that will propagate.

For a detailed exposition of mode theory of propagation the reader is referred to any standard text such as [Budden, 1961].

2.7 Modelling Trimpi Mechanisms

The localised ionisation enhancements (“Precipitation patches”) resulting from electron precipitation perturb the normal nighttime ionospheric reflection height at 85–87 km [Ferguson, 1980]. This consequently alters the propagation characteristics of the earth-ionosphere waveguide. During normal day-time conditions the reflection height is 70–72 km, and the fact that no events are observed during daytime indicates that the major particle energies involved are in the range of 40–200 keV (the energy required for electrons to penetrate to nighttime reflection heights)

The complete simulation of the effect of a local ionisation enhancement of a VLF signal should take into account the whole three-dimensional waveguide topography and a complete description of the disturbance, i.e. position, size, depth and shape of the ionisation patch. This has not been done to date, and is beyond the scope of this thesis. We present here two models which independently investigate the VLF signal perturbation due to an ionisation enhancement. In Section 2.7.1 a complete modal description of the VLF propagation is used to investigate the effect of ionisation patches which lie exactly along the signal propagation path, whereas in Section 2.7.2 we use a simpler model description to investigate the effect of ionisation patches which lie near but off the propagation path.

Both models are capable of reproducing the types of trimpi signatures which have been measured (positive and negative amplitude and phase perturbations [Inan et al., 1985, Dowden and Adams, 1989]), and there is no way of distinguishing which kind of mechanism is responsible for a given event. For this, data from more than one station covering the same event is required (see Section 8.3).

2.7.1 Two Dimensional: “On Path Trimpi”

Results presented in this section are from [Tolstoy et al., 1986], which use a complex mode-propagation model (two dimensional Budden-Wait-Pappert model; [Budden, 1961, Wait, 1970, Pappert and Snyder, 1972]) to study the effect of precipitation patches on the VLF signal. This model includes as much realism as is currently possible, including mode conversion and variable ground conductivity (modelling mixed land/sea propagation paths). A computer program *MODESRCH* [Morfitt and Shellman, 1976] is used to determine the set of significant modes for a given source-receiver path or path segment. However, for long signal paths beyond several thousand kilometres only the lowest modes are strongly excited and have the smallest attenuation rates, and contribute significantly to the field. When a signal path encounters no abrupt changes in environmental parameters (such as ground conductivity changes at water/land, water/ice and land/ice transitions; and ionospheric conductivity/reflection height changes at day/night transitions and *localised ionisation enhancement, i.e. trimpi events*) the five strongest modes adequately describe the signal. However for path segments including one or more of the above transitions a complete mode set of 15 modes is retained in calculations. Accuracy in the description of the ionospheric medium is crucial since changes in the effective reflection height of a nighttime ionosphere can result in up to 20 dB changes in signal amplitude [Ferguson, 1980]. The modified electron density profiles used here are shown in Figure 2.11.

In general, nighttime paths longer than 6000–7000 km are characterised by one strongly dominant mode. When a single mode encounters a region of enhanced electron density, its attenuation is increased and its phase advanced. In the absence of mode conversion a signal amplitude decrease would then be expected. However, if two or more modes are present, then amplitude increases and phase retardations may result as the modal interference pattern is altered.

Propagation model predictions of signal amplitude show that each transmitter to receiver path has a unique character, and thus each path reacts differently to the same ionisation enhancement. The most important factors affecting paths under uniform background conditions are the transmitter frequency, geographic location of the ionisation enhancement, the electron density profile and the ground conductivities encountered. Due to the interplay of all these factors it is impossible to obtain general features valid for all trimpi events on all possible paths, the full model calculations have to be done for each individual set of circumstances. Thus the results presented in Section 3.7 are valid for SANAE only.

[Tolstoy et al., 1986] have applied this method to VLF signal paths to Palmer Station, Antarctica. Their results are summarised in Figure 2.12 for computations on four signal paths, NAA at 17.8 kHz, NSS at 21.4 kHz, NLK at 18.6 kHz and NPM at 23.4 kHz. The numbers (+/-) along the paths in Figure 2.12 give the amplitude change (ΔA) according to the code given in Table 2.1.

0	⇒	0.00 dB	≤	ΔA	≤	0.15 dB
1	⇒	0.15 dB	≤	ΔA	≤	0.50 dB
2	⇒	0.50 dB	≤	ΔA	≤	1.00 dB
3	⇒	1.00 dB	≤	ΔA	≤	1.50 dB
4	⇒	1.50 dB	≤	ΔA	≤	2.00 dB
5	⇒	2.00 dB	≤	ΔA	≤	2.50 dB

Table 2.1: Amplitude change codes for Figure 2.12

A precipitation region 50 km in length resulting from 150 keV electrons with a flux of 10^{-7} erg cm $^{-2}$ s $^{-1}$ is assumed. The circular segments give distance from Palmer in 100 km intervals.

As can be seen from Figure 2.12 each path shows a different behaviour of amplitude perturbation as a function of distance from the receiving station. Trimpi characteristics of a path are thus completely specific to that path.

By changing the parameters of the model calculations in such a way that the predicted amplitude and/or phase perturbations fit the observed data some information about the characteristics of the ionisation enhancement regions may be obtained. Application of this model to data from SANAE collected by the author with the methods described in this thesis is a further suggestion for future research (see Section 8.3).

2.7.2 Three Dimensional: “Off Path Trimpi”

One possible mechanism to explain phase and amplitude perturbations is to consider the superposition of “Echoes” [Dowden and Adams, 1988] from precipitation patches and the direct signal at the receiver.

This method assumes that precipitation patches, laterally displaced from the

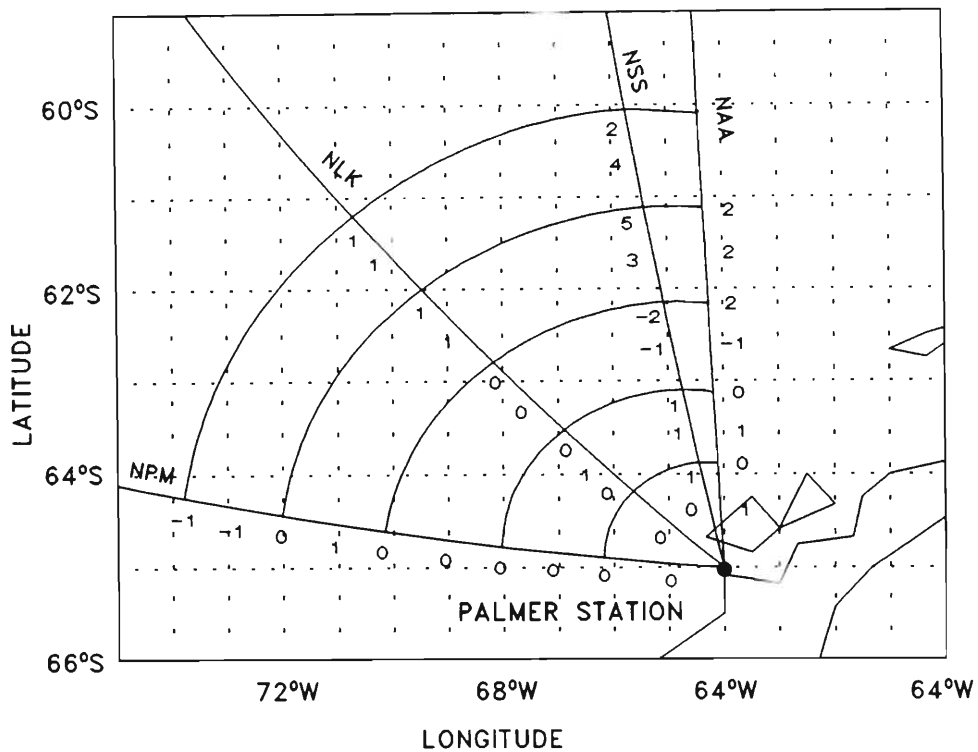


Figure 2.12: Amplitude effects of ionisation enhancement regions on NSS, NAA, NLK and NPM signals at Palmer (Tolstoy et al., [1986]).

great circle transmission path, produce echoes at the receiver slightly delayed relative to the direct signal. The resulting interference can then cause both amplitude and phase trimpis of both signs. This method allows for much greater phase variations, since not only does the precipitation patch affect the phase, but a phase difference is also introduced due to the path difference between the direct and echo signals. To demonstrate this method Dowden and Adams investigated the 22.3 kHz signal from NWC (North-West Cape, Australia) to Dunedin, New Zealand. Single mode propagation only was considered, using the dominant second mode for this path.

Figure 2.13 demonstrates this mechanism. The great circle path is shown (thick line) together with a possible echo path (thin line) for the signal diffracted by the precipitation patch (small dot).

Position of the patch is a possible one for a small patch. For a Gaussian depth distribution of the enhanced ionisation (not necessarily realistic) the patch would re-radiate a single diffraction beam with no side lobes as shown in Figure 2.13. For precipitation patches with dimensions of ~ 40 km the beam width is about 20° , so that significant echoes might be received from patches up to 200 km off the great circle path for distances from the receiver over 1000 km. For larger patches the beam becomes narrower, which requires the patch to lie nearer the great circle path so that much of it might straddle the direct path, thus for large patches the one-dimensional approach in 2.7.1 is a good approximation. The ratio

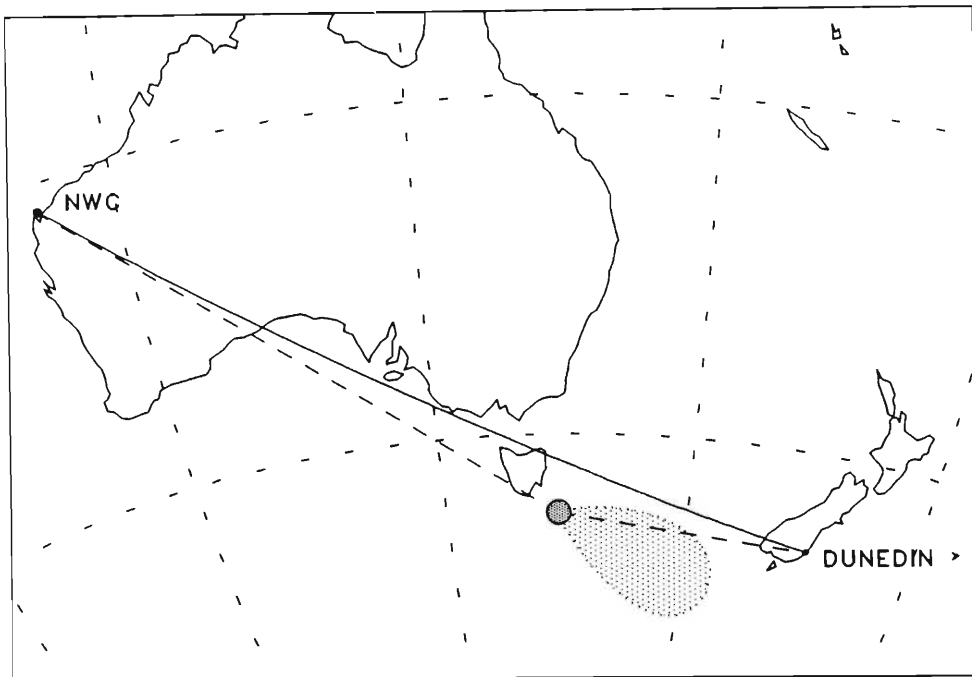


Figure 2.13: Scenario for “Echo Trimpi” (Dowden and Adams [1988])

of echo- to directly-received power is given approximately by

$$R_p = G \frac{\sigma}{2\pi h} \left(\frac{1}{r_1} + \frac{1}{r_2} \right) \quad (2.21)$$

where σ is the scattering cross section of the ionisation “stalactite” caused by the precipitation, h is the ionospheric reflection height, r_1 and r_2 are the transmitter-patch and patch-receiver distances respectively, and G is the counter part of antenna gain, determined by horizontal dimensions of the patch in a direction perpendicular to the patch-receiver path and the shape of the enhanced ionisation depression. Beam width is of the order of λ/D where λ is the wavelength of the VLF signal, and G is very small outside this beam.

[Dowden and Adams, 1988] have shown how data from the NWC-Dunedin path can be fitted to this model, and have calculated echo phase and relative amplitude required to produce the observed trimpi events. Echoes in the range of -30 dB relative to the direct signal are able to explain the observed events.

A further interesting result from Dowden and Adams [1988] is their observation of a systematic drift in time of the echo phases needed to explain successive trimpi events over an 8-hour observational period, where the phase decreased at a rate of 65° per hour. When this change in echo phase is interpreted from the point of view of a moving duct exit point (thus producing ionisation patches at successive locations along the loci or “footprint” of the duct, indicated by the arrow in Figure 2.13) this yields an average duct drift speed of 37 km/hr, a reasonable duct drift speed [Thomson, 1976] showed that at $L=2.5$ drift in L leads to speeds

of about 30 km/hr southward for the duct footprint).

A more sophisticated model of subionospheric VLF propagation in the presence of ionisation enhancements such as occur in the trimpi event has been developed by [Poulsen et al., 1990]. Although only the dominant transmitter mode is considered, the model is extended to three dimensions to account for ionisation patches which do not lie exactly on the great circle path between transmitter and receiver. The results of this model show that the amplitude perturbations maximise for “on-path” events and become negligible for events that occur more than 20 wavelengths off the path, while the phase perturbations maximise at about 8 wavelengths from the path before becoming negligible at distances more than 20 wavelengths from the path.

2.8 History of Trimpi Observation

Observations of trimpi events date back to 1963 when they were first observed at Eights and Byrd Stations (Antarctica) by M.L. Trimpi during his year long stay (hence the term “Trimpi” event). They were first reported at a URSI conference in Los Angeles in 1971 but were only published in 1973 [Helliwell et al., 1973] which reported amplitude trimpi events on signal paths from North America observed in the Antarctic, and linked these events to whistlers observed at the same time.

Phase trimpi events were first observed by [Lohrey and Kaiser, 1979] on a signal path from NWC to Dunedin, New Zealand, and also associated with whistlers.

Most of the early observations of trimpi events come from the US Antarctic stations Siple, Eights and Palmer [Carpenter and LaBelle, 1982, Inan et al., 1982, Leyser et al., 1984, Chang and Inan, 1985]. Trimpi events on MF signals were also reported [Carpenter et al., 1984].

Extensive studies were done on a network of VLF paths crossing North America [Inan et al., 1988c, Inan et al., 1988b] in conjunction with a lightning detection network in the United States. From an extensive study of trimpis and their associated lightning strike a new type of trimpi event was found: A so called “fast” trimpi [Inan et al., 1988b] which showed that for some events the onset time between the causative spheric and the trimpi event is < 50 ms, allowing no time for wave-particle interaction in the magnetosphere (which produces time delays in the order of seconds). It is believed that these events are due to direct ionospheric heating due to the intense VLF radiation from a lightning strike. D-region ionisation and its effect on VLF radio propagation has been experimentally verified [Barr et al., 1984], while from a comprehensive description of D-region ionisation [Inan et al., 1991] it is found that such heating can successfully account for most aspects of the reported “fast” trimpi event.

Work has also been done on short paths over ice in the Antarctic using the Siple

transmitter and stations Palmer and Halley Bay [Hurren et al., 1986, Carpenter et al., 1985].

The NWC (North West Cape, Australia) signal paths to a chain of receiving stations in New Zealand has been investigated [Dowden and Adams, 1988, Dowden and Adams, 1989, Adams and Dowden, 1990], including studies on the two sideband frequencies of MSK modulated signals and studies on events observed by two stations on a short baseline (\sim one wavelength).

The current work describes the first events observed at SANAE, Antarctica (see section 3) and the first extremely low-L trimpi events observed at Durban, South Africa (section 6).

An increasing amount of work has been done to understand all the mechanisms contributing to a trimpi event (see references in the relevant sections of this Chapter), and the trimpi event is rapidly developing into a passive tool for understanding the dynamics of radiation belt electrons. Emphasis is now being placed on international collaboration in large trimpi detection networks (see section 8.3).

Chapter 3

Trimpi Events Recorded at SANAE, Antarctica, 1982

In this chapter the analysis system used for extracting trimpi events from VLF data on tape is described. The system is used for a survey of 1982 SANAE data. This chapter reports the first trimpi events recorded at SANAE (70°S , 002°W , $L = 4.02$) on signals from a number of transmitters in the frequency range 15.1–22.3 kHz.

3.1 Data Source

Often signals from as many as six transmitters were observed at the same time, giving a wide range of propagation paths to SANAE. Details of the VLF transmitters are given in Table 3.1, and their great circle paths to SANAE are drawn in Figure 3.1.

Data were recorded on broadband audio tape at SANAE and the required frequency signals were extracted and digitised at Durban using a narrow band (bandwidth of 160 Hz) Ubiquitous Spectrum Analyser. The resulting data files which typically contained 90 minutes of data (the duration of one side of the audio tape) were then processed digitally. FFT methods were employed to remove interfering signals and trimpi events were detected using the automatic method described below. The absence of a stable reference frequency on the data tapes makes phase detection impossible, thus only amplitude perturbations were detected. The recording schedules were originally chosen to study the relationship between VLF and aurora, and thus only cover local nighttime, magnetically disturbed periods. Since 1982 was not a particularly active year for aurora the data coverage is somewhat limited. Receiving and recording equipment was band-limited to frequencies <20 kHz and only on one occasion was a frequency above 20 kHz strong enough to be detected (22.3 kHz NLK).

F (kHz)	CALL-SIGN	STATION	LONGITUDE	LATITUDE
22.3	NLK	Jim Creek	121°55'W	48°12'N
19.6	GBZ	Anthorn	003°30'W	55°00'N
19.0	GQD	Criggion	003°04'W	52°43'N
18.1	UPD8	Murmansk	033°05'E	67°58'N
17.8	NSS	Washington DC	076°27'W	38°59'N
17.8	NAA	Cutler MF	067°17'W	44°39'N
16.8	FTA2	S Assise	002°35'E	48°33'N
16.4	DMA	Mainflingen	009°00'E	50°01'N
16.4	JXZ	Helgeland	013°01'E	66°25'N
16.2	UGK	Kalingrad	020°30'E	54°42'N
16.0	GBR	Rugby	001°11'W	52°22'N
15.1	HWU	Le Blanc	001°05'E	46°37'N
15.1	FUO	Croix D Hins	000°48'W	44°45'N

Table 3.1: List of VLF transmitters observed at SANAE in 1982

Data were collected for 376 hours between day 77 and day 279. Figure 3.2 shows the hours of data collected for each transmitter frequency.

The 17.8 kHz NAA signal is the strongest and most frequently received at SANAE. Figure 3.3 shows the distribution of hours in local time (for SANAE $LT = UT$). Most of the data were recorded between 2200 and 0500 LT, and this will be considered to be the statistically relevant period.

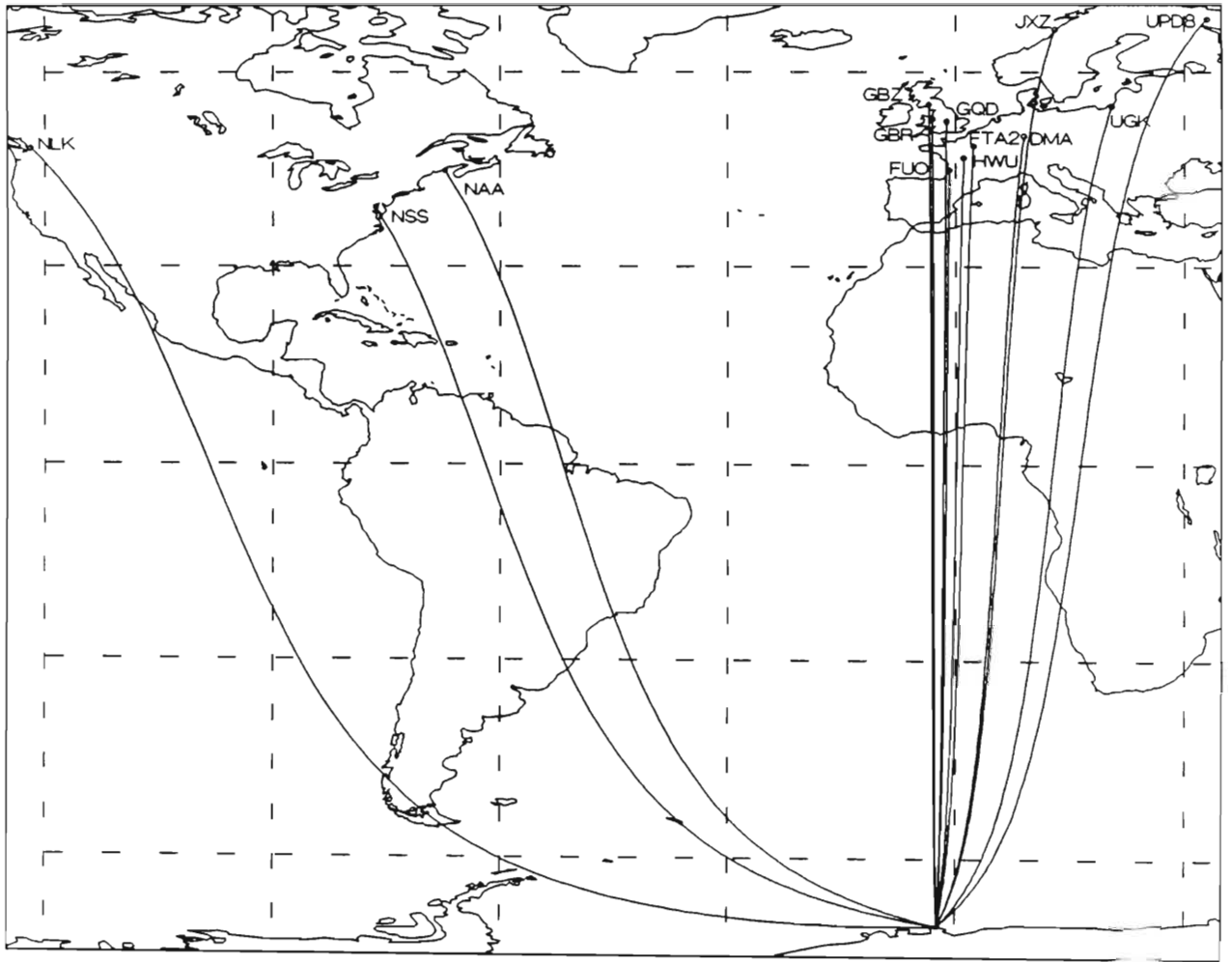


Figure 3.1: Great circle paths from VLF transmitters to SANAE

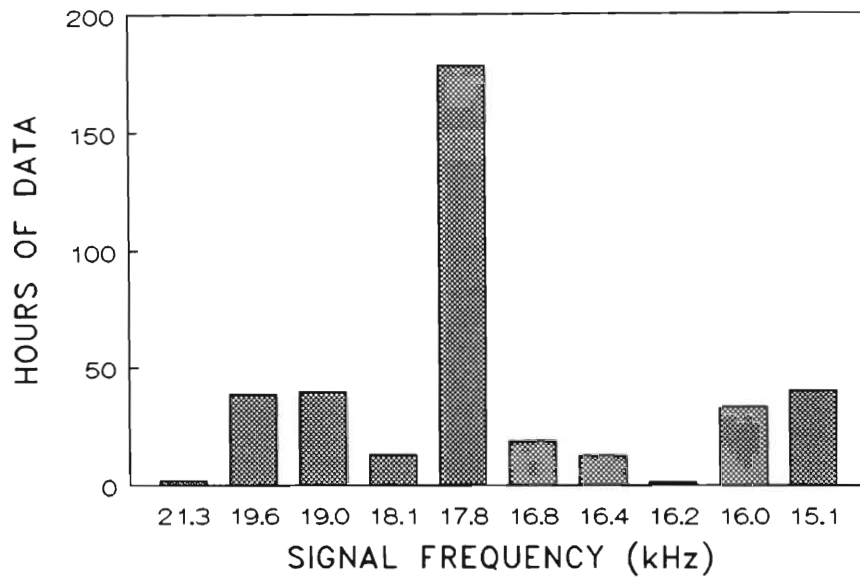


Figure 3.2: Distribution of the hours of data recorded with respect to observed frequency

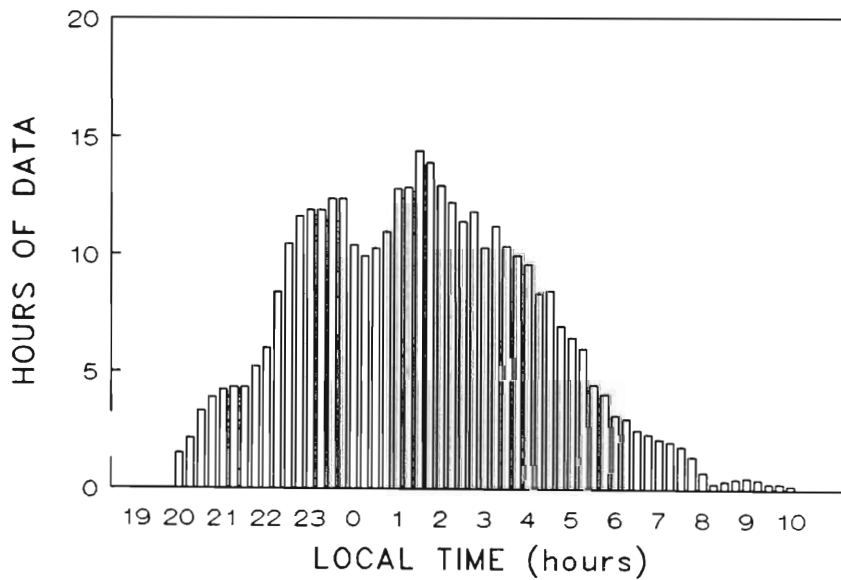


Figure 3.3: Distribution of hours of data recorded with respect to local time of data in 15 min intervals

3.2 The Analysis System Hardware

The system developed for this project was designed to convert the single frequency amplitude information contained on the data carrier (magnetic tape) to an accurately timed digital time series suitable for further analysis on a personal computer. The system is designed around an IBM compatible personal computer (PC) which can handle all the data acquisition and analysis tasks and a spectrum analyser to extract the desired frequencies from the broadband data on tape. The overall block diagram of the system is shown in Figure 3.4.

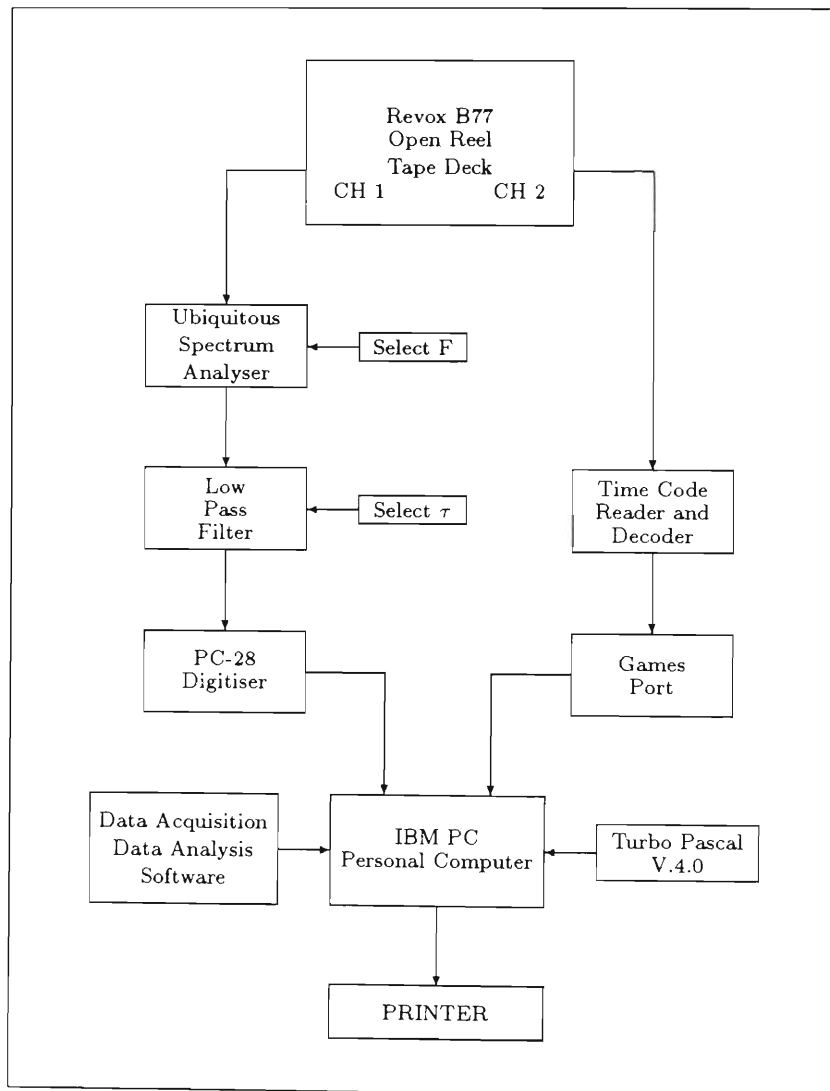


Figure 3.4: Analysis System Block Diagram

The data tapes are loaded onto a Revox B77 tape deck for replay. The VLF channel of the tapes is fed to a Ubiquitous Spectrum Analyser. This instrument can be run in several modes, a full spectrum mode or single frequency sampling with extremely narrow bandwidth.

Once the signals present on tape have been established using the full spectrum

mode (a full 500-point spectrum over the frequency range of 20 kHz is clocked out at the rate of 25 Hz and can be viewed on an oscilloscope) the Ubiquitous is set to single frequency mode. In this mode a single frequency is sampled at the rate of 10 kHz, providing a theoretical upper limit for the time resolution this system can provide. The output of the Ubiquitous is a voltage between 0–10 Volts representing the signal strength, and can be set to either linear or logarithmic scale. Here the linear scale is used, since trimpi events do not cover a wide dynamic range.

Noise and short term variations present on the selected frequency signal are removed by an analog low pass filter. This filter also serves to band-limit the signal before being digitised to prevent aliasing problems. The filter cut-off frequency ($1/\tau$) is set to half the digitiser's sampling frequency (the Nyquist frequency).

The PC-28 digitiser converts the frequency signal to digital format with a resolution of 8 bits. The digitiser is a standard plug-in board for the IBM PC and is fully software controlled.

The timecode-channel of the data tapes is fed to a timecode reader and decoder. Standard NASA time code is used to provide the timing information on the tapes. The reader displays the current time on the tape and provides serially decoded outputs which can be easily read by the IBM PC through a standard games port. A drawback of the NASA timecode is that it takes almost exactly one second to store the time information for that second on tape. This places an upper limit of 1 Hz on synchronising data read off tape, and thus on the accurate time-resolution of the data collected. This problem is overcome in software. The data is thus digitised and accurately timed under software control. The result is a data file for each continuous stretch of data which is stored for later analysis.

Viewing of the collected data is done using the graphics facility of the IBM PC Hercules screen. A standard dot-matrix printer is used to obtain hardcopies of graphics and text output. For high quality output the Hercules graphics format is converted for output on a HP laser printer.

3.3 Trimpi Detection

Trimpi events are identified here by their characteristic signature alone. Traditionally trimpi events have been associated with whistlers observed on simultaneous broadband recordings [Helliwell et al., 1973], and a close time correlation between amplitude perturbations and received whistlers has also been reported for all the events studied by [Carpenter and LaBelle, 1982]. A unique feature of SANA E is the absence of “causative whistlers” from the broadband data. This feature of the data is examined further in section 3.5.

A simple edge detection routine (similar to that used by [Hurren et al., 1986]) was used to test for rapid changes in signal amplitude. This procedure detected any

amplitude change in the signal over a given threshold which was consistent with the normal onset time of a trimpi event (in the order of 1–2 s). This was done by comparing two consecutive running averages each of 2 s duration computed in 0.2 s time steps along the data string. Due to the noisy nature of the signal the lowest threshold used was a 10% amplitude change (the signal had been low-pass filtered before analysis, but the time constant for this filter could not be too large in order not to mask the rapid onset of trimpi events). This method identified a very large number of “events” which upon inspection of the data were obviously artificial and did not fit the normal trimpi shape. All positive “events” detected were quite obviously caused by the transmitter turning on, or by amplitude modulation of the signal from NAA, which was used for the SEEP experiment conducted during May–December 1982 [Imhof et al., 1985]. The more complete template matching routine described here was developed to select only events which fit the trimpi shape to within a set tolerance. The routine was only run testing for negative trimpi events, since the absence of positive events had already been shown.

The typical shape of a trimpi event is well established. It is characterised by a rapid amplitude perturbation reaching a maximum of up to ± 10 dB in 0.5 to 2 s, followed by a slow (10 to 100 s) recovery to pre-event levels. This shape (Figure 3.5) can be approximated by a fractional ($D\%$) change in amplitude followed by a linear recovery over T s. (The actual recovery characteristic is closer to being exponential but for detection purposes a linear approximation is sufficient).

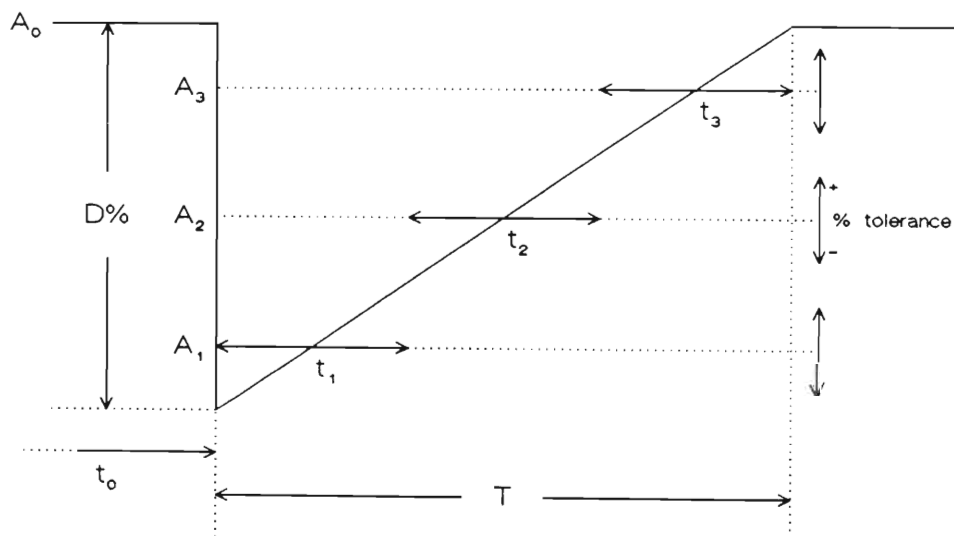


Figure 3.5: Trimpi detection template used in automatic trimpi searches

The total event time T is divided into three intervals t_1 , t_2 and t_3 , and a pre-event interval t_0 is specified. An average value for amplitude in each time interval is then found and compared to pre-selected averages A_0 , A_1 , A_2 and A_3 . If the computed averages and the pre-selected values agree to within some set tolerance

the event is flagged. By choosing the time T and total event depth D any type of trimpi can be selectively detected.

This test for trimpi events is run on each data file in one second steps and for a variety of trimpi shapes ranging from $D = 10\%$ to 95% depth in 5% steps, and $T = 6$ s to 72 s length in 6 second steps, and a tolerance of $\pm 5\%$ on the computed averages. Five typical trimpi events detected by this method are shown in Figure 3.6.

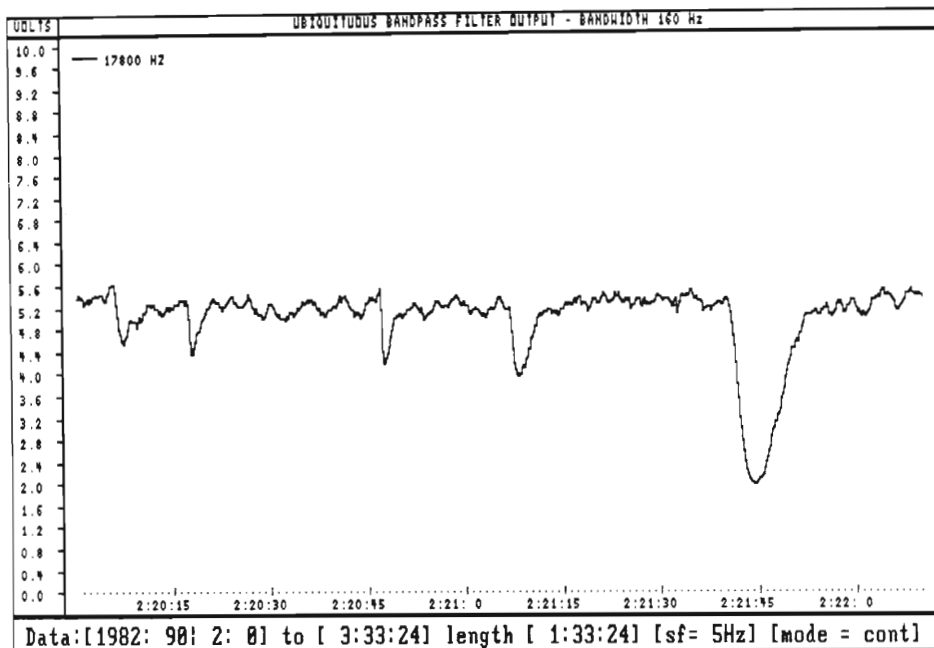


Figure 3.6: Series of typical trimpi events detected on day 90 on NAA 17.8 kHz signal. Each of the five events was detected by its corresponding template. Obtained from broadband 0–20 kHz data after band pass filtering, rectification and low pass (anti-aliasing) filtering (time constant 0.5 s). Digitised at 5 Hz. Amplitude is in relative units (volts of filter output)

The amplitude units are relative, measured in volts of spectrum analyser output. A total of 1120 trimpi events were detected in the data set. This automatic detection method is more self sufficient than that used by [Hurren et al., 1986] which relied on visual checking of the detected events. The method used here discriminates more efficiently against transmitter and mechanically (during tape record/playback) induced amplitude effects and is especially useful when dealing with large data sets. The operation of this method was tested by using visual spot-checks, which showed that all the negative events picked out by the simple edge detection routine which did fit the required shape were picked out again, and that all other perturbations were rejected.

In the absence of a stable reference frequency on tape there may be some doubt regarding the validity of an “event”, since it is known that tape recorded data are

subject to mechanically caused perturbations which could have the characteristics which would classify them as trimpi events. A very simple method was used to obviate this.

Data were recorded at SANAE using two-channel Revox recorders, the second channel being used for the NASA timecode. The data collection software reads the timecode and synchronises the digitising rate, re-calibrating itself once every second. If for any reason (tape fallout, mechanical playback faults, etc) synchronisation becomes impossible data collection is stopped, and the software attempts to re-synchronise at a later time. By setting the timecode reader up in such a way that it misreads at any amplitude perturbation on the timecode channel greater than 10% (the average noise level of the data) no data is collected when there are spurious amplitude perturbations on the tape, at such times a data gap occurs. During the course of playback of a 90 minute tape side such data gaps make up about 1 to 4 minutes on average. To collect data from several transmitters active at the same time the tape had to be played several times, which serves as a good test for this method; at all times the data gaps occurred at exactly the same times on all frequencies sampled. We thus have a high degree of confidence in the validity of the data and subsequent detection of trimpi events. Moreover, when data were available from more than one stations one of these stations could always be used as a reference for the other. Especially for unusual events, such as the very large ones reported in this paper, this visual inspection was done, and all the events "passed the test".

A more difficult problem is the possibility that the VLF transmitter was switched off and on in just the trimpi pattern, since for some of the very large events observed the signal does drop to the noise level for a short time at the onset of the event. For many of the stations observed at SANAE reports on transmitter failures during 1982 were not available, so this possibility cannot be ruled out. However, this explanation cannot account for all the large events observed (about 10% of all events as shown in Figure 3.8). It would be too much of a coincidence if all the transmitters failed and recovered in just the trimpi shape!

3.4 The Occurrence of Trimpi Events

A striking result of the observations is the absence of any positive trimpi events - all events found were negative amplitude perturbations. [Hurren et al., 1986] report that negative events observed at Halley Bay on Siple transmissions are more common, while [Carpenter and LaBelle, 1982], report that 80% of their observed events were positive amplitude perturbations, while negative amplitude events occurred during magnetically disturbed periods when the plasmopause was equatorward of their station. For our observations, taken during disturbed times, the plasmopause is likely to be equatorward of SANAE and thus the absence of positive events would be consistent with [Carpenter and LaBelle, 1982].

At SANAE both the total number of events and their rates of occurrence fall well short of those reported on other signal paths. Rates approaching ≈ 1 per minute were reported by [Hurren et al., 1986] on 3.79 kHz CW signals from Siple to Halley, and at Palmer Stations average rates of 30–40 events per hour, up to 80 events per hour were reported [Carpenter and LaBelle, 1982]. In chapter 6 rates of up to 44 events per hour on the NAA-Durban path are reported. The overall rate of trimpi events was only one every 20 minutes, with the maximum rate never exceeding 15 per hour. This lower rate could partly be due to the somewhat high threshold level of -10% (-0.92 dB) used in this study, which was due to the noisy nature of the data medium.

Another interesting feature of the SANAE observations is the occurrence of some very large events, with depths of over 90% which depress the signal amplitude down to the noise level. An example of such an event is shown in Figure 3.7.

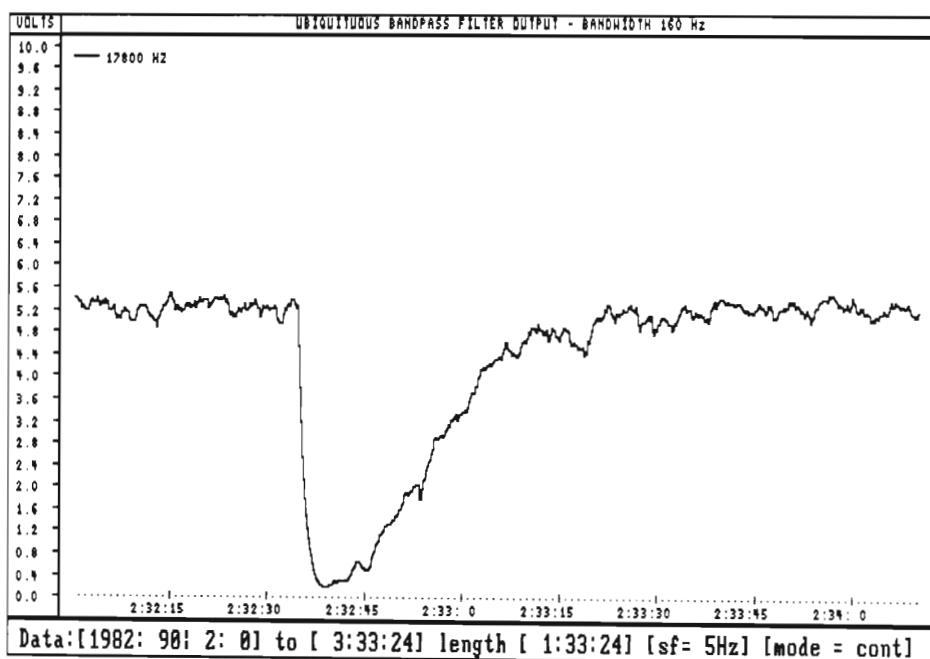


Figure 3.7: Large trimpi event detected on day 90 on NAA 17.8 kHz signal. Depth 95%, Length 52 s

However more data and transmitter information are needed to substantiate this unusual observation. Trimpi events of this size can only be understood if the precipitation patch interacts with the dominant mode of the transmitter in such a way as to re-radiate a strong second mode that effectively cancels the first mode at the receiving station. Since all transmitter paths are unique this scenario must be considered possible, even though events of such size have not been observed on other (even though comparable) paths. [Carpenter and LaBelle, 1982] reported events in the range of 10% to 50% only. [Hurren et al., 1986] suggest that events poleward of the plasmapause projection reach greater amplitudes compared to values of 0.5–2 dB (about 5% to 20%) in the plasmasphere region. This point is

further discussed in Section 3.5

Figure 3.8 shows the number of events detected as a function of depth (all durations, all frequencies). Events of deviations less than 10% fall inside the noise band and cannot be detected. Smaller perturbations of the signals are more frequent with 60% of the events having a depth <25%, and events of depths between 25% to 95% being more evenly distributed.

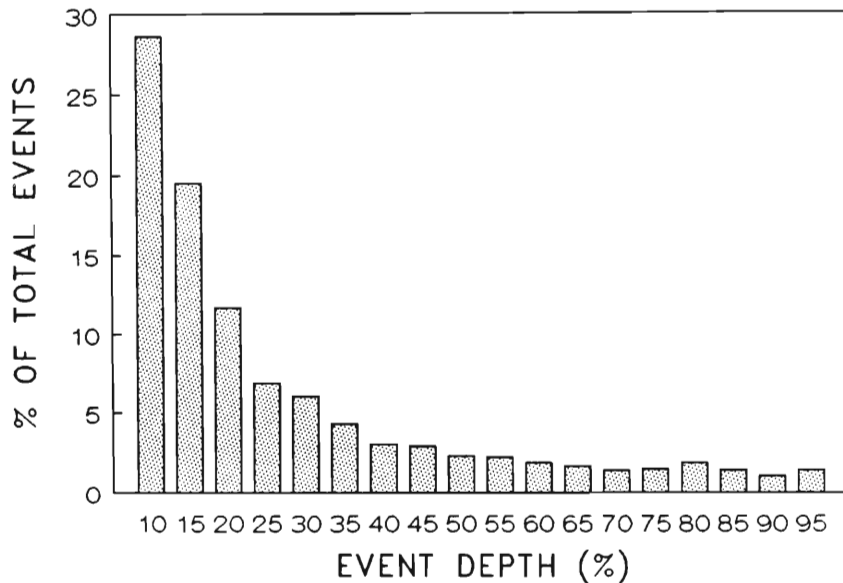


Figure 3.8: Distribution of trimp events. Detection template set to depths between 10–95% for all event lengths

This can be explained by the echo trimp mechanism [Dowden and Adams, 1988] which produces small events but is not effective in producing large signal perturbations. Events of greater depth can be explained using “on-path” trimp mechanisms [Tolstoy et al., 1986]. Both mechanisms can produce positive and negative events, and in particular [Tolstoy et al., 1986] show how the sign and depth of an event depends on distance from the receiving station (see Figure 2.12). In view of this it is somewhat surprising that only negative trimpis are observed at SANAE.

There seems to be a level of 3% to 4% of events at each depth due to “on-path” precipitation patches, enhanced by echo trimpis for small perturbation events, which are more numerous since they can affect a signal path over a wider area [Dowden and Adams, 1988]. This could explain the observation of [Leyser et al., 1984] that most events occur within ≈ 1000 km of the receiving station, since the power re-radiated by off-path precipitation patches is weak and falls off rapidly with distance.

Figure 3.9 gives the frequency of occurrence of events in local time ignoring the intervals for which there was less than 5 hours of data (see Figure 3.3).

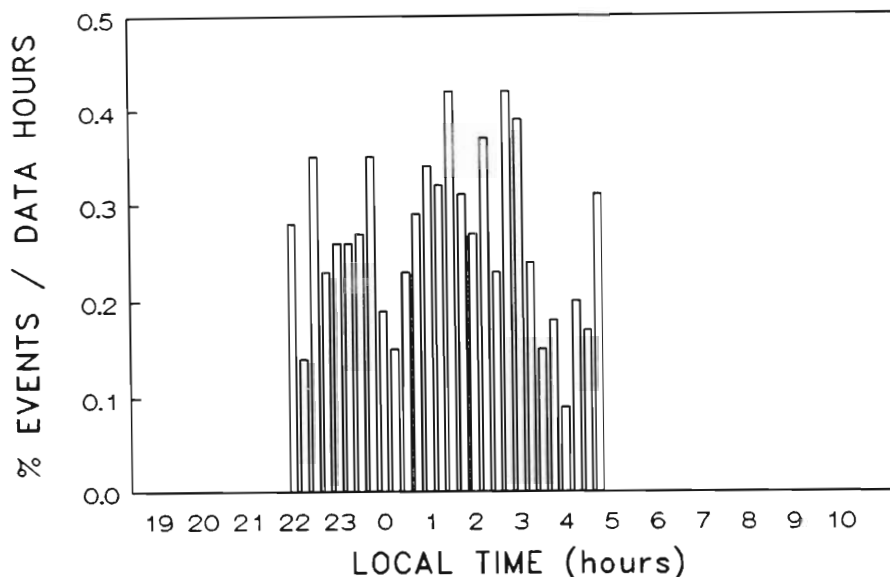


Figure 3.9: Distribution of trimpi events in local time in 15 min intervals (4 per hour) normalised with respect to total data hours available in each bin

For all times the signal paths were in darkness for at least 3000 km from SANAE and thus in principle equally susceptible to trimpi precipitation. The frequency of occurrence has a well defined minimum between 0330 and 0430 and a secondary minimum between midnight and 0100 hours. [Helliwell et al., 1973] reported a minimum in occurrence at Siple around midnight. The surprising fact here is that the frequency of occurrence does not follow the diurnal variation for the occurrence of whistlers which has a pre-dawn maximum [Helliwell, 1965], considering the established links with whistlers in the trimpi scenario.

Another feature of the data may be seen by grouping trimpis observed on the paths from the North American stations which approach SANAE from the west and comparing them with trimpis observed on the transmitter paths from Europe. In so doing this we find that the rate of occurrence of trimpis on the North American paths is about 2.4 per hour as against 3.5 per hour on the paths from Europe. The interesting aspect of this is that it is well known that the majority of whistlers observed at SANAE arrive from the west of the station [Ladwig and Hughes, 1989] and thus we might expect a greater frequency of occurrence of trimpis on the signals from North America than on signals from other directions.

A possible explanation of these facts is that the whistlers observed on the ground which determine the occurrence in arrival direction and which would have been used in the [Ladwig and Hughes, 1989] study are ducted whistlers while trimpi events may be caused by both ducted and non-ducted whistlers.

It is tempting to suggest that the high frequency of occurrence of trimpis on the Jim Creek transmitter (Figure 3.10) may be related to the fact that its path to SANAE skirts the South Atlantic Anomaly on its western side where conditions in the magnetosphere are more favourable to wave particle interaction and thus to the production of trimpis precipitation. It should however be noted (Figure 3.2) that the frequency of occurrence of trimpis for this transmitter is based on only 2.2 hours data and the result may not therefore be significant.

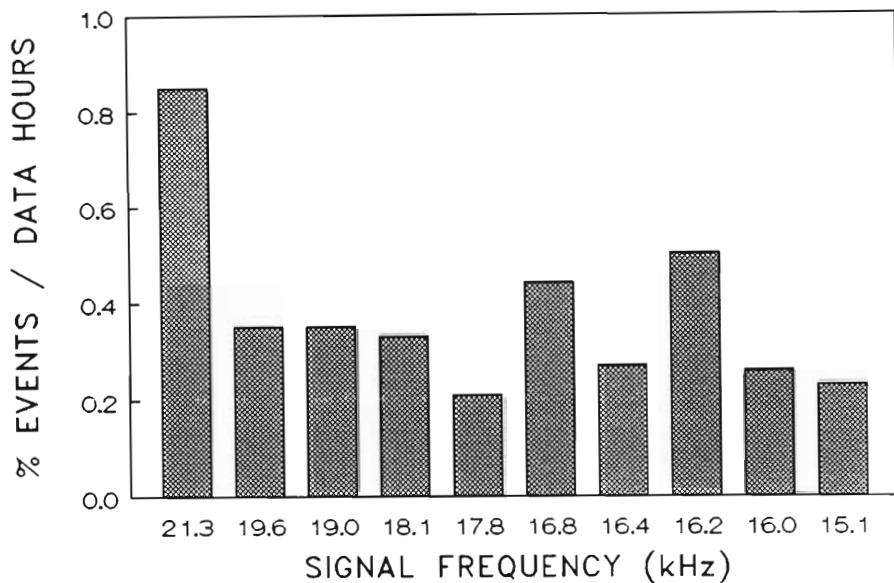


Figure 3.10: Distribution of number of trimpis events at each observed frequency normalised with respect to data hours available at each frequency

3.5 The Causative Whistler

The absence of detectable whistlers associated with trimpis events observed at SANAE may indeed be due, as we have suggested, to the fact that many of the trimpis observed are caused by whistlers which do not penetrate the ionosphere. There are however other factors which ought to be considered:

- (a) For cyclotron resonance at a given frequency the resonant electron energy decreases with increasing electron density [Kennel and Petschek, 1966] thus, given the normal energy spectrum of energetic electrons in the magnetosphere, wave growth is greater and particle precipitation more likely inside the plasmopause than outside. Now since our observations were made at magnetically disturbed times when the plasmopause would have been well north of SANAE it is conceivable that had whistlers been present they might well have exited from the ionosphere at some distance from SANAE

and thus have been too weak to be observed, their attenuation also being increased by increased ionospheric absorption.

- (b) It should also be noted that whistler activity is generally low at SANAE [Smith et al., 1991a] and this in itself is consistent with the low frequency of occurrence of trimpis. Between 2 and 6 trimpis per hour are observed compared with rates of 80 per hour reported by [Helliwell et al., 1973] for Siple.

A possible explanation for the absence of causative whistlers is that the wave-particle interaction responsible for the trimpis event either takes place with non-ducted whistlers, or that most or all of the whistler energy is reflected at the southern mirror point and is too weak to be detected at SANAE. For large events, which indicate an interaction of the VLF signal with a large precipitation patch, a non-ducted interaction is likely since in that case precipitation is not confined to a narrow field aligned duct but can take place over a range of L-shells producing precipitation over a large area. Figure 3.11 depicts this case, with the whistler mode wave crossing several L-shells and causing some precipitation along each field line it crosses.

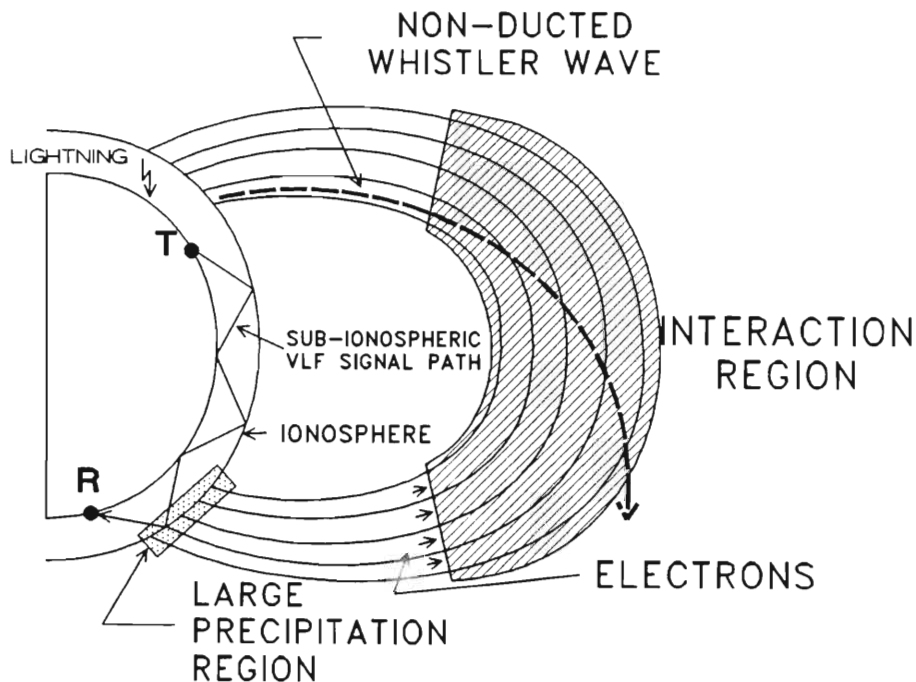


Figure 3.11: Scenario for a large trimpis event. Here the wave particle interactions are between non-ducted whistler mode waves and energetic electrons, across several L-shells near the equator

In this scenario electrons travelling northward precipitate in the southern hemisphere after being mirrored. This is likely due to the lower mirror points in the southern hemisphere. A problem with this explanation is the fact that the inter-

action time of the whistler on any given field line is shorter, thus leading to less precipitation along each field line, even though it is spread out over a larger area. However, if we consider a whistler group, which is spread out over several field lines, which becomes unducted before passing through the equatorial region (the main interaction region [Inan et al., 1978]) then it is perhaps possible to have a large region of substantial precipitation. [Hurren et al., 1986] also suggest that non-ducted waves that are internally reflected within the magnetosphere may be the cause of trimperturbations which are not associated with an observed whistler.

3.6 Location of WIEP Regions

The method we use to locate the precipitation region uses simple geometric considerations based on established features of trimperturbations. Ignoring "shallower" trimperturbations caused by echo events (perturbations of less than 2dB or 20%) [Dowden and Adams, 1988] large amplitude events can be considered to be caused by WIEP on or very near the transmitter path. Since events are only observed in the nighttime ionosphere [Leyser et al., 1984], the signal path must lie in darkness at ionospheric reflection altitudes. Trimperturbations have been firmly linked with whistlers [Helliwell et al., 1973], [Lohrey and Kaiser, 1979], thus the L-value of the accompanying whistler yields a line of geomagnetic latitude (at ionospheric heights, D-layer \approx 80km) along which the field-aligned electrons precipitate.

Plotting the day/night divider at the time of an event, the L-shell and signal paths then define the location of an event. When one has a large number of close signal paths available (as is the case for the paths to SANAE from European transmitters, see Figure 3.1 the common occurrence of events on adjacent paths indicates the extent of the precipitation region.

Unfortunately this method relies heavily on the observation of a single causative whistler, which was notably absent for the data observed at SANAE. The determination of the correct L-shell for a trimperturbation caused by a whistler group is problematic and for unducted whistlers impossible. A search for observable whistlers associated with events of 30% depth or more yielded only three very weak whistlers. VLF activity at SANAE during aurora displays is normally very low, with whistlers being very rarely observed [Stephenson, 1989]. Applying our method to these events yielded precipitation regions confined to as little as 10 km in longitudinal extent. However this requires further study as only 0.8% of the events tested showed a possible causative whistler.

3.7 Summary of Results

A new template matching and data collection method was used to extract trimpi events from tape recorded data, discriminating against spurious events to a high degree of confidence.

It is found that non-ducted whistlers may play a role in the production of trimpi events for the following reasons:

- (a) The Local Time patterns of occurrence of trimpi events do not correspond to the patterns of occurrence of whistlers observed at SANAE. The whistlers observed at ground stations are usually considered to have been ducted.
- (b) The causative whistler is rarely seen at SANAE.
- (c) It has been established [Ladwig and Hughes, 1989] that the majority of whistlers received at SANAE exit from the ionosphere to the north-west of the station. We might therefore expect, if trimpi events are produced only by ducted whistlers, that most events would occur on signals from North American transmitters. We find, within the limits of our statistics, that trimpis occur less frequently on the propagation paths from North America.

The occurrence statistics of the events at SANAE and the frequent absence on simultaneous broadband VLF records of the causative whistler suggest that interactions with other than ducted whistler mode waves play a significant role in producing trimpi events and in particular may be responsible for the huge amplitude perturbations.

The use of a simple geometric method to determine the location and extent of WIEP ionisation has been demonstrated. The main limitation of the method is that it can only be applied in a few specialised cases for which several paths cross the precipitation region, all the required transmitters are active at the time of an event and the causative whistler can be identified. The application of this method to the present data set was extremely limited.

The uniqueness of a particular receiving location when it comes to the observation of trimpi events is again evident. Specific features of the SANAE location are:

- (a) The absence of positive trimpis and causative whistlers.
- (b) A preference for short duration events.
- (c) The occurrence of some very large events.
- (d) Two lows in trimpi occurrence near 0015 and 0400 hours LT.
- (e) Low occurrence and occurrence rate of events.

- (f) An indication that for many of the events observed gyroresonant interactions with non-ducted whistler mode waves are important.

This uniqueness of location makes it very difficult to compare the results obtained at one station with another unless data from several receivers covering the same frequencies at the same time can be taken into account. Since the results here apply only to magnetically disturbed times (i.e. those periods of a substorm which lead to recordable aurorae over SANAE), part of the characteristics observed could be due to this fact rather than any special feature of the SANAE location.

Chapter 4

A System for Receiving Trimpi Events at Durban

The system used in 3.2 is developed further here to allow “live” data capture at Durban. The system described here is a multi-channel computer controlled receiver which allows the recording of (amplitude only) of up to 20 transmitter signals simultaneously.

4.1 The Receiving System

The system developed here is based on the system shown in Figure 3.4; the new system is shown in Figure 4.1. The system used for the study in chapter 3 used the analog output of the Ubiquitous Spectrum Analyser which could be set to display either the whole spectrum or a single spectrum point, and was thus limited to one frequency only. The low-pass filter and PC-28 digitiser is replaced by a model 1015 Spectrum Averager: a somewhat archaic, hardware-logic device designed to perform simple averaging of a number of spectra. It is used here because it provides an adaptable digital output for interfacing with an IBM compatible PC running a PC-14 dual 8255 digital I/O card. Off the air signals are obtained by replacing the input stage (normally tape) by a simple whip antenna and a high-gain VLF pre-amplifier. Since the input to the spectrum analyser is broadband (0–40 kHz) and limited to 0.1V RMS particular care must be taken to remove unwanted signals from the input. The receiving site used here (Roof of the Physics Department) is a particularly noisy site with strong 50 Hz power hum and harmonics. A steep notch filter at 50 Hz and a low pass filter at 40 kHz limits the signal. A pair of fast germanium diodes on the output of the pre-amp serves to clip strong spherics and keeps the input to the Ubiquitous from overloading.

Timing of data collection is done using the on-board computer clock. Figure 4.2 shows the block diagram of the timing and data collection loop.

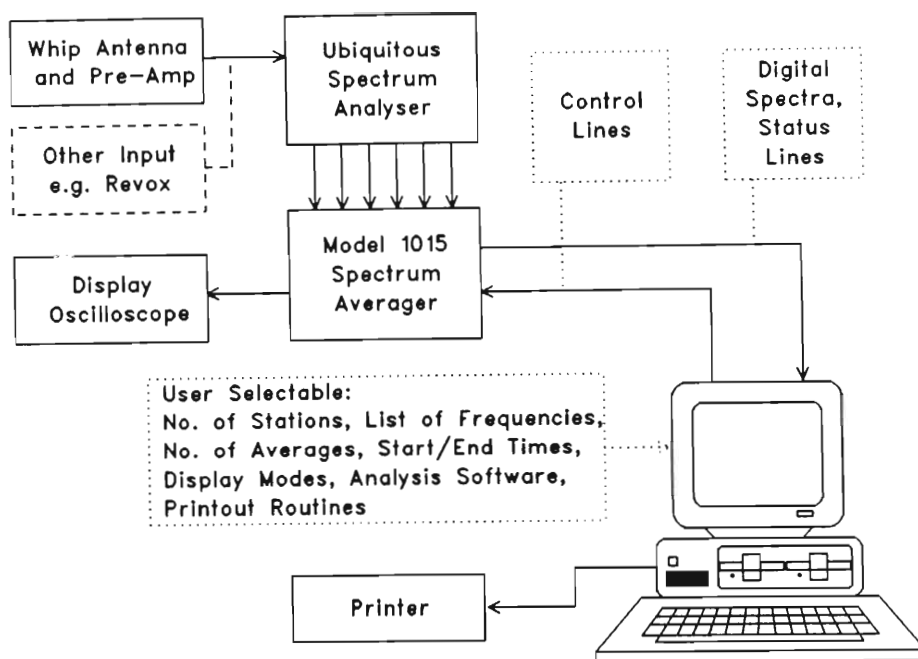


Figure 4.1: Multi-channel computerised VLF receiving system

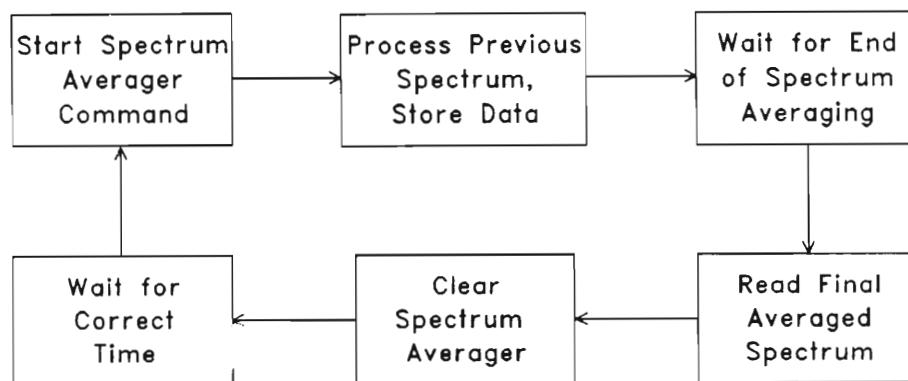


Figure 4.2: Spectrum Averager – PC timing and data collection loop

The PC issues a start spectrum averaging command and then waits for an end averaging signal from the Averager. The Averager performs a “divide first then add” function, e.g. with the number of spectra to be averaged set to 4 each spectrum read from the Ubiquitous (which produces one spectrum of 500 points every 0.05s max) is divided by 4 and then added to a stack. The averaged spectrum thus “grows” to its final value, and the process can be monitored on a display oscilloscope (see Figure 4.1). After the final spectrum has been added the end average signal is given and the averaged spectrum is then read by the PC. It subsequently takes one further spectrum loop to clear the averaged spectrum and reset the Averager for the next averaging cycle. The limitation of this system

is that it always takes two more spectrum times than the number of spectra averaged to perform one cycle, effectively dividing the maximum time resolution of the Ubiquitous Spectrum Analyser by three. This, however, becomes less noticeable at higher averaging numbers. Table 4.1 shows a comparison between the minimum free running Ubiquitous Spectrum Analyser time between spectra and the times available after averaging. The last column shows the chosen timing times for the PC timing and data collection loop, round Figures are chosen here for convenience.

No. of Spectra	Ubiquitous alone (s)	Averager & readout (s)	PC timing loop (s)
1	0.051	0.154	0.25
4	0.204	0.306	0.50
16	0.816	0.918	1.00
32	1.632	1.734	2.00
64	3.264	3.369	4.00
128	6.528	6.631	8.00
256	13.056	13.156	15.00
512	26.112	26.223	30.00
1024	52.224	52.324	60.00

Table 4.1: Maximum spectrum rates available for different averaging settings

Thus the software allows data collection rates of averaged spectra ranging from 4 Hz to one spectrum a minute. The advantage of using long averages is that the signal to noise level is improved, and signals that are normally invisible in the noise are now visible. This is useful for identifying stations and monitoring their signal strength over long periods, but limits the time resolution needed for the detection of trimp events.

While the PC “waits” for the end of averaging to occur it utilises this time to process the last spectrum read. A look-up table of pre-selected frequencies is used, and each frequency point is averaged over 3 spectrum points weighted 0.5, 1, 0.5 respectively. The data thus extracted is stored and written to disk periodically. The system is very flexible in allowing the user to pre-select sets of frequencies to be collected at various averaging rates over various periods.

The existing data display software from the study in chapter 3 was extended to allow the display and printing of up to six frequencies simultaneously. All other software routines (digital filtering, smoothing, trimp detection) as written for the analysis in chapter 3 can be used on this data as well.

4.2 Data Source

A large number of VLF/LF transmitter signals are detectable at Durban, although some are barely above the noise level of the equipment used here. Details

of the more common VLF/LF transmitters received in this study are given in Table 4.2 and their great circle paths to Durban are drawn in Figure 4.3.

F (kHz)	CALL-SIGN	STATION	LONGITUDE	LATITUDE
36.55	???	Jeloey	010°36'E	59°26'N
32.00	???	Hanjiang	110°25'E	21°12'N
30.85	???	Mexico DF	099°08'W	19°26'N
28.50	???	Ft. Allen	066°30'W	18°25'N
24.00	NBA	Balboa	079°39'W	09°03'N
22.30	NWC	N-W Cape	114°09'E	21°48'S
21.40	NSS	Washington DC	076°27'W	38°59'N
19.60	GBZ	Anthorn	003°30'W	55°00'N
19.00	GQD	Criggion	003°04'W	52°43'N
18.60	NLK	Seattle	122°15'W	47°42'N
18.10	UPD8	Murmansk	033°05'E	67°58'N
16.80	FTA2	S Assise	002°35'E	48°33'N
16.00	GBR	Rugby	001°11'W	52°22'N
13.00	Ω	Australia	146°56'E	38°29'N
12.90	Ω	Argentina	065°11'W	43°03'N
12.30	Ω	LaReunion	055°17'E	20°58'S
12.00	Ω	Liberia	010°40'W	06°18'N

Table 4.2: List of VLF/LF transmitters observed at Durban in 1990

The paths cover a wide area around Durban and are potentially useful for joint studies with overlapping paths (see 8.3.2) and the OMSKI system (see chapter 6).

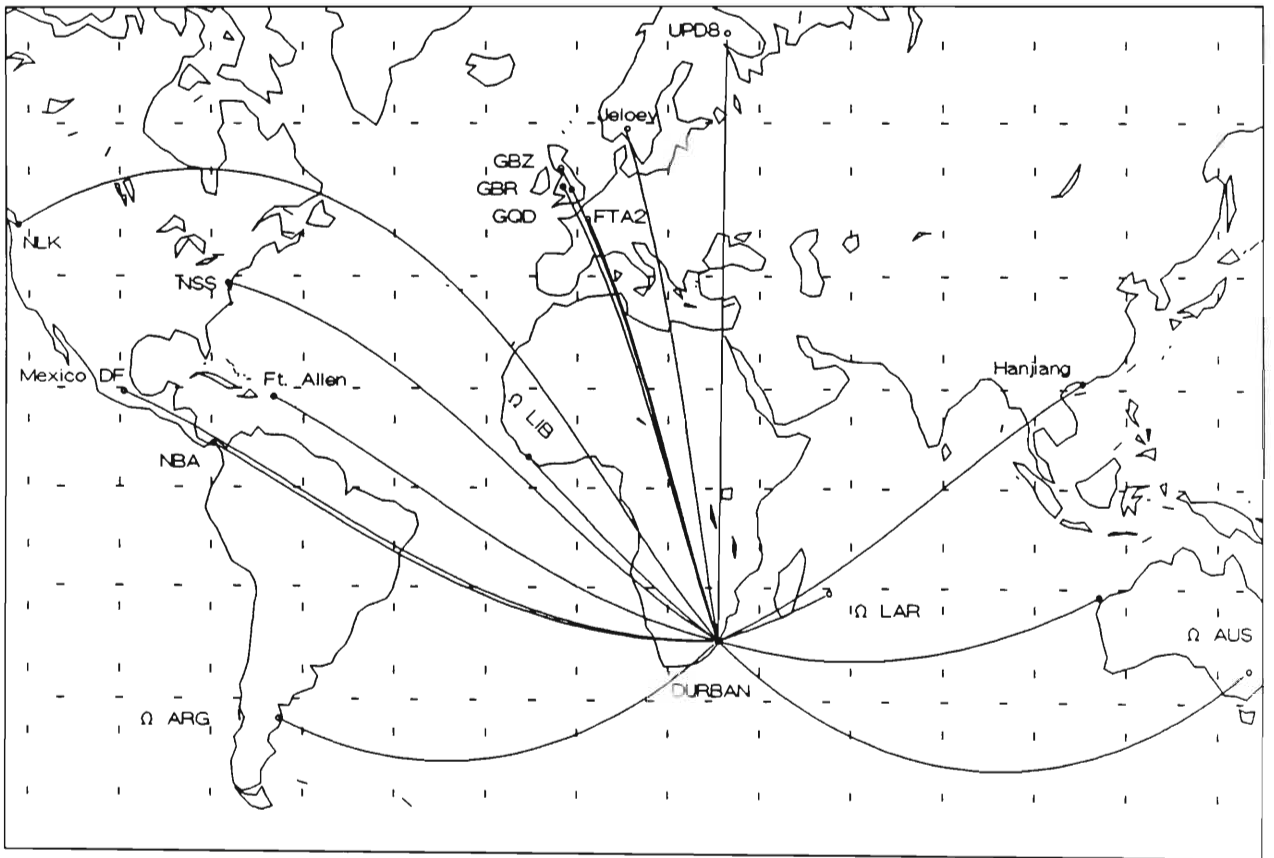


Figure 4.3: Great circle paths from VLF transmitters to Durban in 1990

4.3 Problems

The system as it stands suffers from various difficulties which only allow limited use for trimpi work:

- (a) Since the input to the Spectrum Analyser is broadband a range of unwanted signals and noise contribute to the 0.1V RMS maximum input signal strength, limiting the amplification of the signal in order to improve the signal strength of wanted signals. This is a basic limitation of a broadband device.
- (b) The bandwidth of the individual spectrum points is defined as

$$\beta = \frac{\text{frequency range}}{500 \text{ spectrum points}}$$

and here $\beta = 80$ Hz. Thus as a receiver the system is not very selective. This makes individual signal detection very noisy.

- (c) Using the longer averages improves S/N ratio but at the expense of time resolution.
- (d) The overall system is not suited to detect trimpi events of amplitude changes less than about 1 dB even at times when strong signals received are amplitude stable. Too much noise is added to the signal by the equipment used.
- (e) Phase variations on the signals are not detected. This further reduces the sensitivity of trimpi detection, since phase events can be quite distinct even on noisy signals.

The actual data collected with this system is limited to the developmental period from October 1989 to March 1990. The system was not used for a full recording campaign, and a total of only 11 days of data were collected. Further work on this system was abandoned after that for various reasons:

- (a) Very few trimpi events were detected given the limitations described,
- (b) A new receiver system (OMSKI, see chapter 6) had been on order from New Zealand since August 1989 and was expected to arrive soon
- (c) The system as described here was being dedicated to a new task: The production of hardcopy “Quicklook” VLF spectrogram data using a laser printer. Existing tape records of SANAE VLF recordings are being processed by this system (currently 1989) data. A report on this system appeared in [Friedel and Smith, 1991].

4.4 Example of Data

Even though the number of events detected with this system is small (15) important new characteristics emerged. These events represent the first trimpi events found at such low L -values, and in particular some daytime events were found, making these the first such events observed. These events were observed on the Ω -La Reunion and NWC to Durban paths. Figure 4.4 shows a map of these paths together with the L -shells they cross.

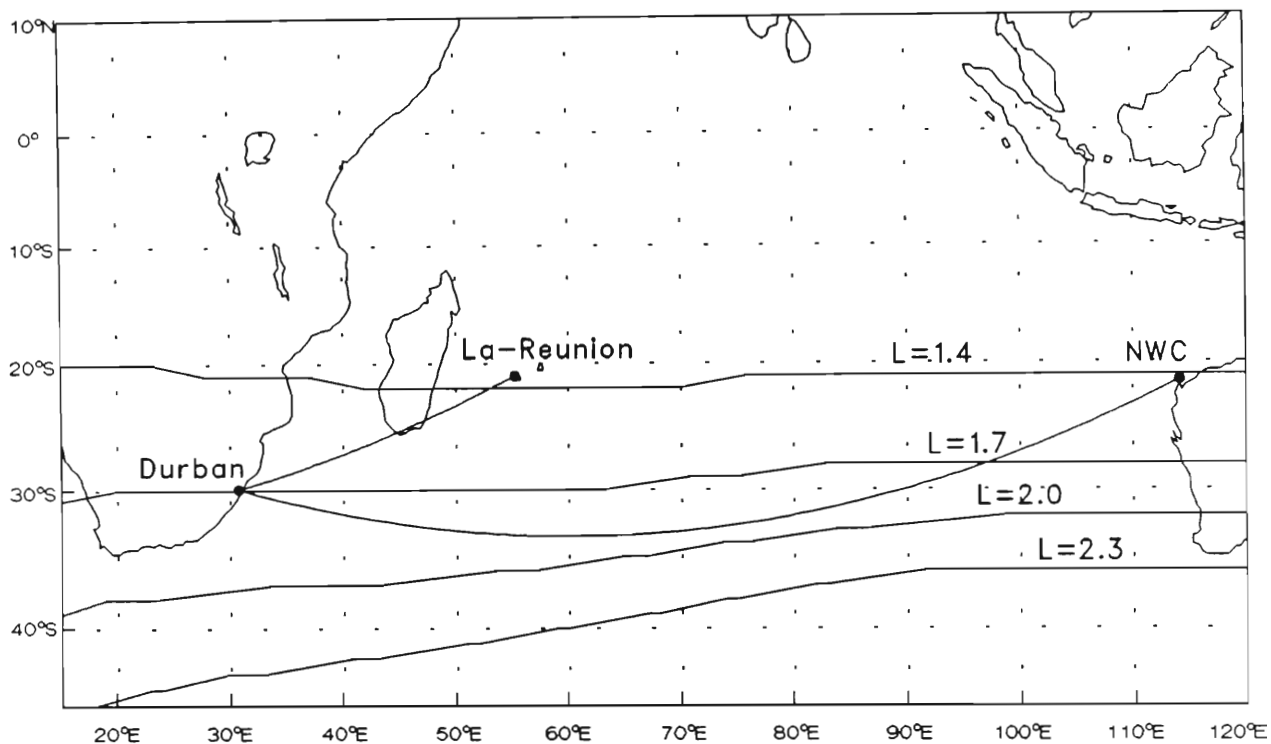


Figure 4.4: Low-latitude transmitter paths to Durban ($L=1.7$, 29°S 32°E) from NWC ($L=1.45$, 22°S 114°E) and La-Reunion ($L=1.36$, 21°S 55°E). Some L -shells in the vicinity of these paths are indicated

Figure 4.5 shows an event occurring at 13:24:24 UT with a recovery time of ~ 30 s - a time for which the whole of the path is in sunlight (the path lies between $L=1.36$ and $L=1.7$). This is particularly interesting since for the ionosphere to be perturbed at VLF reflection heights in the ionosphere during the day, the precipitating fluxes must be of high energy and very intense, suggesting strong pitch angle scattering. The problems concerning the trimpi mechanism (and gyroresonance in particular) at low L are discussed in chapter 5 and daytime events are further discussed in section 6.4.4.

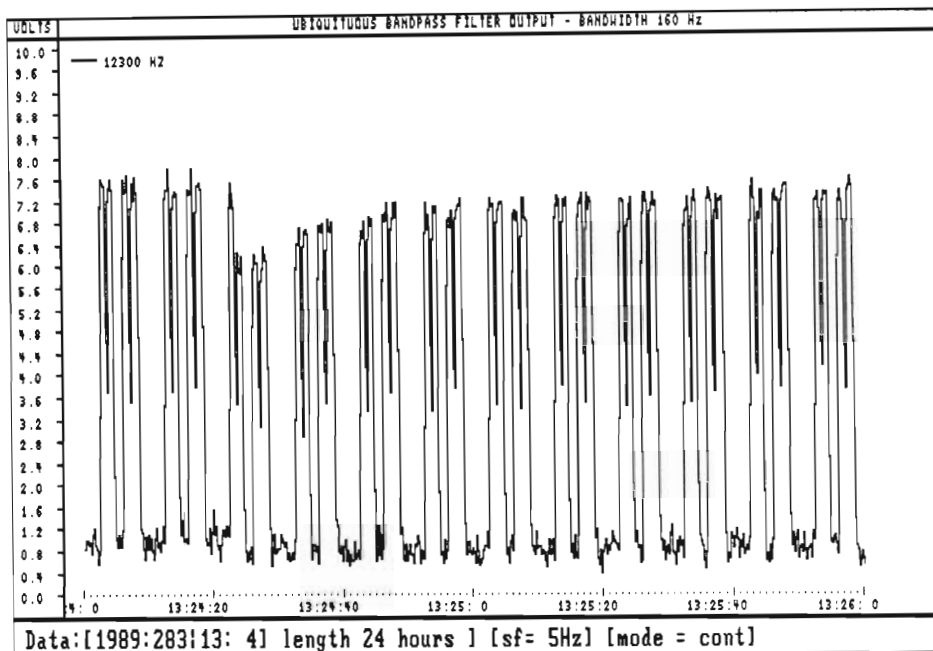


Figure 4.5: Trimp event observed at Durban on OMEGA signal from La-Reunion. On day 283 (October 10, 1989) at 13:24:24 UT (LT = UT+2hr). The signal (12.3 kHz, Ω La Reunion unique frequency) shows the typical OMEGA on/off modulation (see Figure 6.1)

4.5 Uses for this System

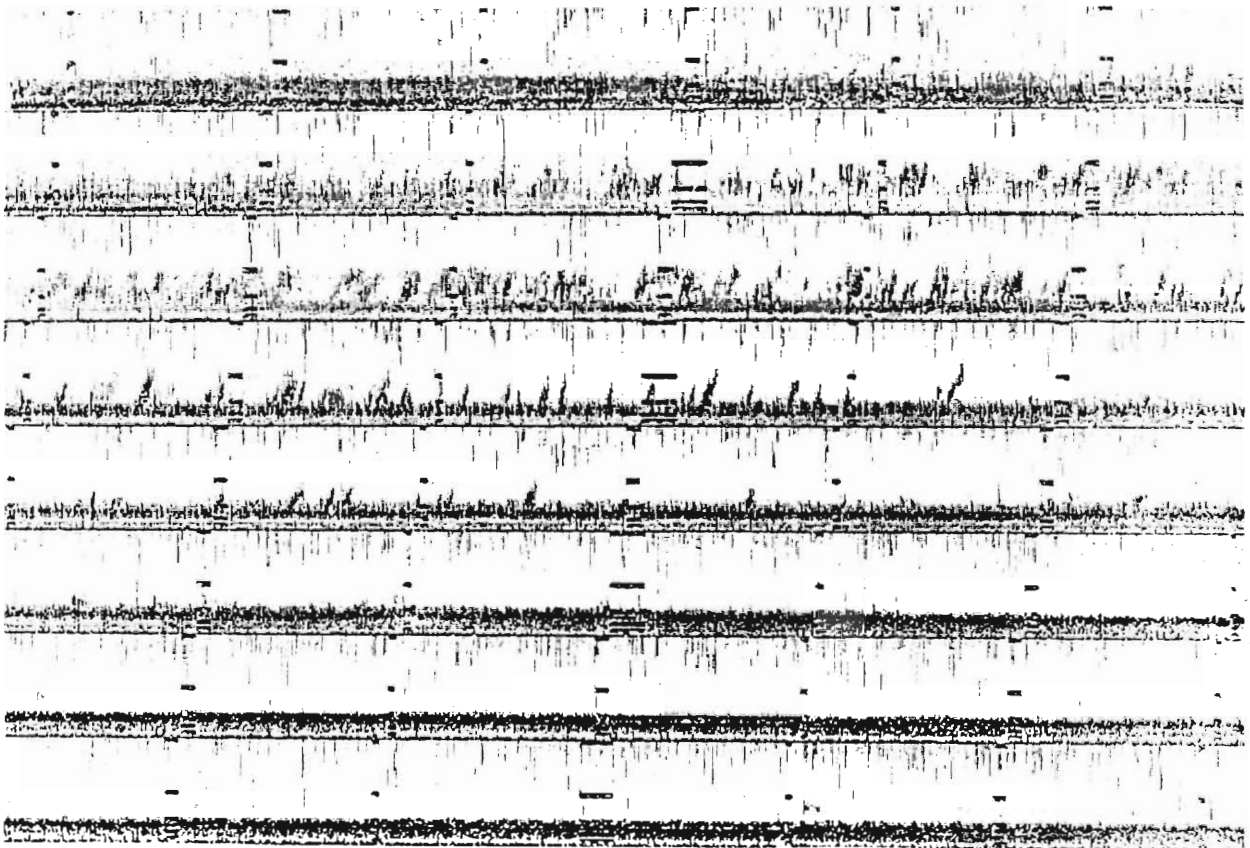
This system was originally designed to record trimp events on VLF signals. However for the reasons mentioned in section 4.3 its use in trimp work is severely limited. Since a large amount of work was invested in the hardware and software development of this system it is still being used for other purposes:

- (a) When using the averaging feature the system is very useful in identifying VLF signals and monitoring a large number of them for their overall signal strength and their transmission schedule. This information is vital in planning the frequency selection and data logging schedule of the OMSKI equipment (see chapter 6).
- (b) As a multi purpose VLF analysis tool for recorded data. The implementation here selects a range of individual frequencies, but any portion of the

spectrum can be extracted.

- (c) For the production of VLF "Quicklook" data. An example of a hardcopy of four hours of synoptic tape data produced in this format is shown in Figure 4.6. This format is useful for scanning the VLF activity of a large volume of data [Friedel and Smith, 1991].

VLF Quicklook Data - 0 kHz to 8 kHz



SG(s) 89 TAPE-342 SIDE-2 BEGAN: DAY318 TIME-08:10

Figure 4.6: Example of VLF "Quicklook" data produced with this system. SANA E data from 1989 one in five recordings, day 318 from 08:10–12:10 UT. Each panel shows spectra in the 0–8 kHz range. The horizontal lines are fixed frequency calibration signals occurring every minute, with longer bars every 10 min and the longest every hour

Chapter 5

Trimpi Events on Low Latitude Paths: Investigation of Gyroresonance at Low L -values

Most of the studies investigating gyroresonance and its relation to trimpi events were carried out for high or middle latitudes: [Potterma and Rosenberg, 1973], [Inan et al., 1988c] for $2 < L < 4$ or near $L = 2$ [Leyser et al., 1984] where the resonant electrons are non-relativistic ($E_k < 50$ keV). For $L < 2$ the topography of the magnetosphere, the resonance condition for the interaction, and the energetic particle distributions are significantly different: the magnetic field is more “curved” and this decreases the size of the region in which (effective) resonance can occur; electrons resonating with VLF waves have relativistic velocities - this decreases the interaction time; and the fluxes of trapped particles near resonance are lower than at higher L .

There have been observations of low-latitude electron precipitation (36–317 keV) due to VLF transmitter action in the region of $1.5 < L < 2.0$ [Vampola, 1983], and a 1 MeV precipitation burst has been related to the recovery signature of trimpi events occurring on paths below $L=2$ [Inan et al., 1988a]. Narrow energy peaks in electrons precipitating from the inner radiation belts have been reported [Imhof et al., 1981, Datlowe and Imhof, 1990], showing that the energy peak value behaviour with L -value is in general consistent with first order gyroresonance near the equator over the interval $1.5 < L < 1.85$. Significant deviations from this are, however, also observed. Since it is established that gyroresonance also leads to the precipitation of electrons at L -values below $L=2$, one must ask the question if such an interaction can be efficient enough to cause trimpi events, and since it is established that lightning strikes are the source of the interacting VLF waves [Inan et al., 1988b], have these waves got the required characteristics in frequency and amplitude to be effective at low L ?

The question raised here becomes even more significant in the face of evidence from the studies in Chapter 4 which reports on the first low latitude trimpi events

observed at Durban, and of chapter 6 which reports on the first results from the OMSKI project at Durban. Both these studies also showed the occurrence of daytime triumpi events, the significance of which is examined further in section 6.4.4.

Early test-particle studies of the gyroresonance interaction have examined the region around $L=4$ [Inan et al., 1978], non-relativistic treatment, and were extended to $2 < L < 4.5$ by [Chang and Inan, 1983], quasi-relativistic treatment and further [Chang and Inan, 1985], relativistic treatment. In this chapter results of a test-particle simulation of the interaction for $1.2 < L < 2.0$ are presented, and the parameter ranges which lead to an effective pitch angle change is defined. Since one of these parameters (for B_w , the wave intensity) turns out to be fairly large (~ 200 pT), the characteristics of the causative lightning is examined to determine if it can be the source of the high wave intensities required.

5.1 The Relativistic Gyroresonance Condition

The physics of basic the gyroresonance mechanism have been presented in section 2.2.5. For the wave particle interaction considered here $m = 1$ in equation 2.20 for cyclotron resonance. The effect of relativity here is to decrease the electron gyrofrequency due to the relativistic mass increase at high energies. The resonance condition can then be written (equation 5.1):

$$\omega_w - k \cdot v_{\parallel} = \omega_H / \gamma \quad (5.1)$$

Cumulative pitch angle changes occur only at or very near resonance and in general depend on the variables shown in Table 5.1.

Wave	: ω_w, B_w, k	(and thus $\omega_p(n_e)$)
Particle	: $v_{\parallel}, \alpha_{eq}, \omega_H$	(and thus B_0),
Relativistic Correction	: γ	(and thus E_k or v).
Wave/particle phase	: ϕ_0	

Table 5.1: Variables influencing gyroresonance

In Table 5.1 k is the wave number, ω_w is the whistler wave frequency, ω_p is the electron plasma frequency, ω_H is the electron gyrofrequency, n_e is the background electron density, B_0 is the background magnetic field, α_{eq} is the equatorial pitch angle, γ is the relativistic correction factor (equation 5.15), E_k is the total particle energy, and v is the particle velocity. The phase ϕ is the angle between particle and wave vectors, defined as the angle between v_{\perp} and $-B_w$. The initial phase ϕ_0 is the angle at which wave and particle first encounter each other and is critical in deciding the sign and size of the pitch angle change (see Figure 5.5).

5.1.1 Derivation of Relativistic Correction

Equation 5.1 looks deceptively simple, however the modification due to γ is by no means obvious. Consider two frames, a background plasma frame Σ and an electron frame Σ' moving with the electron parallel velocity v_{\parallel} so that the electron guiding center is at rest in that frame (see Figure 5.1).

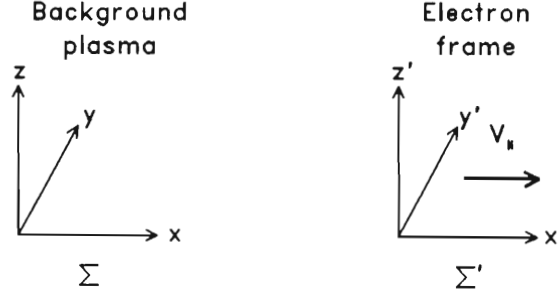


Figure 5.1: Plasma and electron frames of reference

If one considers cyclotron resonance with a circularly polarised wave travelling in the background plasma with phase velocity $v_p \ll c$, in the x -direction, then the polarised wave may be split up into two perpendicular y and z components:

$$\begin{aligned} y &= y_0 \sin(\omega t - kx) \\ y &= y' \\ \omega t - kx &= \omega' t' - k' x' \end{aligned} \quad (5.2)$$

The dash in equations 5.2 refer to the Σ' frame. Now let $x' = 0$, $x = v_{\parallel} t$ for resonance and $k = \frac{2\pi}{\lambda} = \frac{2\pi f}{v_p}$, then equation 5.2 becomes:

$$f t - \frac{f}{v_p} v_{\parallel} t = f' t' \quad (5.3)$$

To relate t' in frame Σ' to t in frame Σ the Lorentz transformation can be used:

$$t' = \gamma_{\parallel} \left(t - \frac{x v_{\parallel}}{c^2} \right) = \gamma_{\parallel} \left(t - \frac{t v_{\parallel}^2}{c^2} \right) = \frac{\gamma_{\parallel} t}{\gamma_{\parallel}^2} = \frac{t}{\gamma_{\parallel}} \quad (5.4)$$

where γ_{\parallel} is given by equation 5.5

$$\gamma_{\parallel} = \sqrt{1 - \frac{v_{\parallel}^2}{c^2}} \quad (5.5)$$

Substituting equation 5.4 into 5.3 yields

$$f - \frac{f}{v_p} v_{\parallel} = \frac{f'}{\gamma_{\parallel}} \quad (5.6)$$

and after rearranging and noting that for resonance $f' = f'_H$, the electron gyrofrequency as viewed from Σ' .

$$v_{\parallel} = -v_p \left[\frac{f'_H}{\gamma_{\parallel} f} - 1 \right] \quad (5.7)$$

The relativistic correction affects f'_H through the electron mass and the particle perpendicular velocity v_{\perp} . If m_0 is the electron rest mass then

$$f'_H = \frac{eB}{m_0} \sqrt{1 - \frac{v_{\perp}^2}{c^2}} \quad (5.8)$$

Applying the Lorentz transformation again yields $v'_{\perp} = \gamma_{\parallel} v_{\perp}$. Using this in equation 5.8 together with $v^2 = v_{\parallel}^2 + v_{\perp}^2$ yields after a few steps

$$f'_H = \frac{eB}{m_0} \frac{\gamma_{\parallel}}{\gamma} = f_H \frac{\gamma_{\parallel}}{\gamma} \quad (5.9)$$

Substituting equation 5.8 into equation 5.7 and allowing for counterstreaming electrons for gyroresonance with whistler mode waves ($v_{\parallel} \rightarrow -v_{\parallel}$) yields

$$v_{\parallel} = v_p \left[\frac{f_H}{\gamma f} - 1 \right] \quad (5.10)$$

Equation 5.10 is just another way of writing the resonance condition (using $\omega = 2\pi f$) in equation 5.1. From 5.10 it can be seen that v_{\parallel} increases with a decrease in frequency. This is due to the lower phase velocity of the whistler wave at lower frequencies, requiring a larger doppler shift. For a given frequency the resonant velocity increases sharply as one goes from inside to outside the plasmopause ($v_{\parallel} \propto v_p$ at given f) - which decreases the likelihood of gyroresonant interactions outside the plasmopause. There is a direct dependence of v_{\parallel} on the electron gyrofrequency, which increases as B increases leading to larger v_{\parallel} at low L .

5.1.2 Dependence of Resonance Condition on L -value

The resonant electron velocity at a given frequency depends on the local magnetic field strength and the particle pitch angle. The most favourable conditions for resonance are at the magnetic equator. Here the particle pitch angle is smallest and thus the resonant velocity is obtained from particles with the lowest possible total energy. Because electron number density increases with decrease in total

energy the greatest number of electrons are resonant at the equator. In addition the magnetic field strength varies more slowly in the vicinity of the magnetic equator and therefore the electron remains in resonance for a longer time.

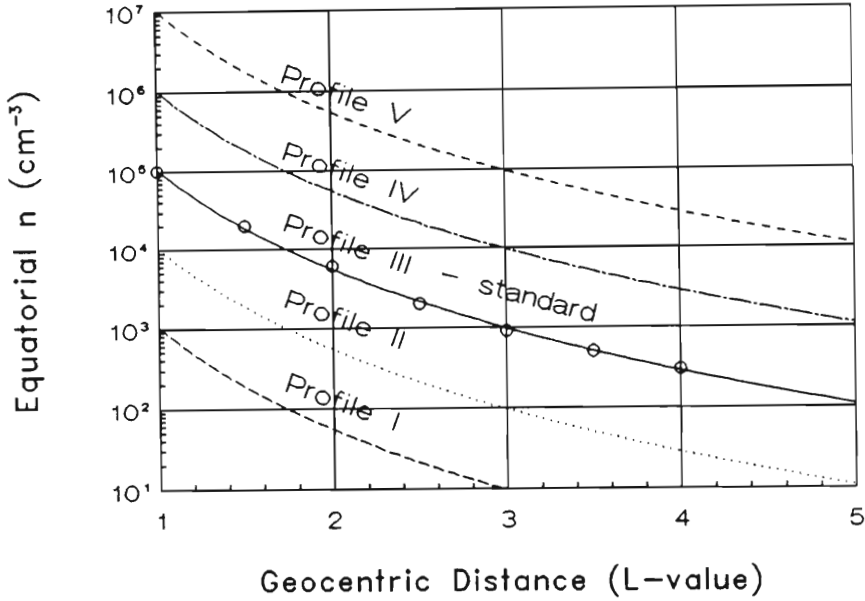


Figure 5.2: Simple equatorial electron density (n_{eq}) model from satellite observations Carpenter and Smith, 1964, profile III scaled up and down by two orders of magnitude to give five profiles I – V. The curve fit equation used here is $n_{eq} = 10.5 \times 10^4 \times L^{-4.26} \text{cm}^{-3}$ (profile III)

A simple equatorial electron density model ([Carpenter and Smith, 1964], figure 5.2, Profile III) and equation 5.1 is used to calculate the relativistic parallel resonant velocity and corresponding energy as a function of L -value at low L . Figure 5.3 shows the results of this calculation for several wave frequencies, for electrons on the loss cone, resonant at the magnetic equator. For $v_{||}$ equal to the resonant velocity $v_{||} \rightarrow v_r$.

Two curves are plotted for each frequency, for the resonant velocity v_r and the corresponding resonant energy E_k . v_r increases at first with decreasing L , but at low enough L the relativistic reduction in ω_H decreases the resonant velocity. E_k increases as L decreases, showing required resonant energies in the MeV range at very low L . Note the lowering of both v_r and E_k with increased frequency (higher $\omega_w \rightarrow$ less doppler shift required \rightarrow lower resonant velocity \rightarrow thus lower particle energies), and the fact that at low L higher frequencies (> 10 kHz) are also resonant (at higher L high frequencies are above the whistler cut-off frequency of $f_H/2$). This potentially increases the possible particle population in resonance at low L : A larger range of energies can “pick” their right resonant frequency at any one time. Further, this decrease of v_r at low L also means that the interaction times are longer, thus also potentially increasing the scattering efficiency.

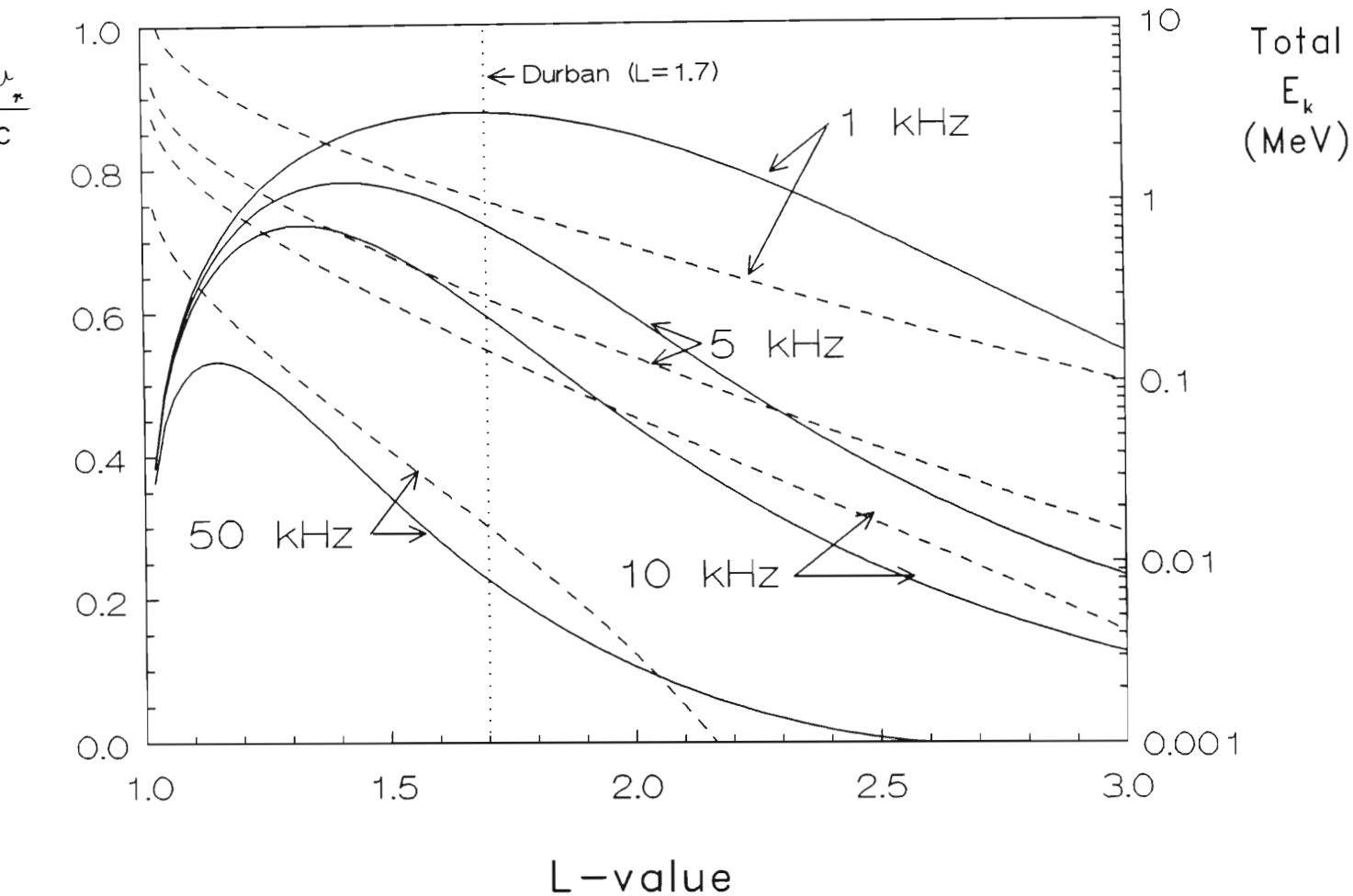


Figure 5.3: Relativistic resonant velocity (v_r/c , left axis, smooth curves) and total resonant energy (E_k , right axis, dashed curves) as a function of L -value for particles on the loss cone, at the equator. For frequencies 1, 5, 10 and 50 kHz

5.2 The Relativistic Equations of Motion

The basic equations have been derived by Inan et al. [1978] and the relativistic modifications were made by Chang and Inan [1983]. A derivation of these equations is included in appendix A for reference. The equations used here are basically the same as those used before [Chang and Inan, 1983].:

$$\frac{dv_{\parallel}}{dt} = \left(\frac{eB_w}{m\gamma} \right) v_{\perp} \sin \phi - \frac{v_{\perp}^2}{2\omega_H} \frac{d\omega_H}{dz} \quad (5.11)$$

$$\frac{dv_{\perp}}{dt} = \left(\frac{eB_w}{m\gamma} \right) \left(v_{\parallel} + \frac{\omega}{k} \right) \sin \phi + \frac{v_{\perp} v_{\parallel}}{2\omega_H} \frac{d\omega_H}{dz} \quad (5.12)$$

$$\frac{d\phi}{dt} = \left(\frac{\omega_H}{\gamma} \right) - \omega - kv_{\parallel} - \left(\frac{eB_w}{m\gamma} \right) \left(v_{\parallel} + \frac{\omega}{k} \right) \frac{\cos \phi}{v_{\perp}} \quad (5.13)$$

$$\gamma = \frac{1}{\sqrt{1 - v^2/c^2}} \quad (5.14)$$

$$v^2 = v_{\parallel}^2 + v_{\perp}^2 \quad (5.15)$$

$$\alpha = \arctan(v_{\perp}/v_{\parallel}) \quad (5.16)$$

where ω_H , $k = f(z)$, z the distance along field line, ϕ is the angle between v_{\perp} as explained before and $-B_w$ and α is the pitch angle. These equations have been studied by [Chang and Inan, 1985] down to $L = 2$, and this current work serves both to confirm the results of the earlier studies and to extend the simulation to low L -values.

The computer simulation integrates these equations of motion along the magnetic field line using a dipole model for the background static field, and a simple R^{-4} model for the electron density variation along the field line, and a continuous (CW) whistler mode wave. The interaction is started off in resonance, at the equator, in the presence of a continuous wave. This approach is sufficient at low L , since the interaction times in general are very short so that even whistler wave packets from a lightning strike “look” continuous.

The purpose of the simulation is to study the basic effect of the controlling parameters (as defined in section 2) on the overall pitch angle change of a given electron. Only single electron trajectories are considered for this purpose, at a single frequency. In reality a whistler is made up of many frequencies, which will resonate with particles of different energies at several places along a field line. The single particle approach is sufficient to examine the overall behaviour of electrons undergoing resonance, since the behaviour of a distribution of particles can be inferred from these results. In general not only particles exactly at resonance with a given wave will interact; the wave will also interact with particles near resonance, but to a lesser degree: here the best case of one particle exactly at resonance is taken to examine the overall behaviour. Similarly a given wave will resonate with particles of various energies before and after traversing the equator. However, the interaction region for these interactions is much reduced by the increased inhomogeneity of the background field, resulting in less pitch angle change. Again the best case of the flattest field at the equator is taken. Thus the results reported here apply equally well to particles near resonance or off the equator or both, but to a lesser degree.

No attempt is made to calculate the possible fluxes of precipitating particles here, although this would be a logical extension of the current work. Examples of such calculations using the test-particle approach are found in [Chang and Inan, 1985].

The resonance criterion (the percentage within resonance) is used to determine the boundaries of the integration [Inan et al., 1978]. Particles only undergo pitch angle changes while very near or at resonance, once the particle moves out of the resonance region pitch angle changes are no longer cumulative. The only difference here is the actual criterion used; at higher L -values ($L \sim 4$) cumulative pitch angle changes occur within 5% of resonance, at $L = 1.2$ particles have to be within 1% of resonance for cumulative pitch angle changes to occur. This is a result of the increased field curvature and shorter interaction times at low L .

The simulation was run for a range of input parameters using L as the main

variable to illustrate the effect of moving to low L -values. Since the final pitch-angle change for a given set of parameters is strongly dependent on the initial phase ϕ_0 the simulation is run for a range of all possible ϕ_0 . Previous studies have used the RMS scattering to measure the scattering efficiency or a diffusion coefficient $D = \langle (\Delta\alpha)^2 \rangle / \Delta T$ (where ΔT is the time the particle remains in resonance [Inan et al., 1991]), both of which ignore the sign of the pitch angle change. A positive pitch angle change leads to an increase in pitch angle or a move away from the loss cone, whereas a negative pitch angle change leads to a decrease in pitch angle or a move towards the loss cone. Since only those particles with negative pitch angle change sufficiently large to reach the loss cone, contribute to any precipitation we need to define a new “loss-scattering coefficient” which takes this into account:

$$S_L = \frac{(\text{Area of positive scattering}) - (\text{Area of negative scattering})}{\text{Total Area}} \quad (5.17)$$

where the areas in equation 5.17 refer to the areas of the $\Delta\alpha_{eq}$ versus ϕ_0 graph below and above the $\Delta\alpha_{eq} = 0$ line respectively (see Figure 5.5). S_L will vary between +1 and -1 for all positive and all negative scattering respectively. In practice S_L lies between 0 for the linear case (small B_w) and close to -1 for the strongly trapped case (large B_w), although S_L can be positive when n_{eq} is very small (see Figure 5.9). Thus S_L is a measure of how efficient the interaction is in giving negative pitch angle change: The larger and negative S_L the more particles are scattered into the loss cone.

The RMS scattering value is retained here as an indication of how large a pitch angle change occurs, irrespective of direction; the results are presented using both parameters.

5.3 Sample Electron Trajectories

Figure 5.4 shows the behaviour of a single particle undergoing resonance. The electron is started off at the magnetic equator, with a pitch angle 1° greater than the loss cone half angle and resonant with a 4kHz wave at the equator. The pitch angle change is computed and reflected back to the equator.

The solid curve shows the change of pitch angle, showing a cumulative change initially, but once the electron moves out of the resonance region ($\epsilon > \sim 1\%$ off resonance) the pitch angle changes merely oscillate about a final net change value. The initial phase ϕ_0 here is zero. The progress of the interaction can be either measured in degrees, time or distance away from the equator.

Note here the large resonant energy (324 keV), the large B_w (200 pT) and the extremely short interaction time - cumulative changes only occur in the first ~ 4 ms. For this simulation a particle within one degree of the loss cone (dotted

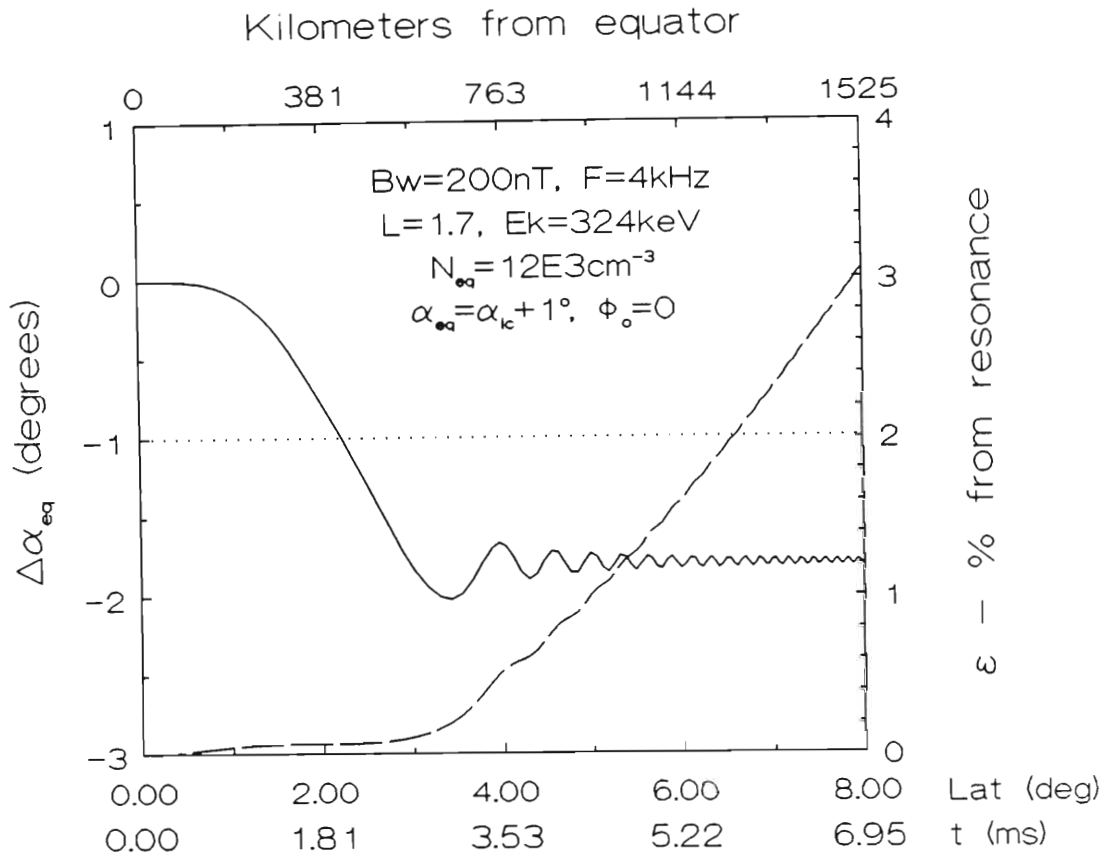


Figure 5.4: Single particle trajectory. Change in equatorial pitch angle ($\Delta\alpha_{eq}$, left axis; smooth curve) and % away from resonance ($\epsilon = \frac{|v_{\parallel} - v_r|}{v_r} \times 100$, right axis; dashed curve) as a function of geomagnetic latitude θ , distance from equator and interaction time. Particle started at resonance, at the equator. Other interaction parameters shown on the graph

line) was chosen; in this case the net change in α_{eq} is large enough to lead to the precipitation of this particle. The choice of ϕ_0 is also critical, other values for this parameter may lead to larger negative changes of α_{eq} but also to positive changes. This is illustrated in Figure 5.5 which shows the possible final $\Delta\alpha_{eq}$ for a range of all possible initial phases ϕ_0 for the test particle used in Figure 5.4.

Here $\Delta\alpha_{eq}$ is calculated for ϕ_0 in steps of 1° . In this case only a limited range of ϕ_0 is scattered sufficiently to end up in the loss cone, and for the range of ϕ_0 near -160° the scattering leads to an increase in α_{eq} . An interesting effect occurs at $\phi = 166^\circ$ which gives the largest negative pitch angle change. The existence of such steep minima is the result of the general non-linear behaviour of the interaction. For low values of B_w the scattering is “linear” which is to say that the dominant factor which controls $\phi(t)$ is the background field inhomogeneity rather than the wave field: This leads to a sinusoidal shape of the $\Delta\alpha_{eq}$ v. ϕ_0 graph (eg. Figure 5.9[a]). As B_w is increased it becomes the dominant factor in

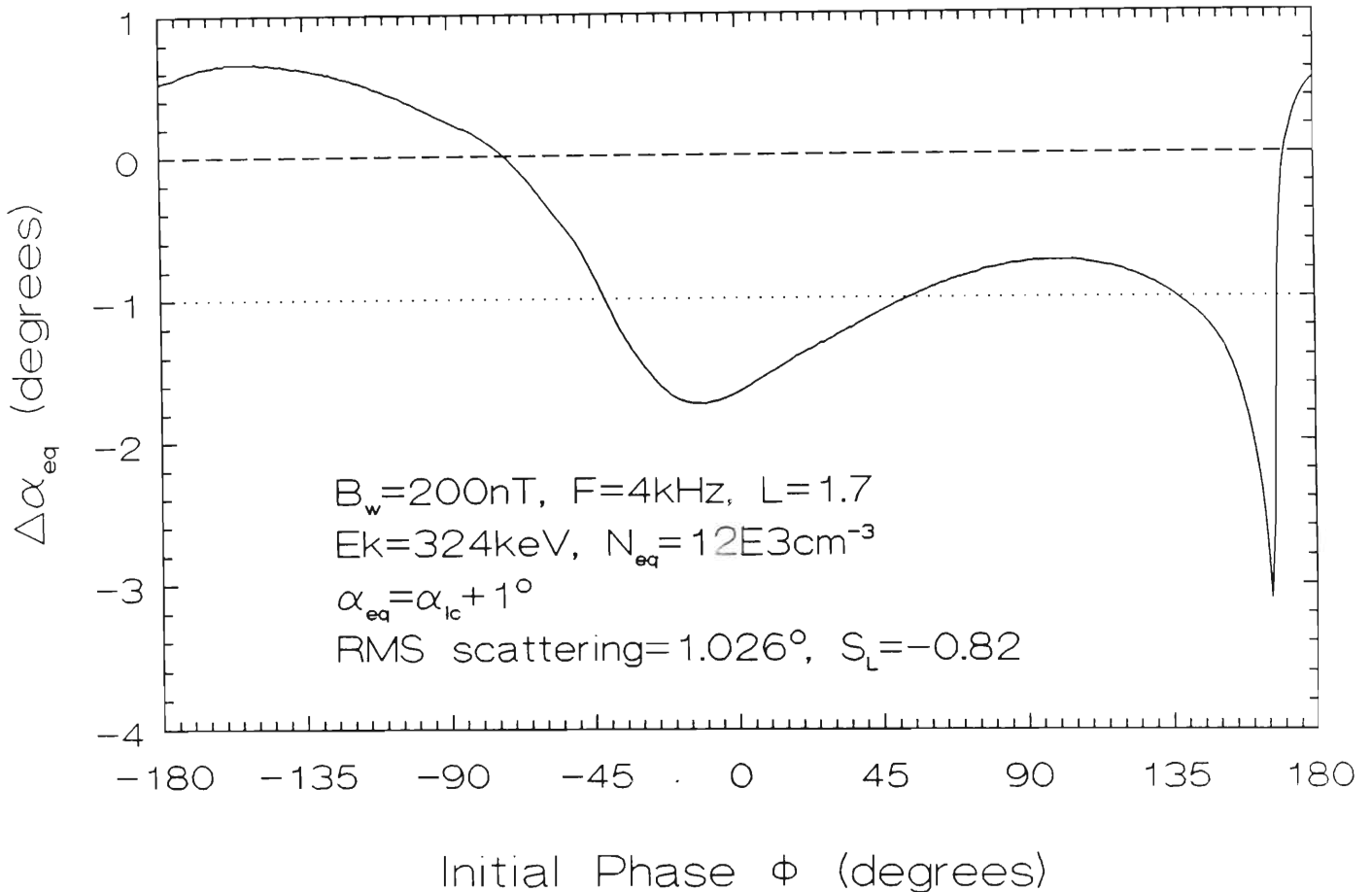


Figure 5.5: Final pitch angle scattering as a function of initial phase ϕ for the test particle of Figure 5.4. Interaction parameters shown on graph

controlling $\phi(t)$. “Trapping” here means that ϕ is forced to be stationary during the interaction, resulting in maximum pitch angle change. “Good” trapping can only occur for ϕ around 0° degrees (eg. Figure 5.9[f]). For intermediate cases the shape of the $\Delta\alpha_{eq}$ v. ϕ_0 graph is a mixture of the two cases: some scattering due to the “linear” background field controlled scattering and some due to the non-linear, B_w controlled scattering. The two effects superimpose to give the minima as observed in figure 5.5 and Figure 5.9[e]. The strange new behaviour observed in Figure 5.9[a] for very low n_{eq} is examined in section 5.4. For a detailed description of the trapping mode and its dependence on B_w and ϕ see [Inan, 1977].

To indicate the scattering efficiency the RMS scattering and S_L coefficient is calculated: In this case the RMS scattering is 1.026° and S_L is -0.82 .

5.4 Interaction Parameter Dependence on L -value

As indicated in section 5.1 the resonance interaction depends on many variables. The main concern of this paper is to show explicitly the variation in the scattering efficiency, as given by the RMS scattering and S_L coefficient, with L -value. The

simulation was thus run for a full distribution of particles in ϕ_0 for the L -value range 1.2 (top of ionosphere) to 2.0 in 0.1 L steps, which then matches up to previous studies [Inan et al., 1982, Chang and Inan, 1985], and for a range of B_w , ω_w and equatorial electron density profiles.

5.4.1 Calculations for Various B_w

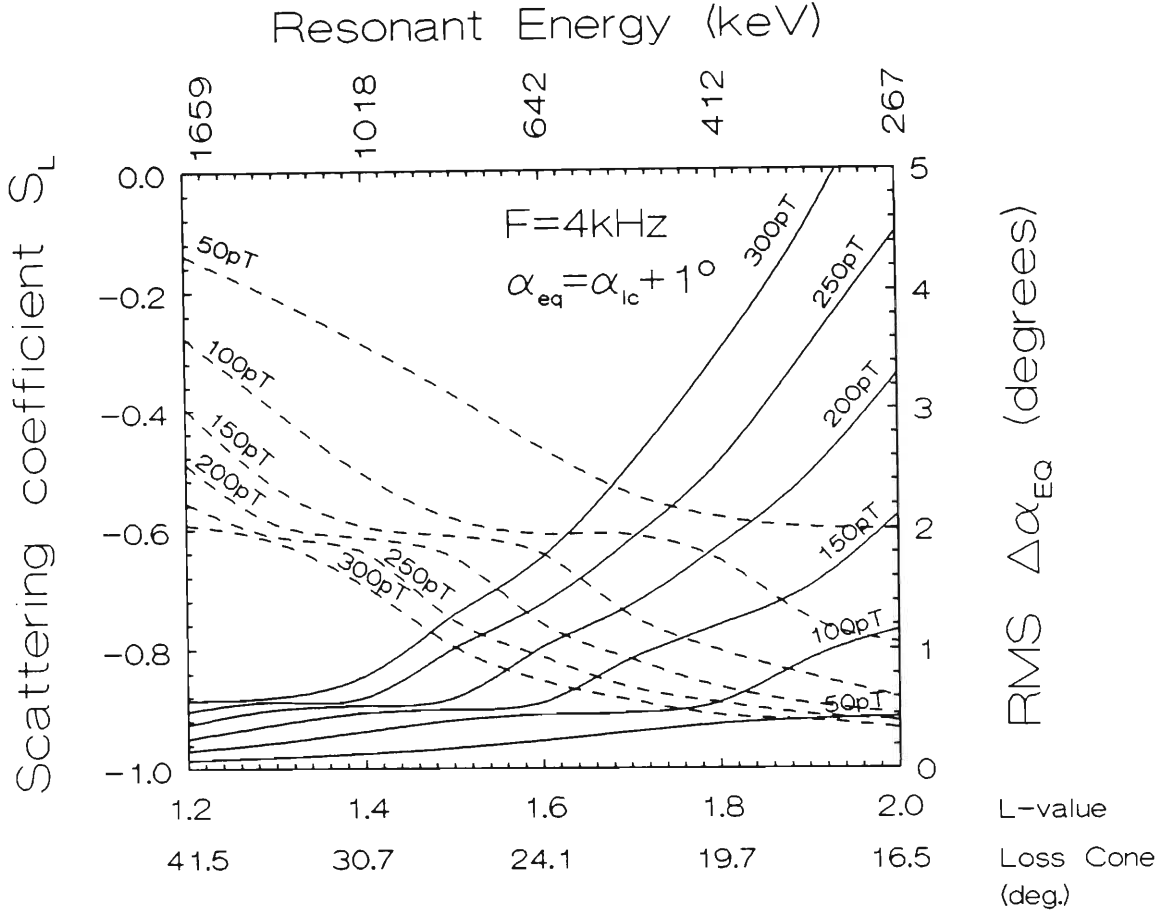


Figure 5.6: L -dependence of the RMS $\Delta\alpha_{eq}$ (full lines, right y-axis) and S_L (dotted lines, left y-axis) as a function of wave intensity B_w (50 to 300 pT in 50 pT steps). Also shown are the loss cone angle and resonant energies for the L -values chosen

Figure 5.6 shows the L dependence for various wave intensities B_w , using the standard equatorial electron density profile III of Figure 5.2, for a frequency of 4 kHz. For all wave intensities shown the RMS scattering increases with increasing L , and this increase becomes more pronounced for higher B_w . Note not only the increase in actual scattering as given by the RMS value but also that the proportion of particles scattered in the direction of the loss cone as given by S_L increases with both L and B_w . S_L mirrors the expected transition from the “linear” case with S_L closer to zero, to the trapped mode giving large negative S_L indicating predominant negative scattering. This behaviour can be understood in the following way: At low L the background field strength is larger than at

high L and thus larger B_w are needed to force the trapping mode, where large negative pitch angle changes can occur. This effect diminishes as one moves to higher L for a combination of reasons: The background field B_0 decreases, and resonant times increase due to a decrease in resonant energies and a decrease in background field curvature.

The important thing to note here is the relatively high value of B_w needed; for $B_w=50$ pT, a high value for whistler waves, the scattering efficiency lies below 0.5° for the whole L -range, and below $L=1.5$ even extremely intense whistler waves have a scattering efficiency insufficient to scatter particles into the loss cone (particles here are “started off” at $\alpha_{lc} + 1^\circ$). We have used a wave frequency of 4 kHz as this lies within the band of the most intensely transmitted whistler frequencies.

5.4.2 Calculations for Various ω_w

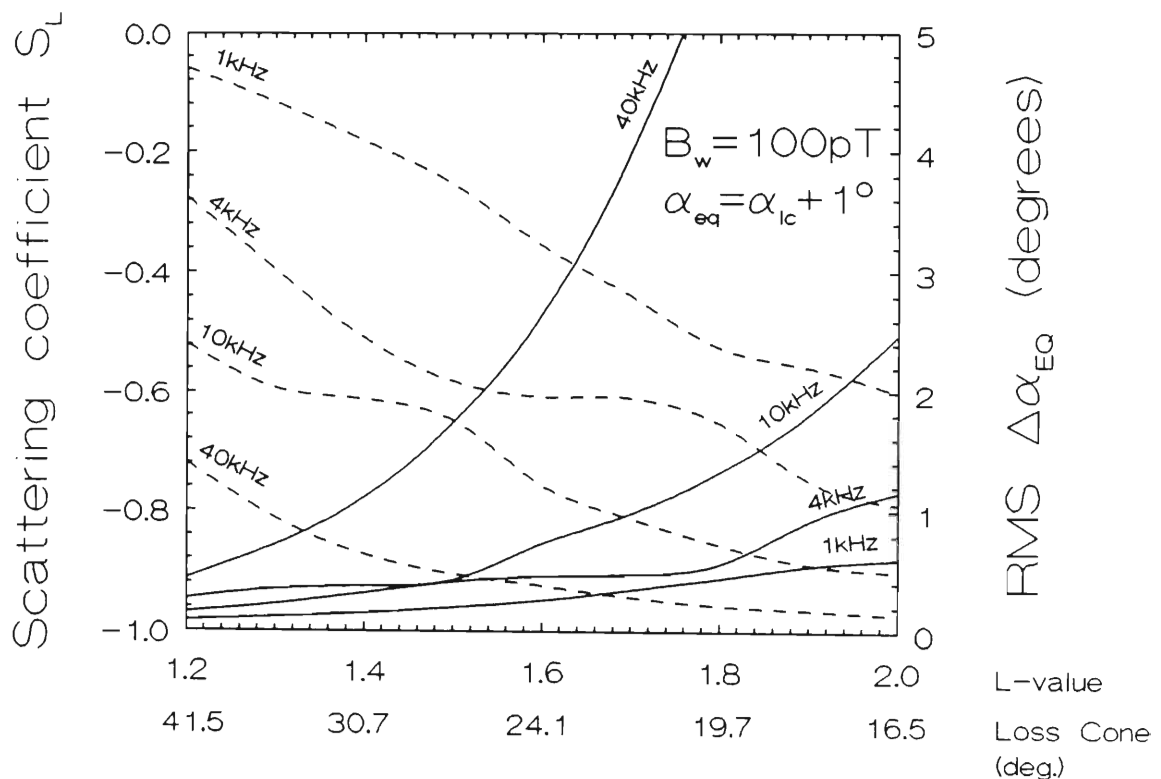


Figure 5.7: L -dependence of the RMS $\Delta\alpha_{eq}$ (full lines, right y-axis) and S_L (dotted lines, left y-axis) as a function of wave frequency ω_w (1, 4, 10 and 40 kHz)

The effect of choosing other frequencies is shown in Figure 5.7. This shows scattering as a function of L -value for various ω_w , using the standard equatorial electron density profile III of Figure 5.2, for a B_w of 100 pT. As the wave frequency is increased the scattering becomes more efficient: RMS scattering increases and S_L becomes more negative. Again this effect is more pronounced at higher L . Below $L=1.5$ even frequencies below 10 kHz (whistler range) do not scatter par-

ticles near the loss cone - one has to move to frequencies well outside this range for the scattering to become significant. This behaviour can be explained from Figure 5.3, which shows a decrease in resonant velocity and energy for higher frequencies, thus increasing the interaction time. The changes in B_0 , as explained above, further increase the scattering efficiency as L increases.

5.4.3 Calculations for Various n_{eq}

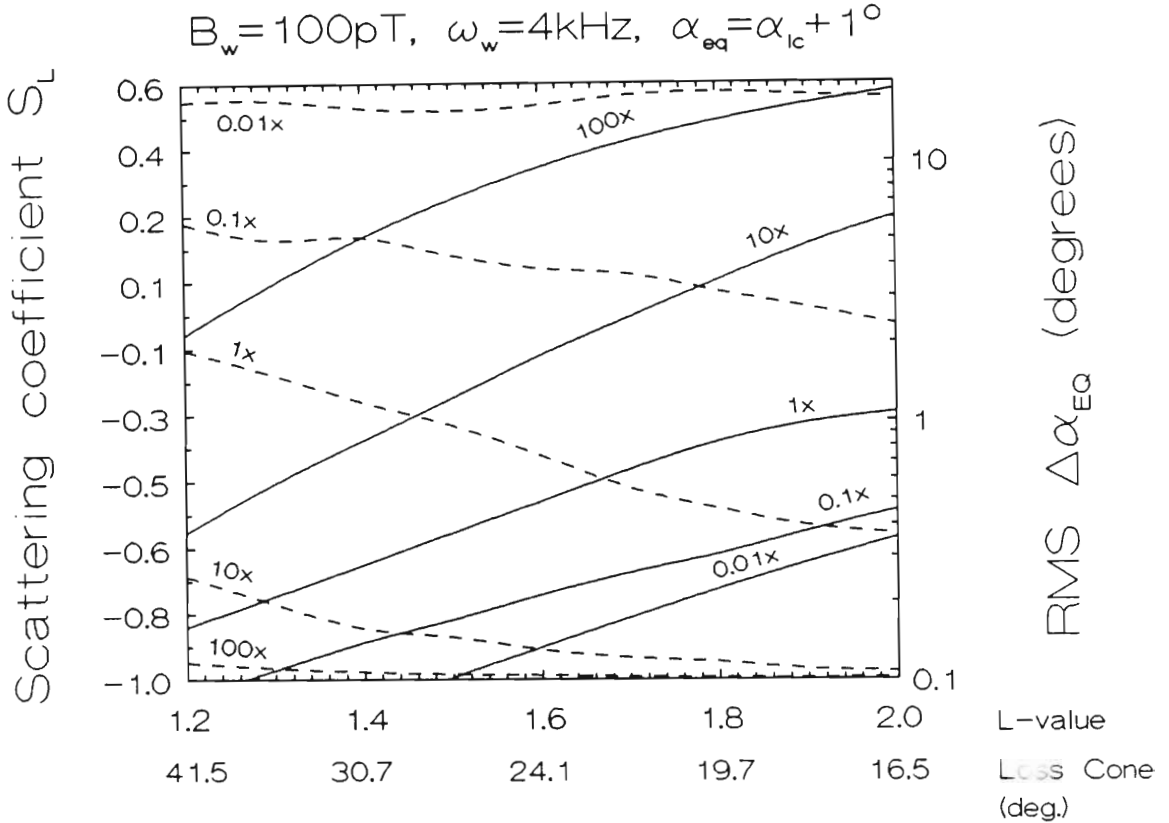


Figure 5.8: L -dependence of the RMS $\Delta\alpha_{eq}$ (full lines, right y-axis) and S_L (dotted lines, left y-axis) as a function of equatorial electron density n_{eq} . The multiplication factors on each graph represent the factors by which the “normal” profile III of Figure 5.2 is scaled

Figure 5.8 shows the effect of varying the equatorial electron density profile. The standard profile III of Figure 5.2 has simply been scaled up and down by two orders of magnitude, to give five different profiles (I to V, Figure 5.2). As L varies in Figure 5.8 the corresponding value of n_{eq} from Figure 5.2 is used in the calculations.

Reducing the electron density leads to an almost non-existent interaction, with very low RMS scattering while an increase of only one order of magnitude leads to a significant increase in the RMS scattering. This result can be understood in the following way: The wave number k is proportional to n_{eq} ($n_{eq} \propto n^{1/2}$), and as n_{eq} decreases the wave phase velocity increases ($v_p \propto n^{-1/2}$) and the parallel

resonant velocity becomes higher [$v_r = v_p(\frac{\omega H}{\omega} - 1)$], requiring higher particle energies. These particles move more quickly through the resonance region and thus have less time to be scattered. Increasing n_{eq} the effect is opposite and more pronounced, since a decrease of particle energy required not only increases the interaction time but also reduces the relativistic mass of the particles, making it “easier” for the wave field to exert force on the particle. Thus higher n_{eq} would also reduce the wave intensity required for successful trapping and efficient pitch angle change.

However, the behaviour of S_L at very low n_{eq} is unexpected: S_L is almost constant and positive, indicating predominantly positive pitch angle change. This indicates a third mode, since for the ideal “linear” case S_L is expected to be very near zero and for the trapped mode S_L is large and negative. This phenomenon is further investigated in Figure 5.9 where the full ϕ_0 dependence of the scattering has been plotted for a variety of equatorial electron density profiles and L -values.

5.4.4 “Positive Mode” at Low n_{eq} - a New Result

Figures 5.9[d]–[a] show the n_{eq} dependence in more detail, showing the transition from the “linear” case in Figure 5.9[d] to the new, predominantly positive scattering mode in Figure 5.9[a], which is called the positive mode. In this mode the behaviour remains “linear” for positive ϕ_0 , and is strongly non-linear for negative ϕ_0 with a positive peak near $\phi_0 = 40^\circ$. From a detailed study of individual particle trajectories this mode is explained as follows: At these low n_{eq} the wave phase velocity is very high, leading to higher resonant velocities - which are already high due to the relativistic electrons needed for resonance at low L . Since v_r cannot exceed c a high γ is needed to enable resonance. Typical values are $v_r \sim 0.98c$, $\gamma \sim 5$ and resonant energies in the range from 12 MeV at $L = 1.2$ to 3 MeV at $L = 2$. Interaction times are very short (~ 1 ms), and the interaction region is limited to $\sim 2^\circ$ within the equator. In this short time ϕ only undergoes one cycle before the interaction region is left which for ϕ_0 near -40° brings ϕ close to zero for a relatively long time, and at $\phi = 0$ the wave exerts maximum force on the particle. Under normal conditions $\Delta\alpha_{eq}$ oscillates about its final value (see Figure 5.4): Here $\Delta\alpha_{eq}$ swings positive and is “left” there as the particle moves out of resonance quickly.

This positive mode, however, is only of theoretical interest since the low background electron densities needed are rarely encountered in practice at low L .

The normal transition to a trapped mode in Figures 5.9[d]–[f] is also shown, and for large n_{eq} the interaction becomes almost ideal for negative pitch angle scattering as S_L approaches -1 (strong trapping).

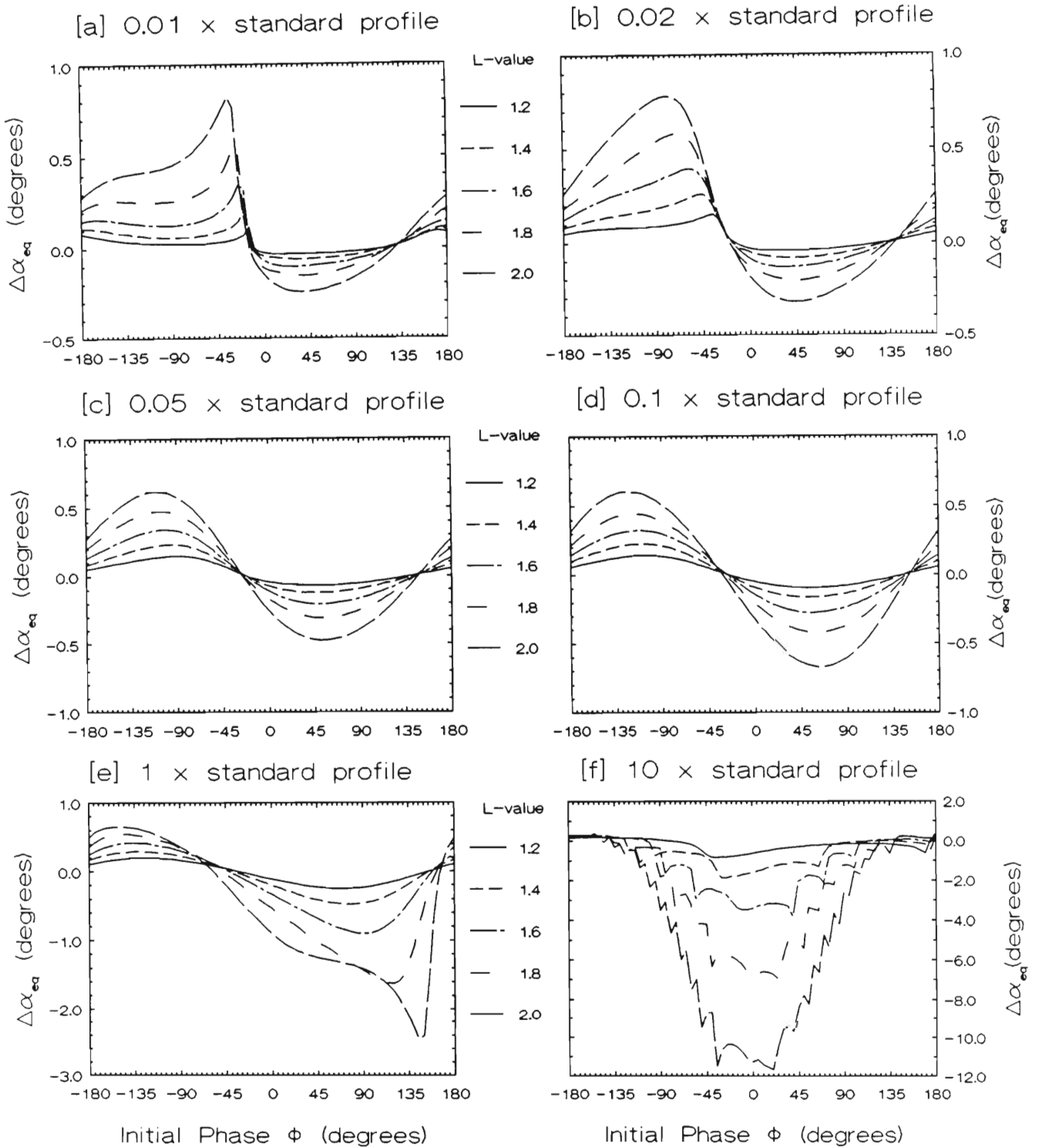


Figure 5.9: Final pitch angle scattering as a function of initial phase ϕ for the conditions in Figure 5.5. Each graph uses a different multiplication factor for the standard electron density model of Figure 5.2 (Profile III) and plots the curves for several L-values. [a] - positive mode, [d] - "linear" mode, [f] - trapped mode

5.5 Lightning as a Wave Source at Low L ?

Lightning has been shown to be the source of the whistler mode radiation responsible for the wave-particle interaction leading to a trimpi event, at least at high and middle L -values. Can this be true at the low ($L < 2$) L -values considered here? To achieve pitch angle scattering $> 1^\circ$ the requirements can be summarised briefly:

- (a) Wave intensities B_w in excess of 150 pT for low frequencies or
- (b) Wave frequencies ω_w higher than 10 kHz or
- (c) Background electron densities at least one order of magnitude higher than normal or
- (d) Larger interaction times.

The mode of propagation of the VLF waves for gyroresonance has to be field aligned: the ducted whistler mode. The work of [Hayakawa and Tanaka, 1978] (and references therein) shows that ducted propagation at low L is supported by simultaneous measurements of multistation networks and in-situ measurements of wave normal angles. It is highly probable that daytime whistlers travel in ducts lying in the equatorial anomaly, while propagation of nighttime whistlers depend significantly on latitude: down to 20° latitude the enhanced occurrence of echo trains suggests ducted propagation while at the lowest latitude range the most probable propagation seems to be non-ducted, although several near-field aligned modes which are field-aligned near the geomagnetic equator (and can thus participate in gyroresonance) can exist [Singh, 1976]. From [Smith, 1961] we know that the whistler mode propagates in a field-aligned background electron density enhancement (a duct) below a cutoff of one-half the local gyrofrequency. Thus for the range of L -values considered here frequencies in excess of 100 kHz can propagate in the whistler mode. Since lightning is a short electromagnetic burst it radiates at all frequencies, thus point 2 above could be potentially satisfied.

The available wave intensities from a lightning stroke are shown in Figure 5.10. This gives the peak spheric amplitude in a 1 kHz bandwidth 10 km from the source [Volland, 1982]. The scatter of data points roughly follows the empirical equation

$$E_{peak} = 6500f^{-1.1} \quad (\text{for } 10^{-1} < f < 10^4) \quad (5.18)$$

where f is in MHz. This wave energy is generated below the ionosphere: to reach a guiding duct above the ionosphere waves are in general attenuated by the ionosphere. Figure 5.11 shows the ionospheric penetration losses calculated by [Brooker et al., 1970], for the best case of 90° magnetic dip. Transmission losses are low for normal whistler frequencies but increase sharply above 10 kHz.

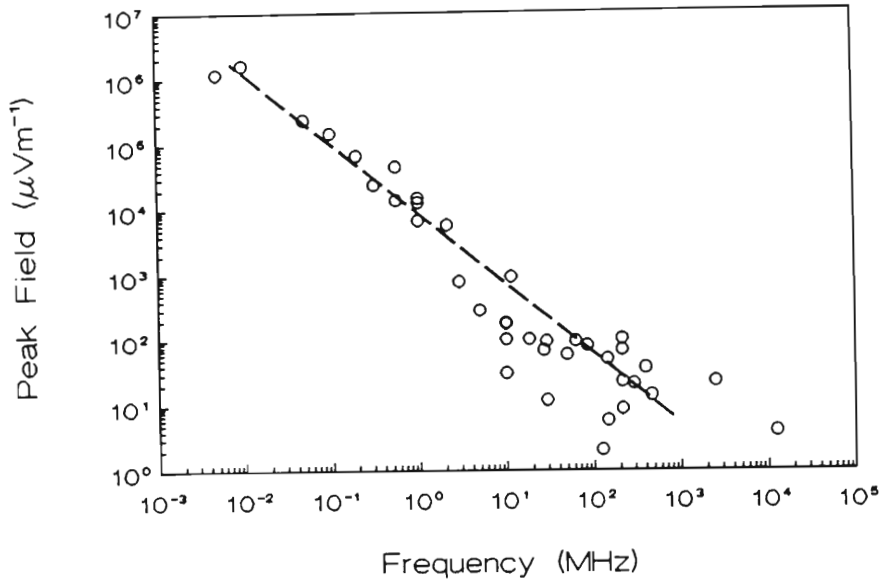


Figure 5.10: Peak sferic electric field amplitude as a function of frequency in a 1 kHz bandwidth 10 km from the source (H. Volland, 1982)

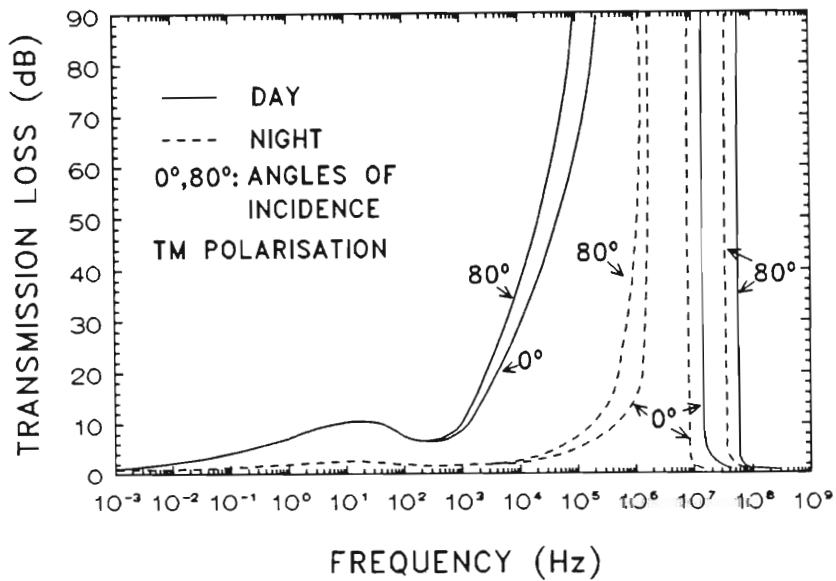


Figure 5.11: Ionospheric penetration losses as a function of frequency for 90° magnetic dip for both day and night at 0° and 80° incidence

In Figure 5.12 the two effects of source spectrum and transmission losses are combined and normalised with respect to 1 kHz, for both day and night conditions. This shows that higher frequency waves get progressively weaker with increasing frequency, with daytime conditions still worse.

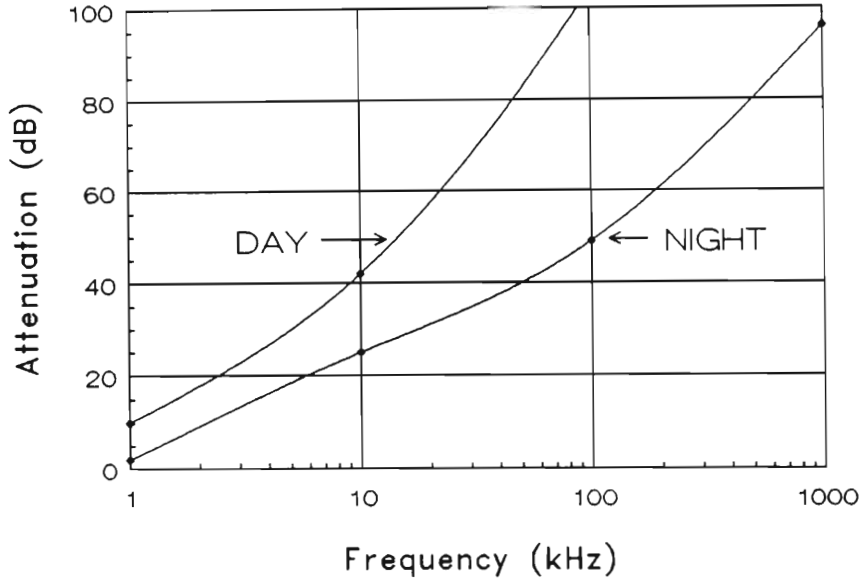


Figure 5.12: Combined source- and transmission spectrum at the top of the ionosphere as a function of frequency normalised to 1 kHz

From these relative calculations it is clear that waves at higher frequencies (outside the normal whistler range) play at best a minor role in wave-particle interaction since they are so heavily attenuated. This does not, however, answer the question if absolute wave intensities in the order of ~ 150 pT are available at the top of the ionosphere. There is little experimental data of wave intensities in a duct: even if one measures the available wave intensities at ionospheric heights, it is not known which fraction actually enters a duct and remains there until it reaches the resonance region near the equator. Most of the wave energy of whistlers measured at the ground is confined to the frequency range 500 Hz to 6 kHz, but ground observations are not a good measure of the field intensity in the magnetosphere, since that depends on many highly variable parameters which are in general not known:

- (a) The ionospheric exit points and thus the distance to the observing station [Ladwig and Hughes, 1989], [Friedel, 1987]
- (b) The earth/ionosphere waveguide attenuation [Tsuruda et al., 1982]
- (c) The ionospheric transmission/reflection coefficients [Helliwell, 1965]
- (d) The spreading losses in the magnetosphere depending on whether the wave propagation was ducted or non-ducted

Some crude estimates based on whistlers measured at Palmer Station ($L=2.3$, 65°S 64°W) show that intensities of up to 100 pT can be consistent with measurement [Inan et al., 1989] but are the exception rather than the rule. There is as yet no concrete evidence of whistler intensities in ducts available.

5.6 Discussion

There are a number of reasons why Trimpi events should not be observed at Durban:

- (a) The resonant velocity and the loss cone angle are large and the total energy of a resonant electron is correspondingly large. From Figure 5.3 we can see that at $L=1.7$ the resonant electrons have the following total energies

1 MeV	at	1 kHz
270 keV	at	5 kHz
160 keV	at	10 kHz

These increase markedly as we move to $L=1.5$ viz.

1.8 MeV	at	1 kHz
500 keV	at	5 kHz
260 keV	at	10 kHz

Because the population density of energetic electrons decreases markedly for high energies the number of resonant electrons at low L -values is likely to be small. The number of high energy electrons on longitudes close to Durban is likely to be further reduced by

- (b) The fact that electrons have drifted through the South Atlantic Geomagnetic Anomaly and those with pitch angles close to the loss cone will have been lost. This means that
- (c) Most of the flux of precipitating particles comes from the edge of the loss cone, since there even small changes in pitch angle can scatter significant numbers of particles into the loss cone. At Durban the loss cone has been depleted after particles have drifted over the South Atlantic Geomagnetic Anomaly, where mirror heights are lowered. Thus we need large pitch angle changes at Durban to scatter electrons into the loss cone
- (d) Our simulation shows that very large wave fields are needed for pitch angle scattering of $\sim 1^\circ$, which is in agreement with the study of an WIEP event done by [Inan et al., 1989] at $L=2.24$. In general the conditions for gyroresonance become more and more unfavourable at lower L and this, coupled with the lightning source characteristics (higher frequencies heavily attenuated, doubt concerning the availability of large wave amplitudes) make trimpi events more unlikely.

In consideration of these facts it is perhaps remarkable that trimpi events are observed at Durban at all but, in fact, on rare occasions well defined events are recorded. It is of interest that observations include a number of daytime trimpis.

This may not be surprising considering the high energy of the resonant electrons. The rarity of daytime trimpis at higher L values may be due to the fact that the lower energy resonant (and precipitating) electrons may not produce ionisation below the level of the daytime ionosphere (see section 6.4.4).

A possible explanation for the low frequency of occurrence of trimpis at Durban is as follows: Because the resonant electron energy increases and the scattering efficiency decreases so markedly as one moves to lower L values (figure 5.6) from Durban, the probability of getting trimpis precipitation falls off rapidly with decreasing latitude so that only the region close to the station has a reasonable probability of getting precipitation. By contrast at higher latitudes precipitation as far as 1500km or more [Leyser et al., 1984] on the low latitude side of the station may give rise to a trimpis event with the consequence that trimpis are much more frequent.

Since the event signatures observed at Durban remain typical of trimpis events observed elsewhere it is difficult to think of another naturally occurring phenomena apart from lightning which has a similarly short onset time and wide frequency range.

There are several suggestions for alternate scenarios which would lead to more effective gyroresonance:

- (a) It is possible that unducted whistler waves play a much larger role in particle scattering [Inan et al., 1989]; [Friedel and Hughes, 1990]. Only a fraction of whistler energy is ducted, and much larger unducted intensities can be available. It is also possible that some unducted ray paths satisfy the resonance condition for longer periods than their ducted counterparts, thus producing larger pitch angle scattering. The resonance condition depends on the particle parallel velocity, which only changes quickly near the mirror points, and the electron gyrofrequency, which depends on the background field strength. This would be especially “helpful” at low L where large background field curvatures lead to critically short interaction times. It is also possible that unducted rays experience larger focusing in the magnetosphere, leading to higher intensities
- (b) Changes in the background field morphology due to resonant cavity modes and other pulsations could significantly “flatten” the field lines and thus enhance the resonance condition over time scales much longer than the typical trimpis event. This possibility is examined in detail in chapter 7
- (c) Our calculations (as all previous simulations) have dealt with a fixed wave frequency which give relatively short interaction times with an individual electron. As a particle of a given energy travels along a field line it will be in resonance with different frequency waves all along its path, and in effective resonance with a given fixed frequency only for a short section along its path. Whistlers are signals which exhibit dispersion. It is therefore possible for a given particle to remain in resonance with different frequencies of the

same whistler as the two counter-stream for a limited time. Furthermore, as the particle interacts its pitch angle and therefore its v_{\parallel} and/or v_{\perp} are changed, and it becomes resonant with a different frequency wave. If these two effects combine to effectively track a whistler then large pitch angle changes become possible: in fact, at low L only those particles able to do this might experience significant scattering. This is examined in section 7.5

- (d) Only first order resonance has been considered here. More recent work by [Inan et al., 1991] has shown that at large pitch angles (low L) Landau resonance becomes significant and could be important at low L

The database for low-latitude trimpi events is still small and further data is needed. A further project to this end is currently being undertaken at Durban. First results from this project are presented in chapter 6.

Chapter 6

First Observations of Trimpi Events at Durban using an OMSKI Receiver

OMSKI stands for OMEGA and MSK Instrument, where OMEGA and MSK refer to two types of VLF transmission formats (see section 6.1). This equipment is a dedicated computer controlled VLF receiver for trimpi work, designed and produced by the University of Otago in Dunedin, New Zealand. The S.P.R.I. has purchased two units of this type, the first of which (OMSKI1) has been operating at the Institute since April 1991 and the second (OMSKI2) since December 1991. These units were purchased as part of joint project between Prof. Dick Dowden of Otago University, Dr. Andy Smith of the British Antarctic Survey (BAS) in Cambridge, United Kingdom, Dr. Arthur Hughes and the author, both of the S.P.R.I., Durban. The aim of this project is the joint monitoring of multiple signal paths for joint trimpi analysis, using the units in Durban (and later at SANAE, Antarctica, and possibly Marion and Gough Islands, see section 8.3.1) and the existing BAS-net of identical receivers at Halley and Faraday stations in Antarctica [Smith and Cotton, 1990] as shown in Figure 8.1. First reports of data from the BAS-net were presented at the URSI conference in Prague in September 1990 [Smith et al., 1990] and a report on a full 12 month operation of BAS-net was presented at the IUGG conference in Vienna in August 1991 [Smith et al., 1991b]. The extension of this project to include worldwide trimpi-nets is discussed in section 8.3. The first results of one month's continuous OMSKI1 operation at Durban ($031^{\circ}00'E$, $29^{\circ}53'S$, $L=1.69$, $LT-UT = 2$ hours 4 minutes) are presented in this chapter.

6.1 The OMSKI System at the S.P.R.I

This type of receiver uses its own computer to decode the transmission formats of both OMEGA and MSK transmissions.

Station Designation	Location	Longitude	Latitude	Unique F (kHz)
A	Aldra, Norway	013°09'E	66°25'N	12.1
B	Monrovia, Liberia	010°40'W	06°18'N	12.0
C	Haiku, Hawaii	157°49'W	21°24'N	11.8
D	La Moure, USA	098°20'W	46°21'N	13.1
E	LaReunion	055°17'E	20°58'S	12.3
F	Trelev, Argentina	065°11'W	43°03'N	12.9
G	Woodside, Australia	146°56'E	38°29'N	13.0
H	Tsushima, Japan	129°27'E	34°36'N	12.8

Table 6.1: OMEGA transmitting stations

The OMEGA signals are part of the world-wide OMEGA navigation system, which uses high stability CW frequency signals in the 10–14 kHz band from eight transmitters around the world. Each station radiates omni-directional, time-multiplexed transmissions of 10.2, 11.05, 11.33, 13.6 kHz and one additional frequency unique to each station. Table 6.1 shows the frequency allocation to each station, and the transmission format is shown in figure 6.1 (from [Garrison, 1986]).

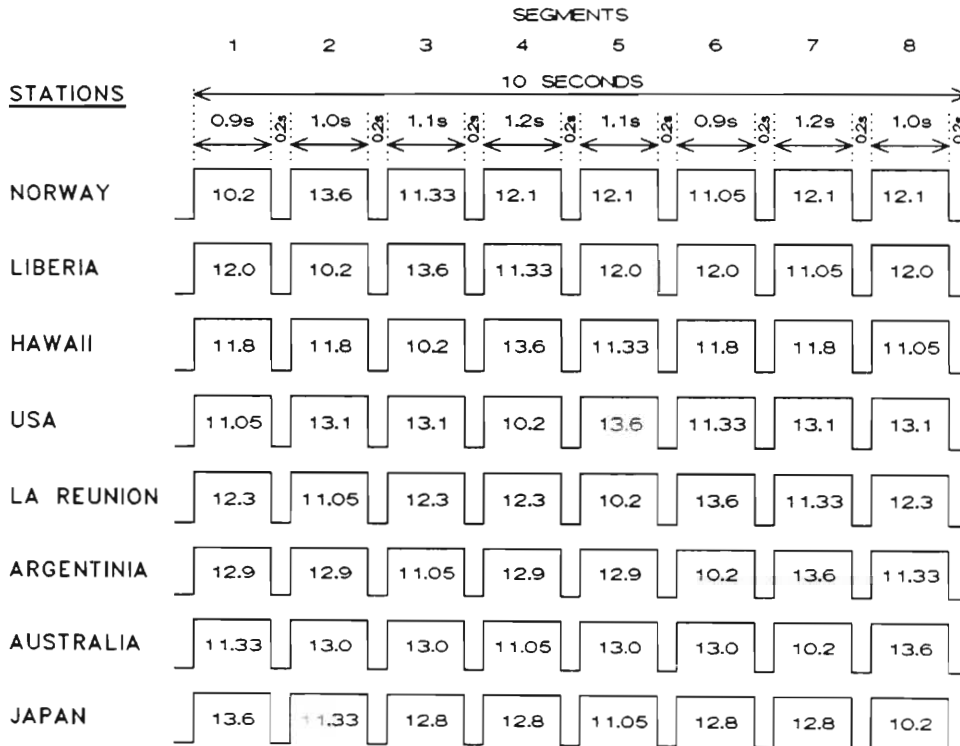


Figure 6.1: OMEGA signal transmission format

The OMSKI recognises and follows the OMEGA signal format with built-in software and derives accurate timing from the OMEGA signal format. In each frequency segment (see figure 6.1) the OMSKI measures the amplitude and phase of the signal.

MSK transmissions are modulated using Minimum Shift Keying. This modulation system is used by the major VLF communications transmitters because of its bandwidth efficiency and error performance. Unlike conventional FSK (Frequency Shift Keying) MSK lacks a power spectrum with discrete lines, and is generated by not only switching the transmitter between two signal frequencies, but also transmitting each frequency at two opposite phases. The OMSKI demodulates MSK using in-built custom software routines. The unit demodulates both the low (L) and high (H) frequency signals of the MSK format, and measures both amplitude and phase of these signals.

The OMSKI is controlled by an external IBM compatible PC which also provides data storage on either floppy or hard disk. Several modes of data collection can be selected, from high detail to minute-averaged. The control software allows one to pre-select when and which mode is activated for how long, allowing completely automatic operation limited only by the size of the mass data storage medium used. A graphic display of the last minute's data is provided for monitoring purposes.

The measurement of MSK signals is described in detail by [Adams, 1990] while the OMSKI and its software is described in its accompanying manual [Friedel, 1991].

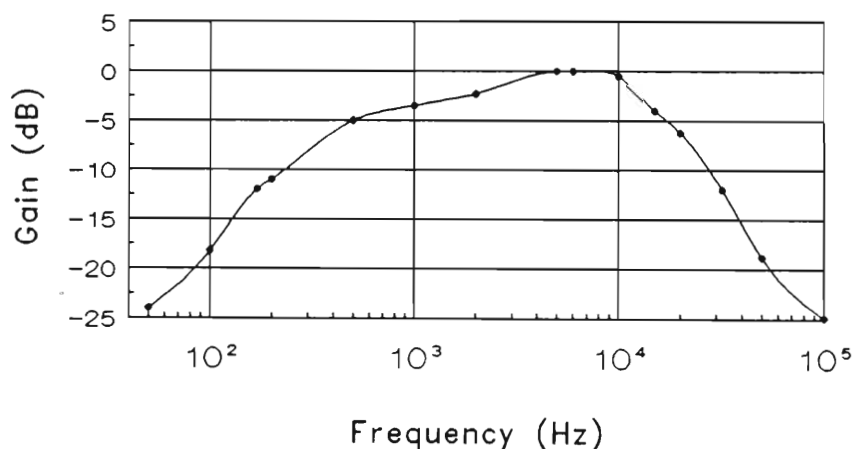


Figure 6.2: Frequency response of the OMSKI VLF pre-amplifier

The OMSKI system as set up at the S.P.R.I. is shown in Figure 6.3. A simple whip antenna is used together with a pre-amplifier which provides high gain in the OMEGA (10–14 kHz) and MSK (20–25 kHz) frequency range while isolating against power line harmonics and MW transmitters. The frequency response of the pre-amplifier is plotted in Figure 6.2.

The antenna signal is fed to the OMSKI via a 70m shielded cable. A further input required is a high stability 5 MHz frequency standard used as a reference for phase measurements. The standard used here is stable to better than 10^{-11} and has a long term drift of $\sim 10^{\circ}$ per hour measured against the average phase of the strongest signal received at Durban, Ω -LaReunion.

An XT-PC is used as a controller and a 21 MByte hard-disk as the storage

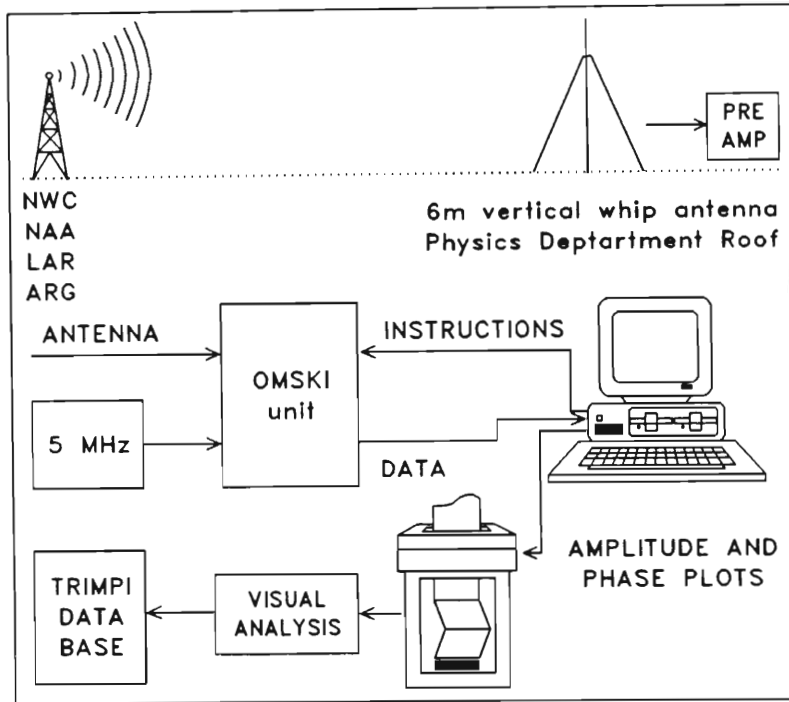


Figure 6.3: Implementation of the OMSKI system at the S.P.R.I. in Durban

medium, allowing many days of automatic operation.

For analysis the data is printed out using a standard dot-matrix printer and then visually scanned for trimpi events and other signal abnormalities. In the absence of broadband VLF data the causative sferic or whistler can not be found, so trimpi events are here identified by their characteristic signature (see section 1.1).

6.2 VLF Signal Paths to Durban

Table 6.2 shows the VLF signals that can be received by the OMSKIs as seen from Durban. Each OMSKI can receive two OMEGA and two MSK signals, the former being “factory preset” and the latter being selectable by dip-switches. OMSKI1 is set to Ω -LaReunion (LAR) and Ω -Argentina (ARG), NAA and NWC. OMSKI2 is set to Ω -LaReunion and Ω -Liberia (LIB), NWC and NSS. The results presented here are from OMSKI1 only. Figure 6.4 shows the great circle paths of all OMEGA and MSK stations to Durban, using an azimuthal equidistant projection centered on Durban. Paths are straight lines under this projection, and distances and bearings from Durban can be read off directly (see Table 6.2).

F (kHz)	CALL	STATION	LONG	LAT	BEARING	RANGE (km)
22.3	NWC	N-W Cape	114°09'W	21°48'S	106.0°E	13007
22.3	NLK	Jim Creek	121°55'W	48°12'N	041.0°W	17080
21.4	NSS	Washington DC	076°27'W	38°59'N	060.0°W	13567
24.0	NAA	Cutler MF	067°17'W	44°39'N	051.5°W	13007
23.4	NPM	Honolulu	158°09'W	21°25'N	135.0°E	18856
24.0	NAU	Aguada	067°11'W	18°23'N	077.5°W	11873
17.4	NDT	Yokosukaishi	137°01'E	34°58'N	064.0°E	13316
Ω	LAR	LaReunion	055°17'E	20°58'S	073.5°E	02646
Ω	ARG	Trelev	065°11'W	43°03'S	131.0°W	08322
Ω	LIB	Monrovia	010°40'W	06°18'N	054.5°W	06042

Table 6.2: OMEGA and MSK stations as seen at Durban

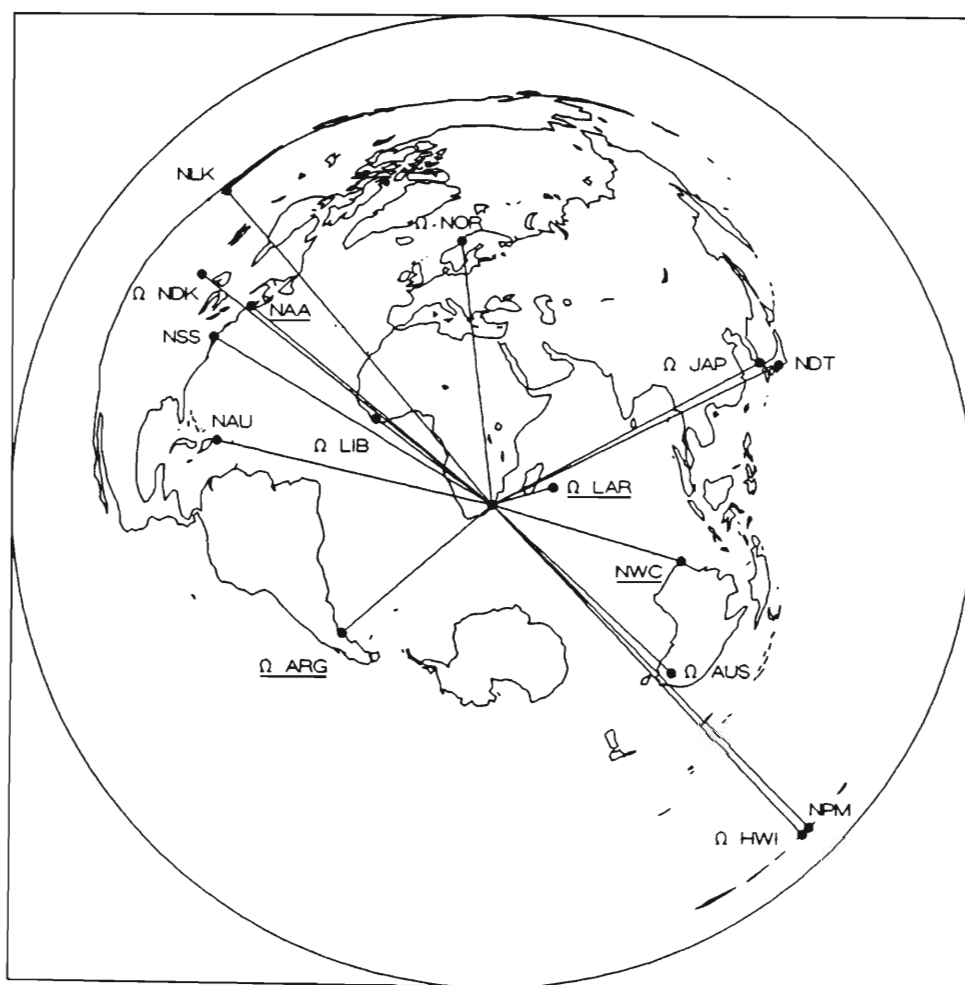


Figure 6.4: Great circle paths of OMEGA (Table 6.1) and MSK (Table 6.2) stations to Durban on an azimuthal equidistant projection centered on Durban. Stations underlined are used in this study

6.3 Data Collection

For the purposes of a first study the OMSKI1 was operated continuously from 27 June–27 July 1991. The logging mode used here was the HS-mode, recording OMEGA (all frequencies) and MSK (mean H+L MSK frequency only) in segment resolution (OMEGA segments: 8 segments \sim 1s long every 10s. Data is averaged yielding 8 data points every 10 seconds – see Figure 6.1). This mode was chosen since it is the most condensed form and data volume is kept down for 24 hr operation. This results in data files of 576840 kBytes per day and over 100 pages of graphic data printout per day.

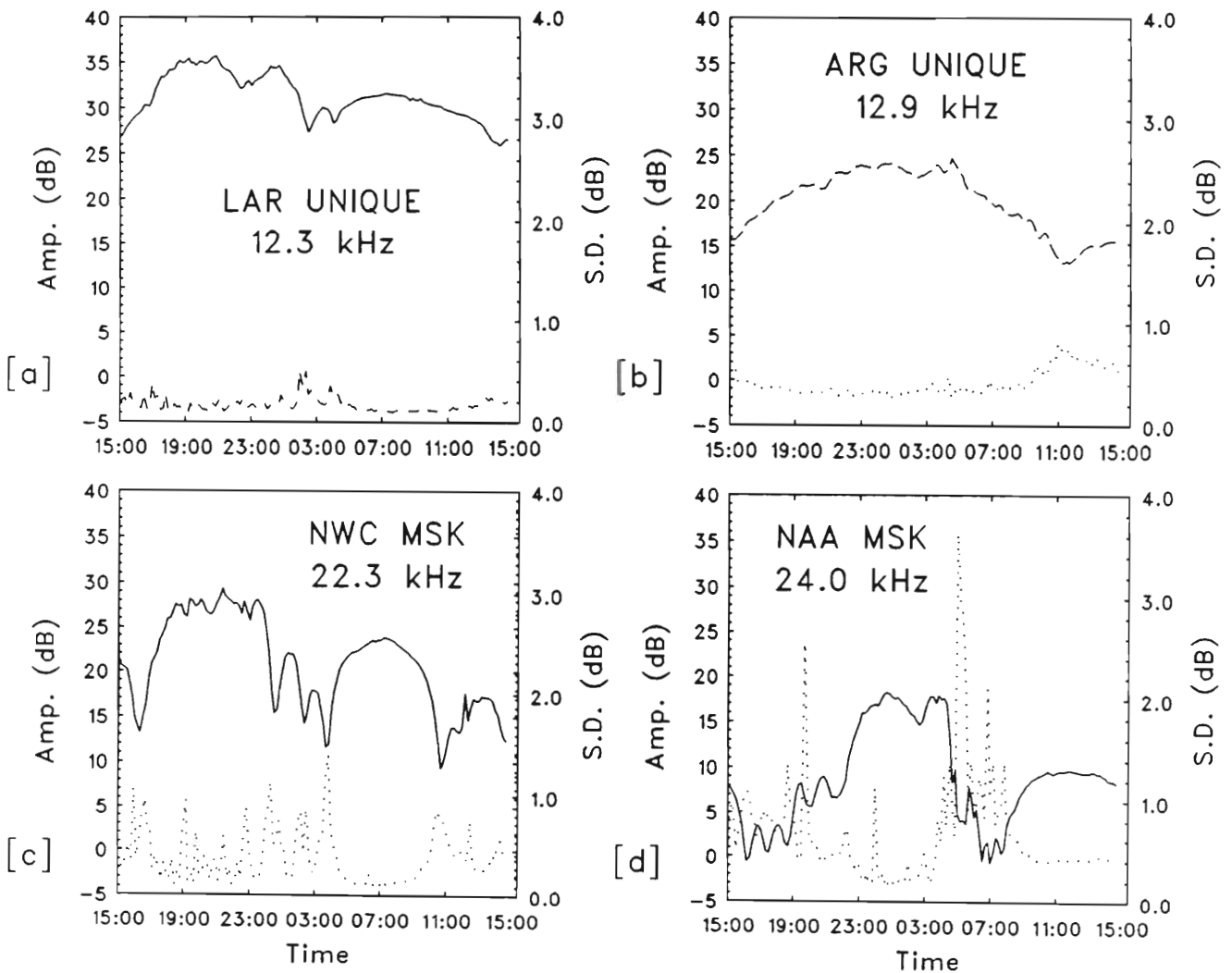


Figure 6.5: Signal amplitude (left axis, solid line) and standard deviation (right axis, dashed line) averaged over ten minute bins plotted against universal time for a 24 hour period

Continuous operation was chosen here not only to look for daytime trimpi events as reported in chapter 3 (and in section 6.4.4 here) but also to monitor the diurnal variation in signal strength and standard deviation as a measure of signal noise.

Many trimpi events are small, with amplitude variations of ~ 1 dB and phase variation of $\sim 5^\circ$. In practice signal amplitude is noisier than the phase, enabling phase trimpi detection even when the amplitude is already quite noisy. In Figure 6.5 the diurnal variation of signal strength and standard deviation is shown for the four signals monitored.

LAR is the strongest signal at Durban at all times with good S/N ratio (~ 0.2 dB average, better than 0.05 dB over long periods). ARG is weaker with a uniform noise level of ~ 0.5 dB at most times. NWC is the second strongest signal at Durban but shows strong day/night terminator effects. S/N ratio is better than 0.2 dB over long periods. NAA is the weakest signal, with good and stable S/N from 23h00–04h00 UT only. In general, signals are strongest when the whole path is in darkness, very disturbed during sunrise/set at either receiver or transmitter, and again stable, although not as strong, once the whole path is in daylight. This is well illustrated by NWC, being very strong from 18h00–0h00 and then again very stable from 04h00–09h00 even though at a lower amplitude.

From Figure 6.5 it is clear that there are times when the signal is too noisy to detect average trimpi events, and any results showing diurnal variation of trimpi activity must bear this in mind.

6.4 The 27 June – 27 July 1991 Data Set

Data for this period was recorded in the HS mode 24 hours a day. A total of 313 events were found in this period, of which a major proportion (88 events) were found during one active two hour period on the NAA signal (section 6.4.3). For the purpose of this study events are classified into three types (table 6.3):

Type	Description
Classic	Traditional Trimpi Perturbation
Dome	A New Event: Dome Shaped Perturbation
Other	Unknown Events (Possibly Transmitter Caused)

Table 6.3: Classification of events for the 27 June – 27 July data set

The statistics of these events for each signal received at Durban (NAA, NWC, ARG, LAR) are shown in Figure 6.6. The percentages shown are the percentage of total events, and the numbers the actual event count. Detection of events is limited by the noise on the signals (see section 6.3).

The total of 313 events detected in this data set has been subdivided according to event type and signal on which it occurred. Classic trimpi events predominate, with NAA being the most active mainly due to one single active period on 13.07.91 (see section 6.4.3). The activity on Ω -signals is very low, which is surprising considering the good signal strength of LAR which should enable the detection of small events as well. However the LAR–Durban path is also the path at lowest geomagnetic latitudes ($1.36 < L < 1.69$), and gyroresonance at low L

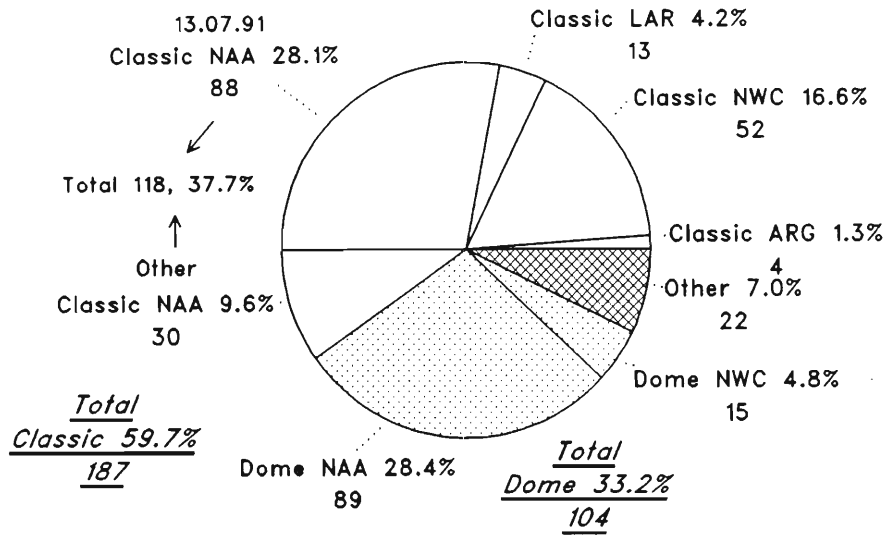


Figure 6.6: Statistics of various event types. All percentages shown are percentage out of total events. The unshaded area refers to classic events, the dotted area to dome events and the hatched area to other events. Each area is further subdivided according to station.

is less favoured (see chapter 5. Dome events make up a third of all events, so there is some confidence in this event being significant and not a spurious equipment or transmitter induced effect. Dome events are only observed on the higher frequency signals from NAA and NWC which are roughly twice that of the OMEGA frequencies. These events are further examined in section 6.4.2.

6.4.1 Classic Event Amplitude/Phase Plots

The standard way of presenting OMSKI data is by the use of amplitude/phase plots to show the distribution of trimp events particular to a specific path. Since each event can be any combination of amplitude and phase variation events are referred to as eg. positive/negative meaning positive amplitude, negative phase perturbation event. Each path has a unique event signature (A/P signature), however, a significant number of events have to be detected to build up a meaningful plot. Figure 6.7 shows such plots for the four paths considered here.

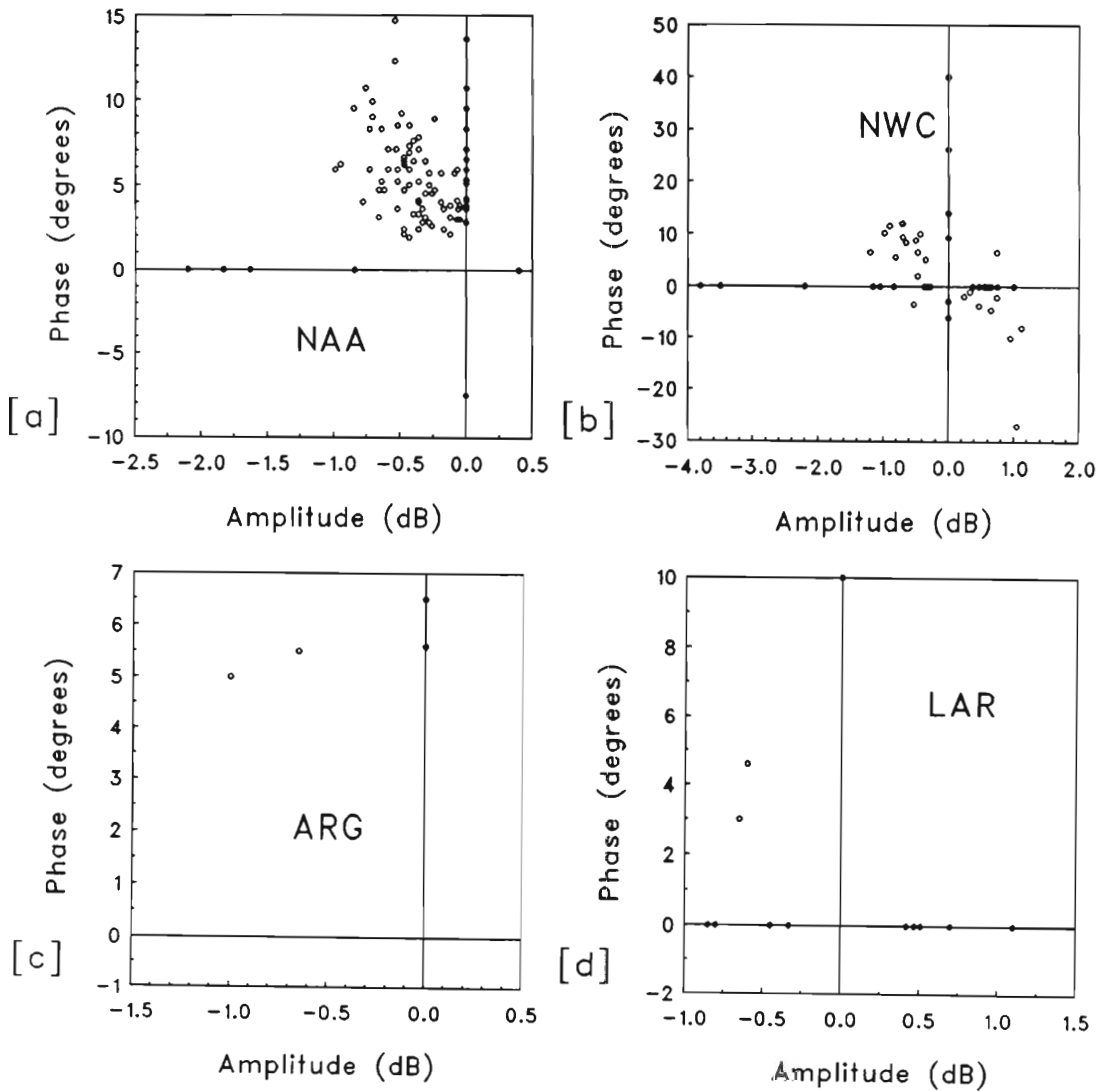


Figure 6.7: Amplitude/phase plots for classic events observed on NAA, NWC, ARG and LAR

Points in Figure 6.7 which have been assigned zero amplitude or phase perturbations refer to those events which had a clear signature in phase/amplitude but had no identifiable corresponding amplitude/phase signature.

Most events on NAA are in the second quadrant (negative amplitude, positive

phase). Events on NWC are split evenly between the 2nd (negative/positive) and the fourth (positive/negative) quadrant. Only 4 events are observed on ARG, which are too few for valid statistics. LAR shows mainly amplitude events, also very few. Since these plots are based on only one month's data, they have to be treated as preliminary results.

6.4.2 Dome Events - a New Type of Trimp?

The dome-shaped events reported here represent a new type of disturbance detected on VLF signals. A large proportion of dome events are detected here (33.2% of all events), which make them statistically significant. An example of such an event is shown in Figure 6.8.

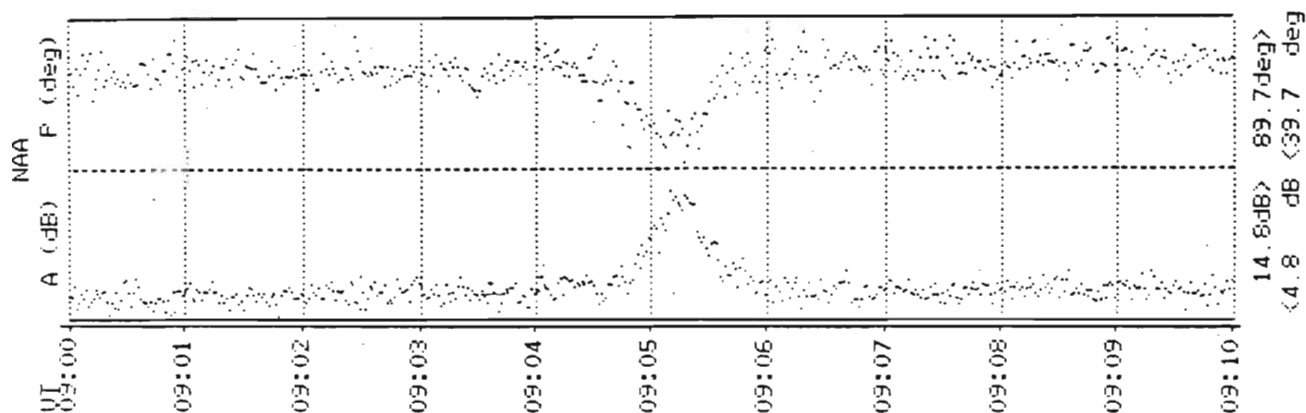


Figure 6.8: Dome-shaped event observed on NAA-Durban path at 09:04:45 UT on 01 July 1991 (+6.5 dB, -27° , duration 80s)

These events are characterised by a smooth dome-shaped symmetrical event onset and recovery in amplitude, accompanied by a mostly noisy dome shaped phase perturbation. Event amplitudes are near 5 dB with phase perturbations in the region of 20° – 30° , and event durations typically 80-150s. Events occur often on NAA and NWC within 10 seconds. Events of this type have only been found on the MSK signals, which is possibly not significant considering the overall low number of events observed on the Ω signals (see Figure 6.6). Figure 6.9 shows the A/P plots for these dome events.

Most dome events have a positive perturbation in amplitude accompanied by either positive or negative phase perturbation. The large number of events with no phase perturbation are possibly due to the noisy nature of the phase event, making it difficult to detect. Both signs of phase perturbation occur on NAA, while for NWC the events are mainly amplitude only.

Events of this nature have not been reported before, nor have they been associated

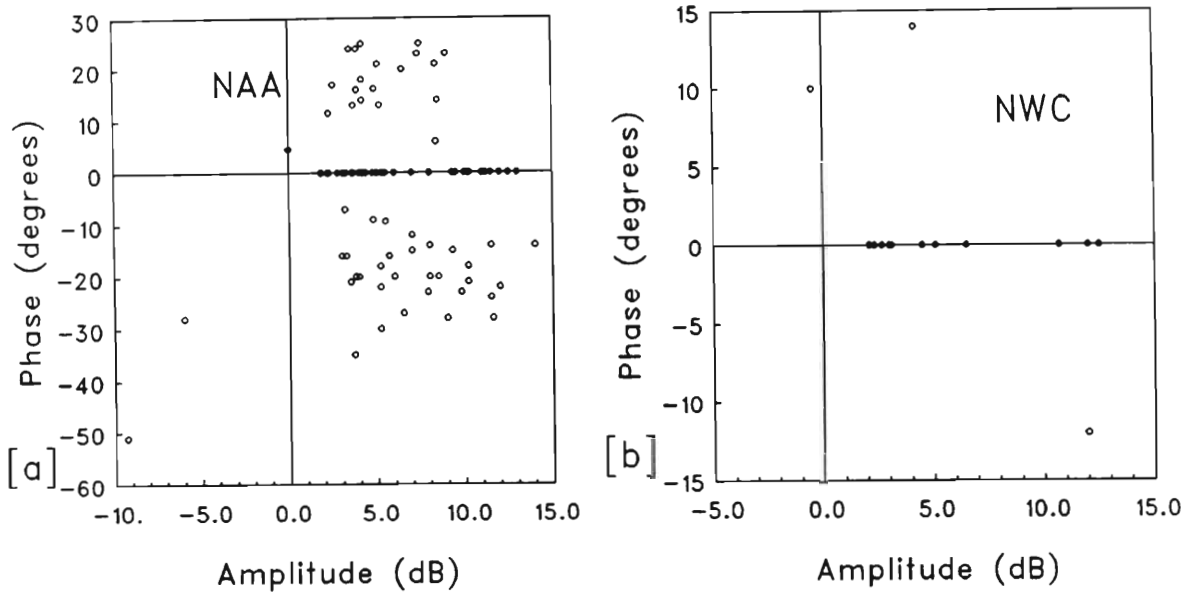


Figure 6.9: Amplitude/phase plots for dome events observed on NAA and NWC

with trimpi events. Evidence that they might be trimpi-related comes from a paper given at the IUGG conference in Vienna in August 1991 [Dowden et al., 1991]. This paper reported on the first results using a chain of VLF receivers along New Zealand, monitoring the signal from NWC (see section 8.3.2 for a map of the NZnet). Receivers spaced along an array can be used in “imaging” the wave induced enhanced ionisation patch from the amplitude/phase signatures of a single event at all the stations. Some perturbations which were clearly of the correct trimpi shape at one receiver had a quite different signature at a receiver only a few 100km away, including the dome-shaped signature reported here. It is thus possible that event signatures quite unlike the classical trimpi shape can be associated with the trimpi phenomenon. One possible explanation is that since at low L (for NWC – NZ paths $L \sim 2$) the wave-particle interaction is with high energy electrons, and the precipitating flux consists of high energy electrons, resulting in an intense and highly localised patch which initially has a VLF interaction crosssection too small to affect the signal. Once the patch diffuses out and starts decaying it will get larger and can thus effect the VLF signal, before decaying away completely. Even though diffusion of a plasma is predominantly along magnetic field lines, at low altitudes (D-layer heights) the neutral atmosphere is dense enough to enable diffusion across field lines by collisions. Field aligned diffusion only starts to become significant at heights above 300 km [Hargreaves, 1979]. This would explain the smooth rise in event onset for the dome events. Again, the present data set is too small to allow any conclusive comments on this new type of event.

6.4.3 High Activity Data Subset on NAA

Overall activity during the month of investigation is quite low, with an average event rate of about 7 events per day (all signals). There was, however, one period of very high activity observed on NAA, from 02:50–04:50 UT on 13 July 1991. 88 classic trimpi events were identified during this period. Figure 6.10 shows a 30 minute section of this set.

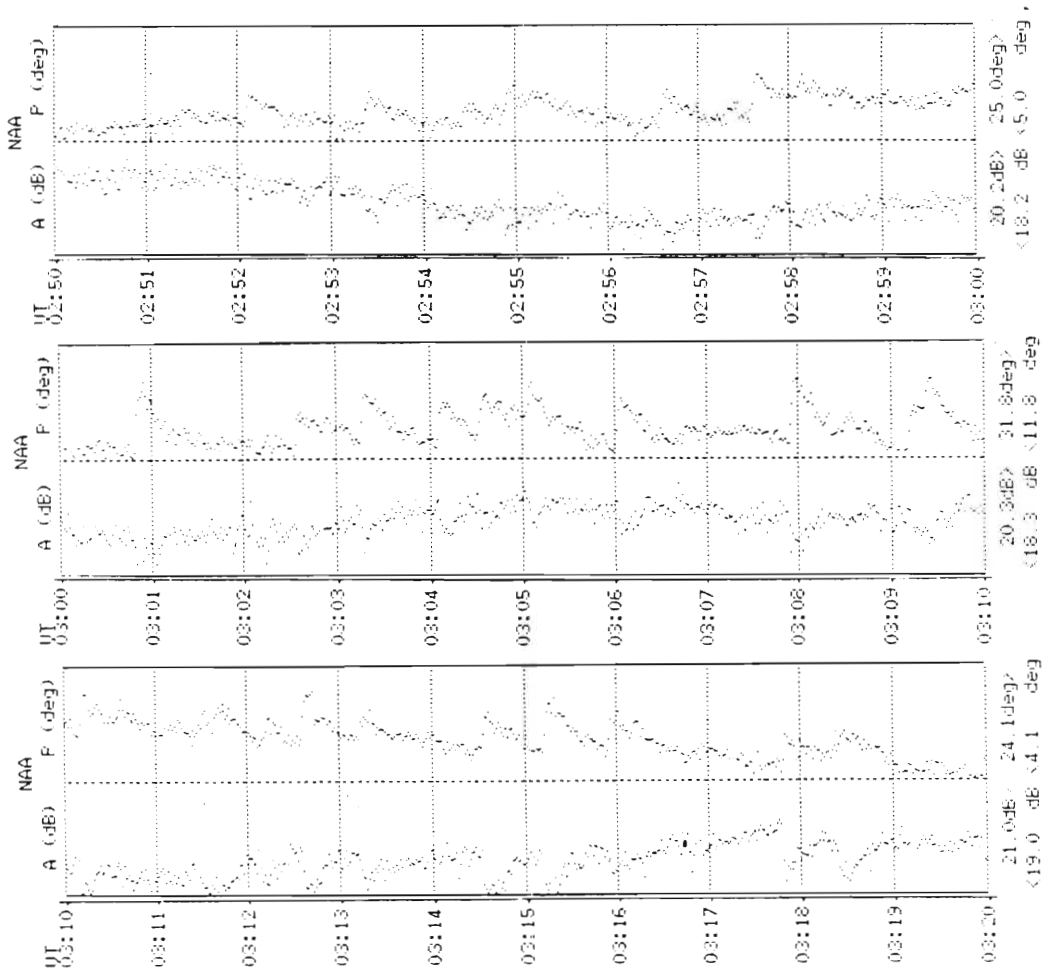


Figure 6.10: OMSKI data for NAA, 02:50–03:20 UT on 13 July 1991. Each panel is individually scaled, amplitude plots have a 2 dB range and phase plots a 20° range

The successive sharp increases and phase followed by a slower decay can be seen clearly, while the amplitude decreases are less obvious but can be easily associated with the phase events. Event rates in this data subset are as high as 1 per minute, which compares well with previously published rates ([Hurren et al., 1986]) Here

new events occur before full recovery of the previous ones, making measurement of recovery times difficult. The distribution of these events in amplitude and phase are shown in Figure 6.11. All the events in this set are of the negative/positive type and are similar, with amplitude around -0.4 dB (see figure 6.11[a]) and phase 2° – 8° (see Figure 6.11[b]) suggesting that the precipitation occurs roughly near the same position along the path (see section 2.7.1). Events of this type can be explained by the single mode, on-path model of [Inan and Carpenter, 1987]. Events designated 0 dB in Figure 6.11 are events which have a phase perturbation but no identifiable amplitude perturbation.

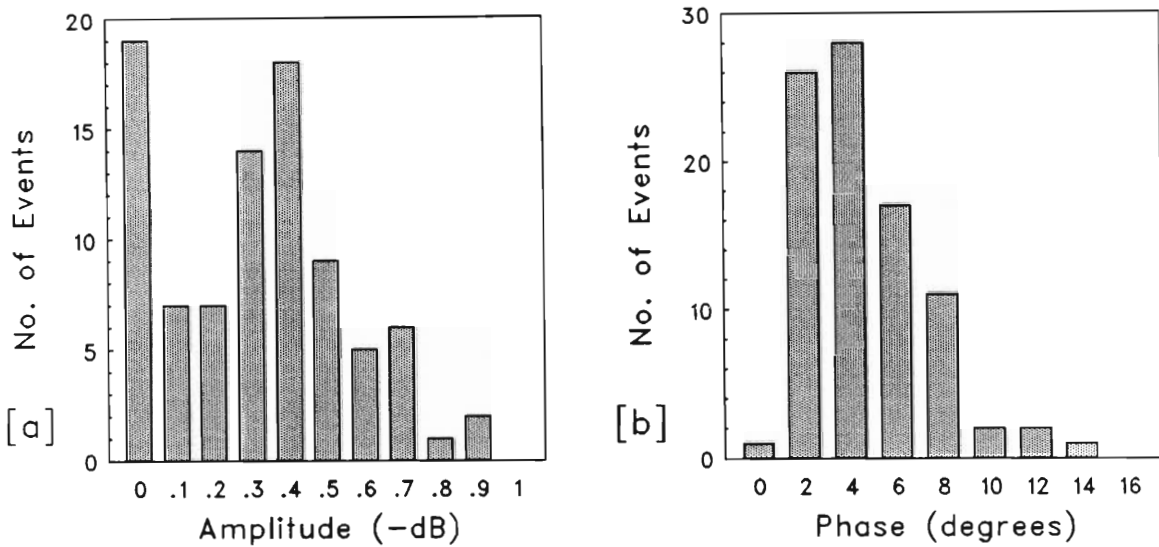


Figure 6.11: Detailed analysis of active NAA data set. [a] shows the number of events at a range of amplitude perturbations, and [b] the number of events at a range of phase perturbations

The generally low occurrence of events can be explained by the absence of thunderstorm activity over the subcontinent in winter (July). Considering the accepted trimpi scenario (see Figure 1.2) a high occurrence of trimpi events can be expected during high thunderstorm activity over the South African subcontinent: lightning will launch northward travelling whistler mode waves which interact with southgoing electrons which will precipitate in the vicinity of the thunderstorm centres (~ 150 km, Inan et al., 1988b). The main centres of thunderstorm activity over South Africa lie on the Witwatersrand and the Orange Free State, going up through Botswana to northern Namibia, and the main period of thunderstorm activity is in the southern summer, January – April. The only path which directly crosses this region is the NAA–Durban path (see Figure 6.4). Thunderstorm activity in winter is rare but not entirely absent. According to the SA Weather Bureau (M. Steyn, private communication) a large isolated thunderstorm occurred over the central Orange Free State on the 13th of July covering the period of high trimpi activity on NAA. The isolated nature of the thunderstorm also explains the uniform nature of the event signatures. The storm occurred in a limited region only, covering approximately 50km^2 . Since trimpis

occur mainly within 150 km of their associated lightning strike [Inan et al., 1988b] their effects on the NAA signal are likely to be similar, since over this distance no drastic change of event type takes place, if one considers the position of the precipitation patch with respect to the great circle signal path (see Figure 2.12).

6.4.4 Daytime Events

These events are of particular importance since they indicate very energetic precipitation and have also been reported by OMSKI studies at Faraday and Halley [Smith et al., 1991b]. Due to the higher level of ionospheric ionisation during the day, electrons of lower energy (~ 40 keV) do not have a sufficient ionisation rate at VLF reflection height (60 – 90 km) to significantly alter the background ionisation levels and thus effect VLF signals. Electrons of high energy, however, have their maximum ionisation rate at much lower altitude. The results from [Rees, 1963, Rees, 1969] show that for 10 keV electrons the maximum ionisation height is about 105 km, while for 100 keV electrons this height drops to 85 km and to 60 km for 1 MeV electrons. Since at low L gyroresonance occurs with relativistic electrons ($E > 100$ keV, see Figure 5.3) one might expect to see trimp events at a time when the path under consideration is in sunlight. Under normal conditions the D-layer shows strong solar control. The effect on VLF reflection height is that during the day it is reduced by about 15km ([Bracewell and Bain, 1952]), further favouring high energy electrons in producing disturbances of the VLF reflection height during the day.

Thus WIEP at higher latitudes ($L \sim 4$) consist of lower energy electrons (~ 40 keV) and can effect subionospheric VLF only in the nighttime D-layer. Consequently, almost exclusively, only nighttime events are reported at high and medium latitudes ([Helliwell et al., 1973]). At low latitudes this constraint falls away and one should expect a more even diurnal distribution of events.

The number of events in hourly bins is shown in Figure 6.12. The events that occurred during the active period on NAA are shown separately since they are an unusual occurrence in this dataset. No clear diurnal variation can be seen within the constraints of this limited dataset of 313 events. It is, however, clear that a significant number of events occur during the day when either the whole or part of the path to Durban is in daylight, confirming the prediction made above. The “low” in events near 13:00 UT is probably due to the fact that most of the signal strengths are at a low at that time due to the unfavorable daytime VLF propagation conditions, signals are noisier and trimp events thus more difficult to detect.

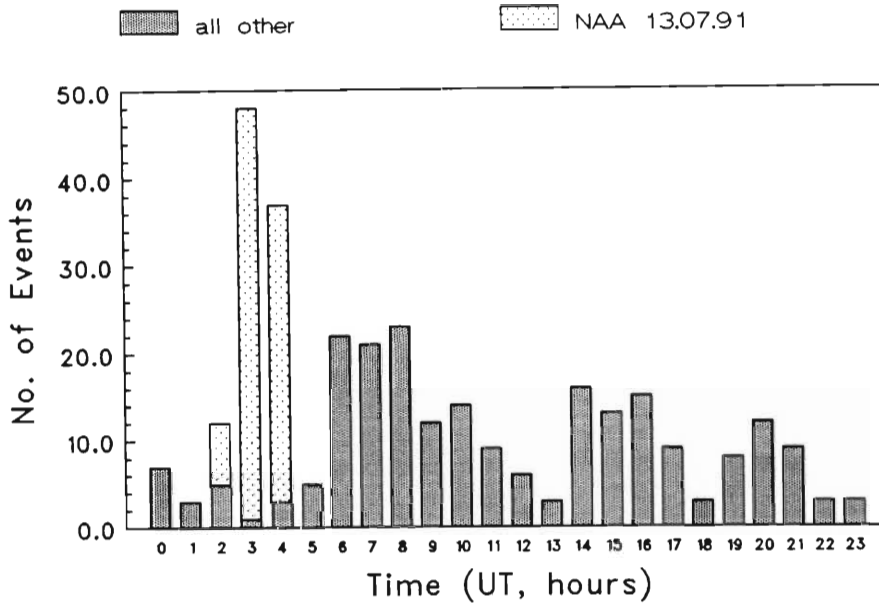


Figure 6.12: Distribution of events in UT for the 27 June – 27 July dataset. The dark bars show the distribution excluding the high activity period on NAA, which is shown superimposed with the dotted bars

6.5 Problems

In comparison to data received at quiet sites such as the Antarctic, Durban is a very noisy site as can be seen from Figure 6.5. At most times detection of small trimp events is impossible.

The data analysis performed here is manual, involving the printout of the data using a dot-matrix printer in graphics mode followed by visual inspection. This is not only time consuming and labour intensive, but also produces large amounts of data - the combined printouts for the month's data examined in this chapter stands about 50cm high!

The OMSKI system at Durban is based on IBM compatible PC's, which have limited software available for data analysis. The original trimp detection and computerised measurement routines were written on Apple Macintosh, and this analysis method was reported by [Adams et al., 1990]. The S.P.R.I. is in the process of switching to Apple Macintosh for further data analysis, which greatly facilitates the processing of large volumes of simultaneous, multi-frequency, multi-receiver data. This is especially important with OMSKI2 coming on line in December 1991.

Further plans for the OSMKI's are discussed in 8.3.1.

Chapter 7

The Effect of Magnetic Field Distortions on Gyroresonance at Low L -values

In this chapter a new magnetic field model is developed for modelling various magnetic field distortions. This model is then used to study the effect of such distortions upon the gyroresonance condition, and is further incorporated into the test particle simulation of Chapter 5 to calculate the effect this has on pitch angle change due to the gyroresonance interaction.

7.1 Why Model Ambient Field Distortions?

The gyroresonant interaction as part of the chain of events leading to a trimpi event has been well established, as has been lightning as a VLF source for the interaction. It is indeed difficult to imagine another VLF source which would lead to the observed sharp event onset. Lightning is responsible for both the “fast” (direct ionospheric heating) and normal trimpi event (gyroresonant interaction along a field line near the equator), but the latter account for about 90% of all events observed [Inan et al., 1988b].

This thesis reports on trimpi events observed at very low L (see Chapters 4 and 6) which also include a number of daytime events, for which the ionospheric conditions require strong and energetic precipitation in order to affect the daytime VLF reflection region. In section 5.1 it was shown that for normal whistler frequencies highly energetic electrons are resonant, fulfilling one of the requirements. However, the results of the relativistic test particle simulation of Chapter 5 have shown that overall conditions for effective gyroresonance are not favourable at very low L , in particular:

- (a) large wave intensities are needed ~ 150 nT,

- (b) electrons are relativistic: this leads to short interaction times ~ 5 ms,
- (c) and the resonance condition is critical.

In order to explain the occurrence of trimpi events at low L in spite of the apparent inefficiency of gyroresonance interactions at low L the interaction itself has to be modified.

There are several ways in which the interaction can be made more efficient apart from fulfilling the conditions listed above. Higher wave frequencies would reduce the required resonant energy and increase the interaction time and lower the required wave intensities. It was already pointed out in section 5.5 that the higher frequencies from lightning are strongly attenuated, so this condition cannot be met (see figure 5.12, eg. intensities between 10 and 30 kHz decrease by 20 and 10 dB for night and day conditions respectively). Given the set range of whistler frequencies and the required high resonant energies leaves the resonance condition as the only possibility. Any phenomena which effectively allows particle and wave to be in resonance for a longer time is likely to increase the pitch angle change due to the interaction. The stability of the phase trapping during the interaction is therefore extremely important: cumulative pitch angle changes occur only during trapping which thus controls the interaction time.

From the gyroresonance condition we know that for resonance the wave frequency ω_w has to be doppler-shifted to match the electron gyrofrequency ω_H (see 2.20), and this condition is in general only satisfied at one point along a field line. Particles have to be very near resonance for trapping (see section 5.3), so in order for the trapping region to be extended the region over which the resonance condition is well satisfied has to be extended. Particles move out of resonance due to changes in

- (a) ω_H (see equation 2.11) which depends mainly on the background field strength,
- (b) the whistler mode phase velocity v_p (see equation 2.8) which depends on ω_H and ω_p (and thus the background electron density n),
- (c) the whistler frequency ω_w which effects the resonance condition in equation 2.20 directly and indirectly through k (i.e. v_p).

Point (3) was taken up by [Brinca, 1981] where it was shown that using specially modulated VLF injection, with the correct frequency/time relation, the resonance condition can be satisfied by continuously adjusting the wave frequency along the field line, and that the resulting change in α_{eq} in such an interaction is much larger than for a CW signal. This result does, however, not help to increase the efficiency of gyroresonance interactions as required here, unless natural whistlers or other naturally generated VLF have the right frequency/time signature. This point is further discussed in section 7.5.

Point (2) involves dependence on n along a field line. Such distributions are commonly calculated from the models used in Park [1972] and are not well known from an experimental point of view, with no actual measurements of density modulations along field lines known to the author.

This leaves point (1) which is the one studied in this chapter. Any change in B_0 (the rate of change of the magnitude of the magnetic field along a field line) which “flattens” field lines, thereby reducing $\frac{dB}{dt}$, will keep the magnetic field strength invariant for a larger region, and since the magnetic field is naturally “flat” near the equator such flattening will be most effective in that region. Distortions of the background field of this kind occur in nature, in natural deviations from the ideal dipole field, in the day side compression of the magnetosphere and most importantly in pc-4 and pc-5 magnetic pulsations (cavity mode oscillations). These can modify the background field strength up to 10% over periods of ~ 100 s which is of several orders of magnitude longer than the typical interaction time at low L .

7.2 A New Background Magnetic Field Model

In order to model magnetic field distortions of the type required above, a new dipole-like field model was developed. The model had to be reasonably simple in order to cut the required computing time, since many of the parameters for particle and wave motion in the test-particle simulation employed here depend on B_0 .

The model used here is based on the Leonovich-Mazur Field Line Equation:

$$r = r_0 \cos^\mu \theta \quad (7.1)$$

where r is the distance from the center of the earth, r_0 the radial distance at the equator and μ the parameter to change field line curvature. A plot of field lines for different values of μ at $L = 2$ is shown in Figure 7.1.

Working back from equation 7.1 yields the general vector field equation for the magnetic field, which is “dipole-like”:

$$\bar{B} = \frac{M}{r^x} [-\mu \sin \theta \hat{r} + \cos \theta \hat{\theta}] \quad (7.2)$$

μ and x in equation 7.2 are not independent: Maxwell’s equation $\nabla \cdot \bar{B} = 0$ requires that

$$\mu = \frac{2}{x - 2} \quad (7.3)$$

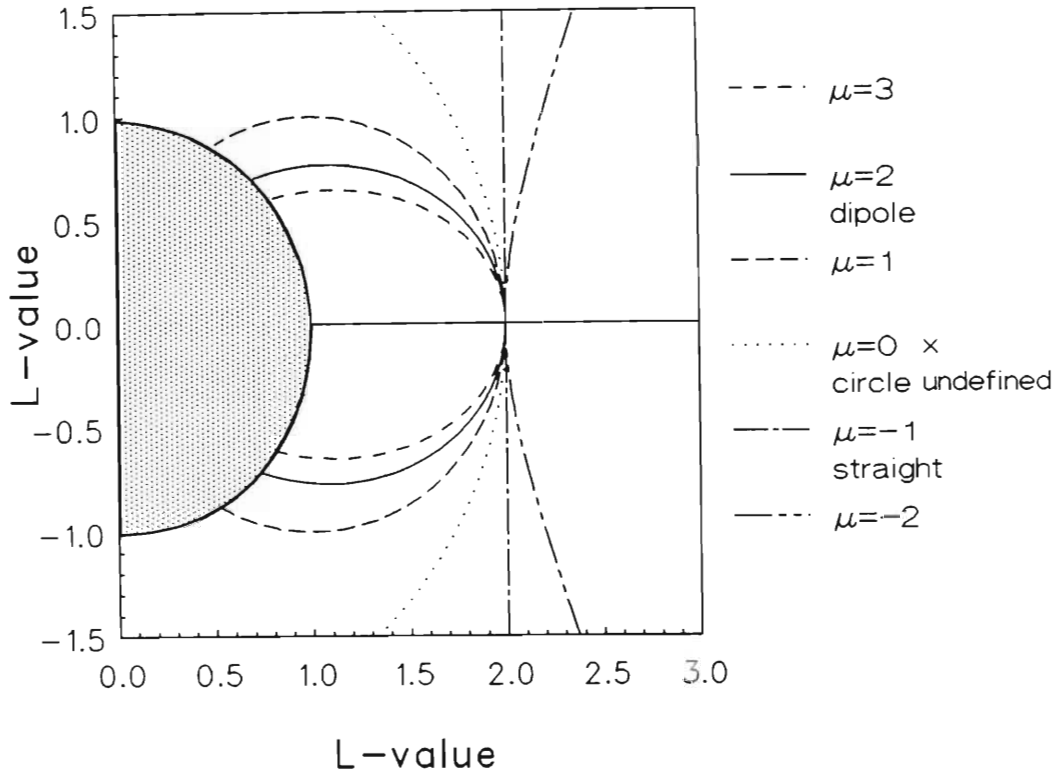


Figure 7.1: Plot of $r = r_o \cos^\mu \theta$ at $L = 2$

where $\mu = 2$ and $x = 3$ is the normal dipole field solution. The equations for total field strength B and field strength along a field line B_f can now be written as:

$$B = \frac{M}{r^x} (1 + [\mu^2 - 1] \sin^2 \theta)^{1/2} \quad (7.4)$$

$$B_f = \frac{M (1 + [\mu^2 - 1] \sin^2 \theta)^{1/2}}{r^x \cos^{\mu x} \theta} \quad (7.5)$$

$$(7.6)$$

This model uses only one parameter to change the field and is simple to compute. Field line curvature increases for $\mu > 2$ (dipole) and decreases for $\mu < 2$. Maxwell's condition $\nabla \cdot \vec{B} = 0$ cannot be satisfied for $\mu = 0$ (circle) and for values of $\mu < 0$ field lines are open. Open field lines are not physically present at low L but near the equator the model can still be used to model negative curvatures of field lines (Figure 7.1).

Figure 7.2 shows the variation of B_0 strength along a field line under the new model. As μ is increased (from $\mu = 2$, dipole) the field changes more and more rapidly off the equator and the homogenous region around the equator is much reduced. As μ is reduced the field becomes more and more flat until curvature increases again due to field lines bending away from the earth. The zoomed

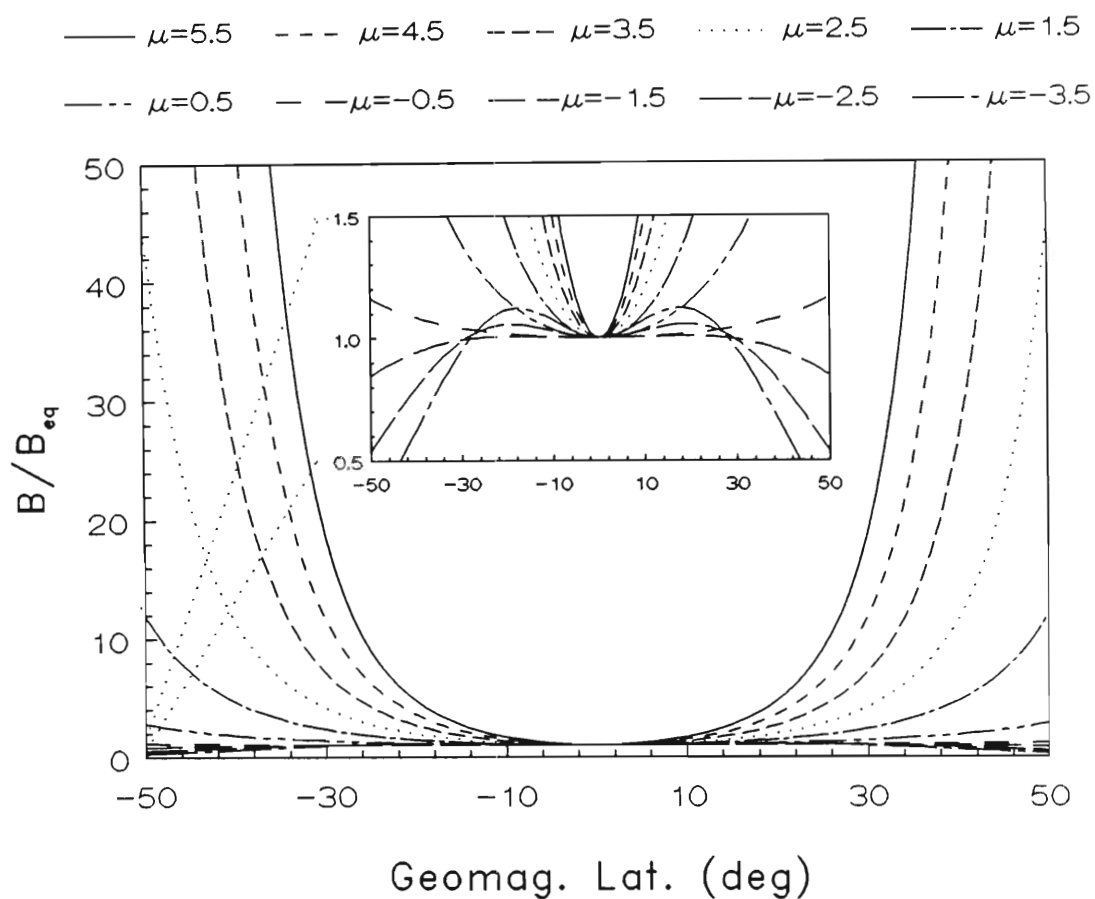


Figure 7.2: Variation of B along a field line normalised with respect to B_{eq} as a function of latitude for a range of new field parameter μ

section of Figure 7.2 shows in more detail the behaviour around the equator showing that for $\mu < -1.5$ B first increases before it decreases off the equator, which can be used to model higher order cavity modes [Pekrides, 1989] near the equator.

The rate of change of B along a field line under the new model is shown in Figure 7.3. This shows clearly that a near constant field along a field line can be modelled with $\mu \sim -0.5$. Figure 7.3 is calculated for $L = 2$, but can easily be scaled for other L since $\frac{dB}{Bdl} \propto 1/L$ and only varies by a factor of 2 in the L -range ($1.2 < L < 2.0$) considered here:

$$\frac{dB}{Bdl} = \frac{\frac{dB}{Bd\lambda}}{\frac{dl}{d\lambda}} \quad (7.7)$$

where $\frac{dl}{d\lambda}$ is the rate of change of the arc length l along a magnetic field line with respect to the geomagnetic latitude λ , which can be written as

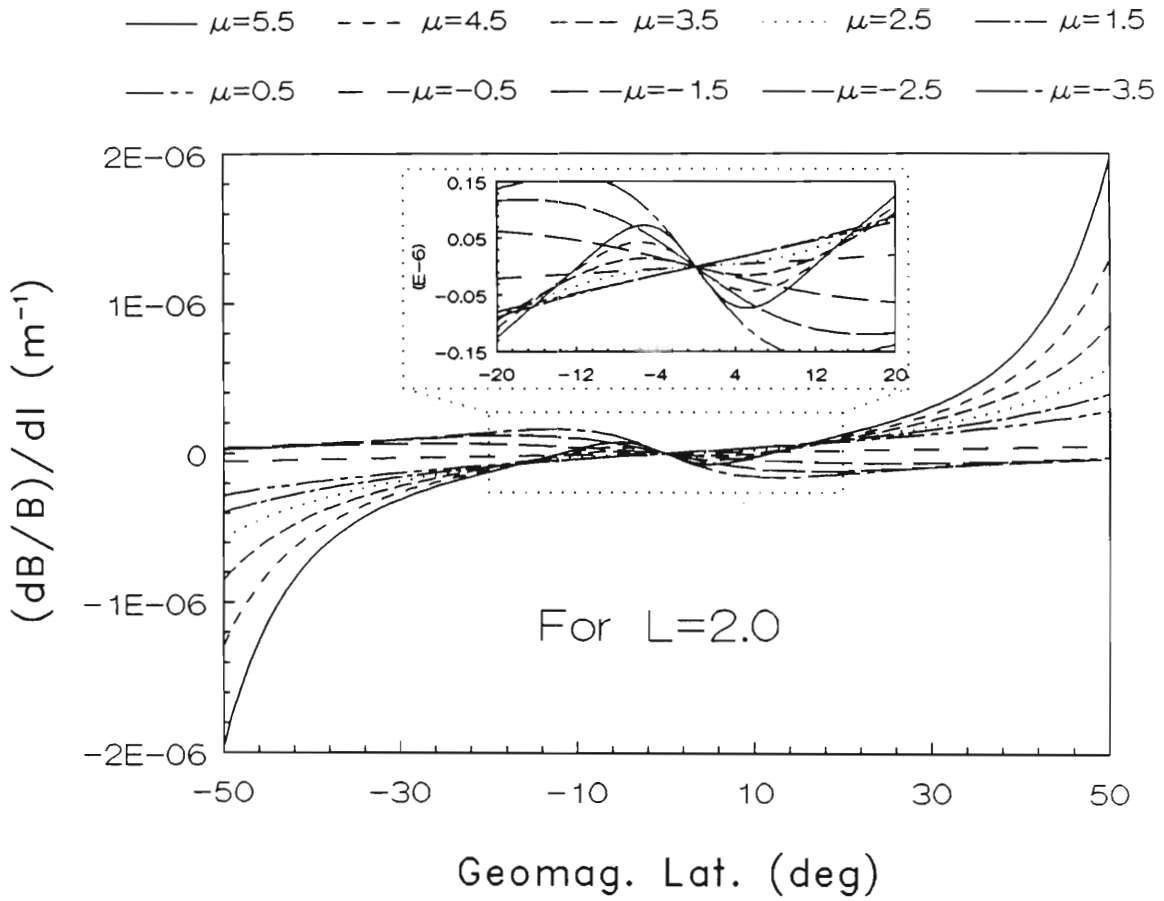


Figure 7.3: Variation of $\frac{dB}{Bdl}$ along a field line (normalised with respect to B) as a function of latitude for a range of new field parameter μ

$$\frac{dl}{d\lambda} = r_0 \cos^\mu \lambda (1 + \mu^2 \tan^2 \lambda)^{\frac{1}{2}} \quad (7.8)$$

and since r_0 can be written as $r_e L$ substituting equation 7.8 into equation 7.7 shows the proportionality $\frac{dB}{Bdl} \propto 1/L$.

7.3 Resonance Condition along a Field Line under the New B -Field Model

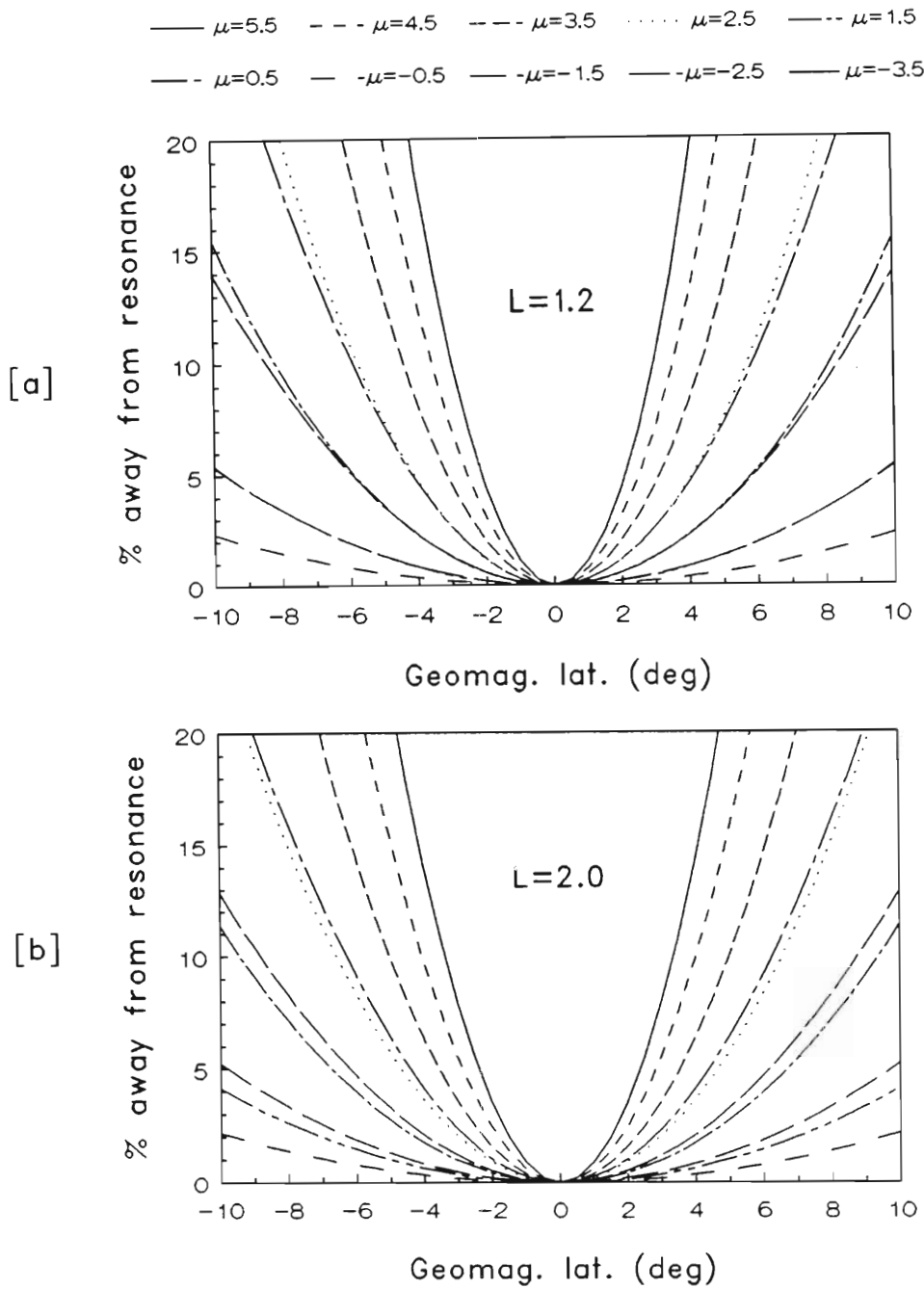


Figure 7.4: Resonance condition ϵ along a magnetic field line as a function of latitude for $L = 1.2$ [a] and $L = 2.0$ [b] for various values of new field parameter μ . The dipole case $\mu = 2$ lies between the curves for $\mu = 1.5$ and $\mu = 2.5$

The relativistic gyroresonance condition (equation 5.1) is re-calculated here for various values of the new field parameter μ . The same condition as used in Chapter 5 to delineate the interaction region is used here (ϵ , the % away from

resonance, where $\epsilon = \frac{|v_{\parallel} - v_r|}{v_{\parallel}}$). In general, at the low L -values considered here, ϵ must be less than 2% for stable trapping. Figure 7.4 shows the results for $L = 1.2$ (7.4[a]) and $L = 2.0$ (7.4[b]).

There is not much change in ϵ between the two L values due to the $1/L$ dependence of $\frac{dB}{Bdt}$. In both cases the ϵ away from the equator decreases as μ is decreased from the tightly curved field at $\mu = 5.5$ and reaches “best case resonance” near $\mu = -0.5$ (detailed calculations show that the best resonance behaviour is obtained for $\mu = -0.387$) before becoming worse again for $\mu < -1.5$ as the field curves away from the earth. Figure 7.4 also clearly illustrates how a small change in μ can significantly increase the region of “good” resonance ($\epsilon < 2\%$). For $\mu \sim -0.4$ the region of effective resonance (particle within 2% of resonance) extends to $\sim 10^\circ$ either side of the equator, compared to $\sim 3^\circ$ for a dipole field. This trebles the available interaction time.

The results here are for low L but apply equally well at higher L and can be roughly scaled on a $1/L$ dependence. This indicates that the resonance conditions are about twice as good at $L = 4$.

7.4 Test Particle Simulation Results at $L = 1.7$ under the New B -Field Model

The test particle simulation employed in Chapter 5 was extended to include the new B -field model (equations 7.3, 7.5) and 7.6 and the equations of motions were adapted accordingly. In order to show the effect of different field curvatures on the gyroresonant interaction, the simulation was run for a range of μ for a typical set of parameters shown in Table 7.1.

Wave Frequency	$\omega_w =$	4	kHz
Wave Intensity	$B_w =$	100	nT
Equatorial Pitch Angle	$\alpha_{eq} =$	$\alpha_{lc} + 1^\circ$	degrees
Durban L -Value	$L =$	1.7	
Eq. Electron Density	$n_{eq} =$	10230	cm^{-3}

Table 7.1: List of parameters used for new B -field test particle simulation

Particles are started off at the equator, at resonance, in the presence of CW (Continuous Wave) of the above given intensity and frequency. The results of this simulation are shown in Figure 7.5.

The simulation was run for all possible values of initial phase ϕ_0 in one degree steps. For a definition of ϕ see section 5.1. μ is varied from dipole ($\mu = 2.0$) down towards and one step beyond best case resonance. Figure 7.5 shows that the scattering efficiency towards negative pitch angle changes (and thus towards the loss cone) increases as the field curvature is decreased from dipole, reaching a

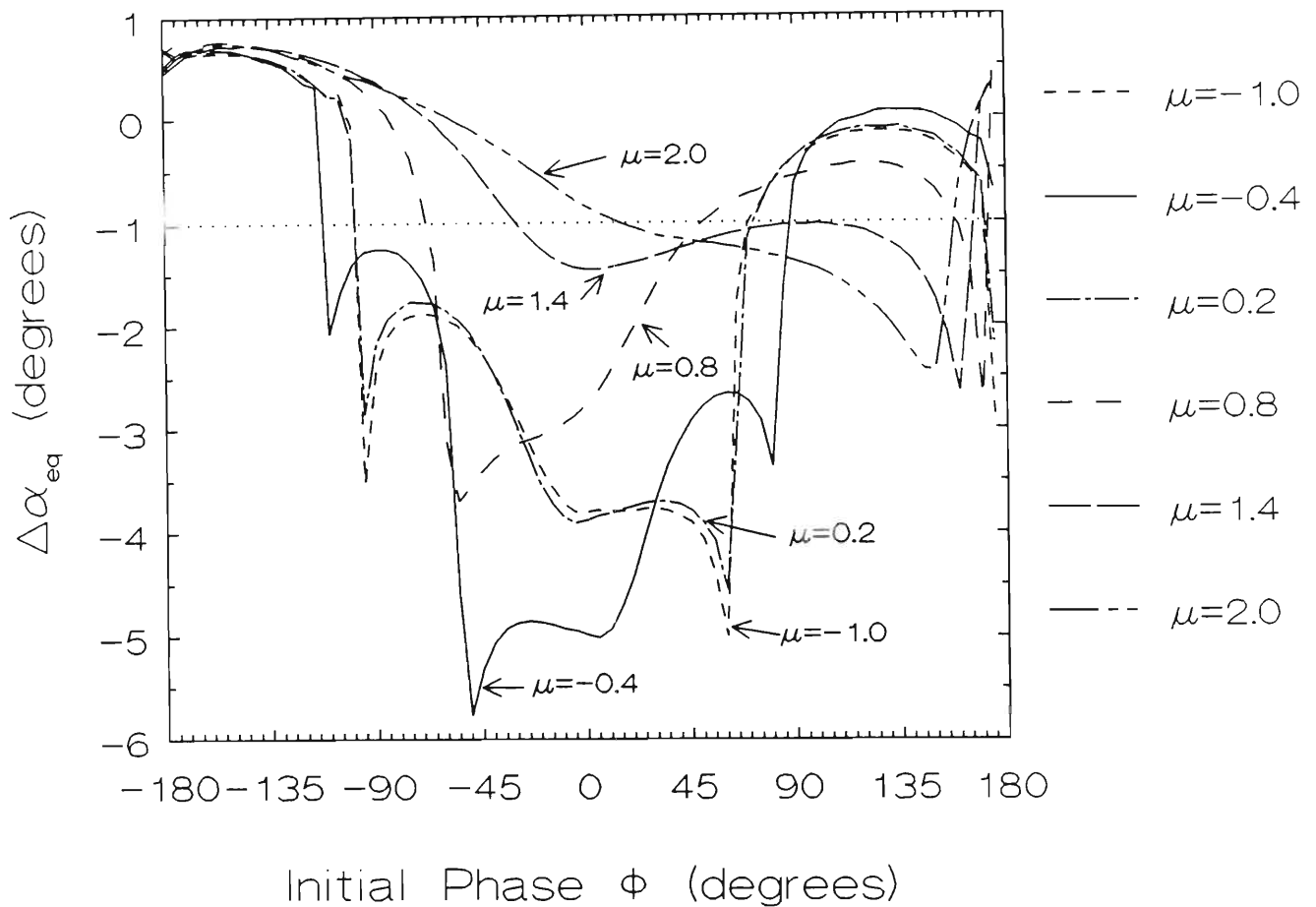


Figure 7.5: Plot of change of equatorial pitch angle as a function of ϕ_0 for various values of new field parameter μ

maximum for best case resonance ($\mu \sim -0.4$) before decreasing again. The same criterion for ϵ was used here as in chapter 5. In Figure 7.6 the loss-scattering coefficient S_L as defined in equation 5.17 and the RMS scattering are plotted as a function of μ clearly showing the behaviour described above.

The results here show that the magnitude of pitch angle scattering towards the loss cone can be significantly increased for even a small change in field curvature. For some critical value of μ a large part of the scattering curve in Figure 7.5 suddenly crosses the loss-cone (dotted horizontal line) and can thus suddenly move a large number of particles in ϕ -space into the loss cone, significantly enhancing the resulting precipitation. It is believed that this mechanism enables the significant WIEP events to take place which are responsible for the trimpi events observed at low L (chapters 4 and 7).

For the example shown in figure 7.5, this occurs at $\mu \sim 1.4$. Not shown here is the corresponding effect resulting from an increase in field curvature and a worsening of the resonance condition: For $\mu > 2$ and $\mu < -2.5$ the resulting pitch angle scattering is worse than for the dipole case leading to a drastic quenching of the interaction.

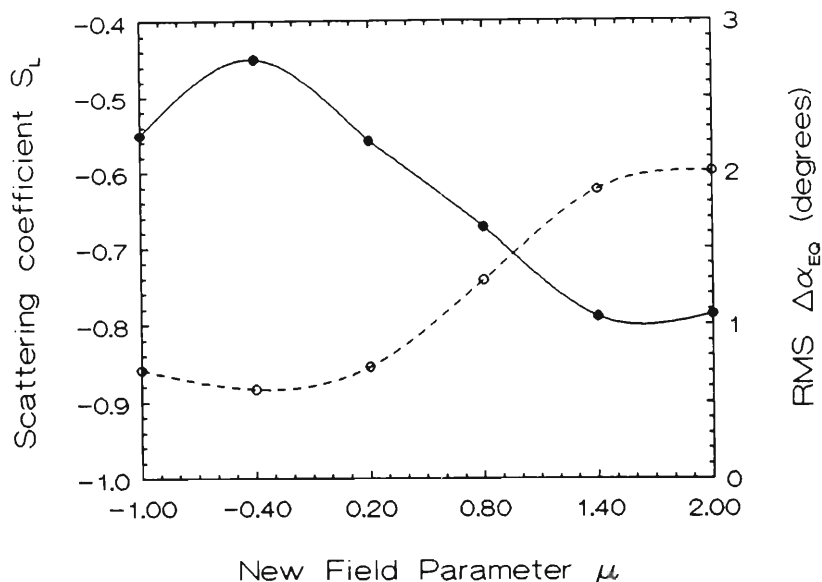


Figure 7.6: μ -dependence of the RMS $\Delta\alpha_{eq}$ (full line, right y-axis) and S_L (dotted line, left y-axis)

7.5 Resonant Frequency along a Field Line

So far in this thesis resonance with single frequency waves only has been considered, and this has led to a limited interaction region since the resonance condition is only satisfied along a short section of the field line for an electron of given energy. This chapter has shown how a change of ambient field can increase the interaction region for a single frequency wave; another way is to change the frequency of the wave in such a way as to satisfy the changing resonance condition along the field line (see equation 5.1). [Brinca, 1981] has performed similar calculations using the non-relativistic resonance condition (see equation 2.20) at $L = 4$, here the first such calculations for low L are presented.

Figure 7.7 shows the local resonant frequency for an electron which is resonant with a 4 kHz wave at the equator (at $L = 2$), along a magnetic field line.

The calculations have been done for an electron of 250 keV energy. Near its mirror points the electron has a large pitch angle and thus needs a high resonant frequency. At the equator the resonant frequency is at a minimum, 4 kHz in this case. The numbers 1–8 on the diagram refer to certain positions along the field line, corresponding to figure 7.8 and will be explained later.

Given the position of the electron along a field line as a function of time, and its resonant frequency at each point, at what time does a whistler wave of the correct frequency have to be injected at the opposite hemisphere so that it meets the electron at the right resonance position? By finding the whistler travel time for each frequency to its resonant point along the field line, and knowing the timing of the electron, a frequency/time characteristic of the input wave structure can

TRAVEL TIME (ms)

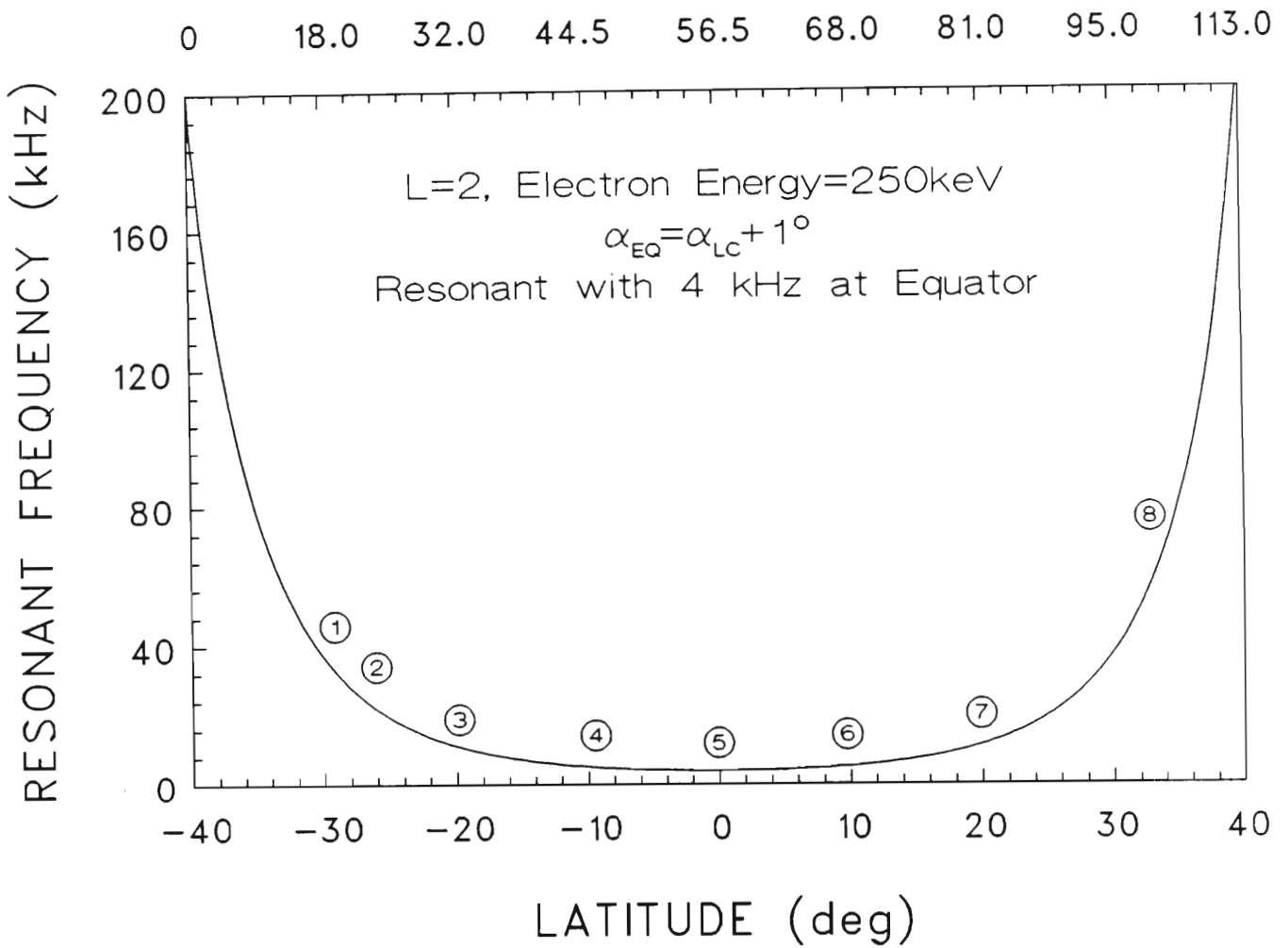


Figure 7.7: Local resonant frequency as a function of geomagnetic latitude. The top x-axis shows electron travel time with $t = 0$ at the mirror point in the southern hemisphere (non-linear scale). Numbers correspond to numbers in figure 7.8

be found which keeps the electron in resonance with the correct frequency wave for it's entire travel along a field line.

The travel time of a whistler wave propagating along a geomagnetic field line has been well established. The result from [Park, 1972] is used here:

$$t(\omega) = \frac{1}{2c} \int \frac{\omega_p}{\omega^{1/2} \omega_H^{1/2} (1 - \frac{\omega}{\omega_H})^{3/2}} dl \quad (7.9)$$

where $t(\omega)$ is the travel time for a whistler wave of frequency ω , and dl is an element of arc along a field line. To find the travel time of the whistler wave from its injection point at the opposite (northern) hemisphere equation 7.9 is integrated from 100 km height along the field line up to the point at which that frequency is resonant. Integration here is done with respect to geomagnetic latitude, so dl in equation 7.9 is expressed as

$$dl = LR_e \cos(\theta) \sqrt{1 + 3 \sin^2(\theta)} d\theta \quad (7.10)$$

where R_e is the radius of the earth and θ is the geomagnetic latitude.

For each point along the field line the travel time for the frequency as given in figure 7.7 is found. The results are shown in figure 7.8.

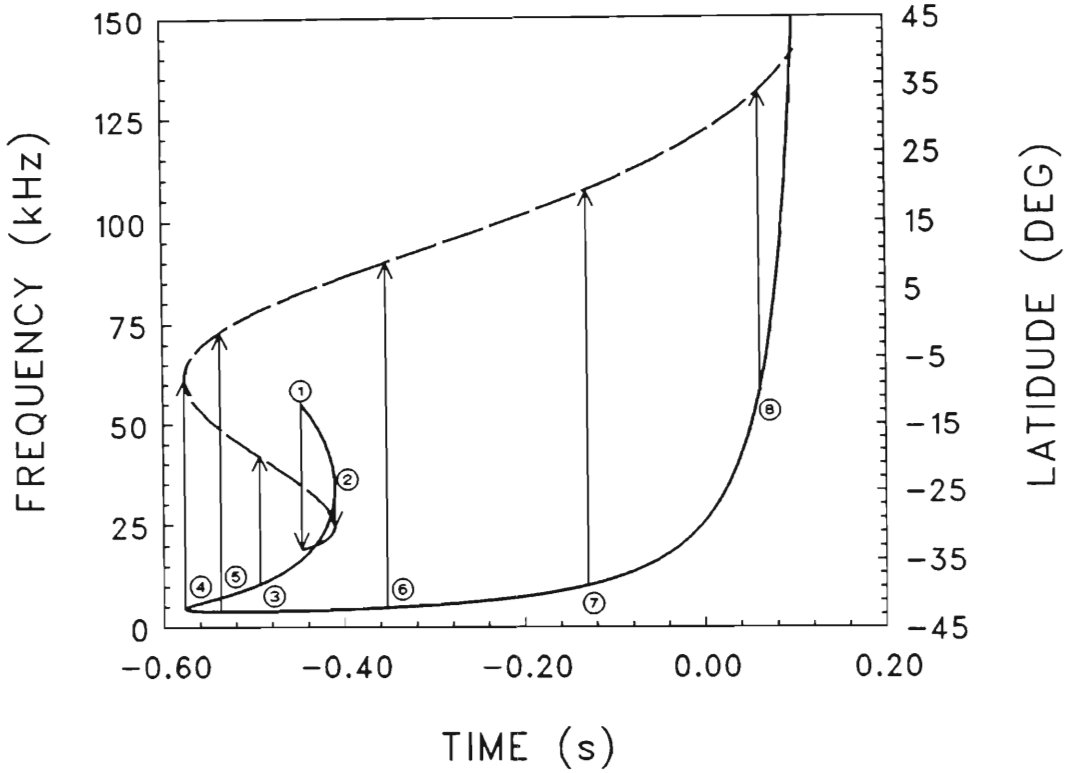


Figure 7.8: Frequency/time format of the required input wave in the northern hemisphere to be in resonance with the electron of figure 7.7. The solid curve is plotted against the left y-axis showing the frequency of the wave, and the dashed curve against the right y-axis, showing at which latitude that frequency is resonant. $t = 0$ at electron mirror point in southern hemisphere. Numbers correspond to numbers in figure 7.7

The results shown in figure 7.8 are explained by following the numbers 1–8 which follow the electron trajectory along the field line from south to north. The arrows in figure 7.8 point to the corresponding resonant latitude on the dashed curve. $t = 0$ is the start of the electron south–north bounce and is taken as the reference time in this calculation:

- (a) The first possible resonant frequency is 55 kHz. This wave has to be injected at the northern end of the field line at $t = -0.442$ s and the resonant point is at $\theta = -33^\circ$. Resonance at an earlier point along the electron trajectory is not possible since the resonant frequency is above $1/2$ of ω_H before the

resonance point is reached

- (b) At $\theta = -30^\circ$ the resonant frequency has reduced to 32 kHz, and this wave has to be injected at $t = -0.404$ s
- (c) At $\theta = -20^\circ$ the resonant frequency has reduced to 12 kHz, and this wave has to be injected at $t = -0.488$ s
- (d) At $\theta = -9^\circ$ the resonant frequency has reduced to 5 kHz, and this wave has to be injected at $t = -0.571$ s
- (e) At $\theta = 0^\circ$ the resonant frequency is at its minimum at 4 kHz, and this wave has to be injected at $t = -0.533$ s
- (f) At $\theta = 10^\circ$ the resonant frequency has slightly increased again to 5 kHz, and this wave has to be injected at $t = -0.350$ s
- (g) At $\theta = 20^\circ$ the resonant frequency has increased to 12 kHz, and this wave has to be injected at $t = 0.129$ s
- (h) At $\theta = 33^\circ$ the resonant frequency has increased to 55 kHz, and this wave has to be injected at $t = 0.067$ s

Frequencies above the whistler cut-off frequency can resonate with the electron in its northern section of travel, this is because the whistler mode waves do not travel all the way to the equator where ω_H is the lowest.

A wealth of information can be gathered from figure 7.8. Firstly it gives the input format for a VLF wave train which would result in the longest possible interaction time for one bounce of the electron: Resonance all along the field line. For the WIEP events considered in this thesis the source of VLF waves is a whistler. At its source, a lightning strike, the frequency time signature is a spheric, which would be a vertical line in figure 7.8. There are only two regions along which the frequency/time curve of the required VLF input approaches a spheric signature. The first region is near $t = -0.404$ and covers frequencies in the range 20–30 kHz, and the second region is at the end of the electron's bounce, near $t = 0.10$, and covers frequencies from 125 kHz upwards.

Both these ranges are outside the normal whistler frequency range and are heavily attenuated (see figure 5.11). A whistler will thus not be able to “track” the resonant frequency of the electron successfully.

The calculations here are for $L = 2$ and for resonance at the equator with a strong whistler frequency. The conditions become worse for both lower frequencies and lower L -values, since the resonant frequencies are even higher. The overall shape of the curve in figure 7.8 is however maintained.

Figure 7.8 does however show that frequencies in a narrow range from 4–5 kHz, near the equatorial resonant frequency, are in resonance for a long period, covering about 16° near the equator. Such a wave input format can be more easily

achieved from a man-made source, notwithstanding the inefficiency and size VLF transmitting antennae. For a given installation there is only a narrow range of frequencies over which a significant amount of energy can be radiated (e.g. the Siple transmitter in the Antarctic).

Chapter 8

Conclusion and Future Research

8.1 Comparison of Trimpi Activity at SANAE and Durban

Trimpi activity in general depends on many factors such as geographic location, signal path geometry, lightning activity and the distribution of energetic particles near the loss cone. All these factors are specific to a particular receiver site and the chosen signal paths, which makes the comparison of data from different paths difficult, and to some extent meaningless. Such differences however are very useful when interpreting simultaneous data sets for the purpose of imaging WIEP regions [Dowden et al., 1991]. Some comments about the differences between the SANAE and Durban data can however be made:

- (a) Both sites display a unique set of characteristics not previously observed at other sites
- (b) Very large amplitude events are observed at SANAE ($\sim -20\text{dB}$)
- (c) There is evidence that wave particle interactions leading to the trimpi events at SANAE occur with non-ducted whistler mode waves
- (d) Both SANAE and Durban show relatively low occurrence rates. This could be due to the fact that both sites lie east of the South Atlantic Geomagnetic Anomaly and that the drift loss cone of radiation belt particles is virtually empty by the time they drift to SANAE and Durban, reducing the efficiency of gyroresonance scattering
- (e) A drastic increase of events at Durban during thunderstorm activity shows a good correlation of lightning with trimpi activity; in contrast, there is virtually no correlation of events with whistlers at SANAE.
- (f) High energy precipitation at Durban latitudes leads to a significant number of daytime events observed at Durban. Such events are rare at high lat-

itudes, the only other report coming from OMSKI observations at Halley [Smith et al., 1991b]

These comments are based on a limited data set from both stations and are not meant to be exhaustive. Further data is needed, and projects to this end are underway (section 8.3.1)

8.2 Comparison of Gyroresonance at High and Low Latitudes

One of the main questions arising out of this thesis is the question of the effectiveness of the gyroresonant interaction in pitch angle scattering at low L , in the face of the evidence which clearly shows that trimpi events occur at low L -value. The results of this theoretical investigation (see chapters 5 and 7) can be summarised as follows:

- (a) Studies of gyroresonance at middle to high latitudes [Inan et al., 1982] have clearly shown how the trimpi scenario involving gyroresonance pitch angle scattering can account for the observed trimpi events. At $L = 4$ resonance is with sub-relativistic electrons, and the interaction times are long enough (~ 50 ms) to allow whistler mode waves of normal whistler intensities (~ 10 nT) to produce pitch angle scatterings sufficient to scatter particles into the loss cone ($\Delta\alpha_{eq} > 1^\circ$)
- (b) At low L all the conditions for gyroresonance and a strong interaction are less favourable (chapter 5):
 - (a) Resonant electrons with VLF waves are of high energy and have high relativistic masses. They have resonant velocities near c and move through resonance quickly, lowering the interaction time (~ 5 ms). Their higher mass requires larger wave induced forces to change the dynamics of the particle.
 - (b) Higher whistler mode frequencies ($\omega_w > 10$ kHz) can resonate with lower energy particles. These frequencies are, however, heavily attenuated at the top of the ionosphere if one considers a lightning source
 - (c) The background magnetic field strength is larger and larger wave intensities are needed to trap electrons. It is in the trapped mode that large pitch angle scattering occurs
 - (d) The background field is also more curved, which means that the resonance condition changes more quickly along a field line, reducing the interaction region

- (e) Items (a), (c) and (d) require higher wave intensities: For effective pitch angle scattering wave fields of the order of 150 nT are needed, intensities which are not normally present in whistler waves produced by lightning
- (c) The density of radiation belt electrons reduces drastically as energy is increased (see Figure 2.3), which reduces the precipitating flux. However, the ionisation efficiency goes up with energy (see section 6.4.4), leading to similar ionisation enhancements as a larger flux of lower energy electrons would produce
- (d) While at higher latitudes “unaided” gyroresonance is sufficient for large pitch angle scattering, this mechanism may only be successful at low L when the resonance condition is modified in such a way that the interaction time is increased, which in turn enables lower intensity waves to scatter electrons. This can be achieved by background field disturbances such as PC5 pulsations. The model used in chapter 7 clearly shows how even slight flattening of field lines increases the scattering efficiency. This might be a necessary condition for producing trimpi events at low L .

8.3 Future Research

Trimpi research is a vibrant field of work and has been undertaken at Durban since 1988. The trimpi event is fast developing into a tool for the investigation of wave induced precipitation events, and the coverage of various trimpi networks is growing. This thesis represents the first report on the activity of the Durban Group.

8.3.1 Planned Deployment of the S.P.R.I. OMSKI Units

Two units have been purchased to date. OMSKI1 has been operating since April 1991 and OMSKI2 since December 1991. After the first test runs (see Chapter 6, it has been decided to move the OMSKI1 to a quieter site. The second unit will be used initially in conjunction with the first on a short baseline, separated by one wavelength on the NWC MSK signal. The purpose is to use two antennae measurements on trimpi events to investigate the type of scattering from ionisation patches at low L and to find out whether the scattering is due to off-great circle “echoes” [Dowden and Adams, 1989]. The measurement technique to be used here is described by [Adams, 1990], chapter 5.

OMSKI1 will continue to be operated at Durban to build up a year long database on low latitude trimpi activity. The second unit will be used in several field experiments:

- (a) A one week experiment in the Natal Drakensberg which is known to be a very quiet site. The OMSKI will be run in conjunction with a portable goniometer system for broadband VLF reception, to look for causative whistlers and spherics and a magnetometer system looking for magnetic pulsation to investigate the effects of PC5 pulsations on trimpi activity (see chapter 7). The experiment will take place in January 1992 which is at the height of the summer thunderstorm activity over the African subcontinent, which would be a prerequisite for good whistler and trimpi activity. In conjunction with this campaign an equivalent OMSKI unit and a VLF receiver will be operated in Budapest in a joint venture with Dr. János Lichtenberger of Eötvös University, to look for conjugate effects of trimpi activity
- (b) The experiment (1) will be repeated at Marion Island in the period 27 February – 28 March 1991, with the same international participation
- (c) The experiment (1) will be repeated at Gough Island in October 1992
- (d) The unit will be sent to the new SANA E base at Vestlaskarvet mountain (71°S; 2°W) during the 1992/1993 takeover to operate for at least one year in conjunction with the BAS-net of equivalent receivers

It is envisaged that OMSKI type receivers will eventually be operated at all the sites given in Table 8.1

Receiver site	Longitude	Latitude	L-value
Durban	031°00'E	29°53'S	1.69
Gough Island	009°53'W	40°21'S	1.78
Marion Island	037°52'E	46°53'S	2.61
SANA E	002°26'W	70°18'S	4.02

Table 8.1: Sites for the planned S.P.R.I. net of trimpi receivers

The planned S.P.R.I.-net provides vital coverage over the South Atlantic Geomagnetic Anomaly, and over large areas of the oceans south of Africa (see figure 8.1).

8.3.2 The Status of Worldwide Trimpi Networks

Interest is continuing to grow in the use of the trimpi technique for the study of lightning induced electron precipitation and networks of trimpi receivers are continuing to be developed around the world. The IAGA/URSI Joint Working Group on VLF/ELF Remote Sensing of the Ionosphere and Magnetosphere (VERSIM) has become the forum for this type of research.

The following countries are currently involved in trimpi research: (Refer to the map in Figure 8.1 for the great circle paths of the various networks.)

Brazil

A 6-channel tuneable VLF receiver (Stanford type) for operation initially at Itapetinga Radio Observatory, São Paulo (23°S; 48°W, $L = 1.2$) in 1992 and later at the Brazilian Antarctic Station Cmte. Ferraz (60°S; 58°W, $L = 2.2$) in 1993. [Dr. L. R. Piazza, Centro de Radio-Astronomia e Aplicações Espaciais, São Paulo]

France

A new VLF receiver has been installed at Kerguelen Island receiving OMEGA signals and NWC MSK and has been operating since 15 February 1991. It is planned to install a Stanford type receiver in France near Poitiers. [Dr. Y. Curcuff, University of Poitiers]

Hungary

An OMSKI type receiver will operate at $L = 1.9$ to look across the $L=2-3$ triump zone at transmitters such as GBR, Ω -Norway, NAA, etc. Initial operation will be December 1991– April 1992. A cooperation has been set up with the University of Natal group (R. Friedel, Dr. A. R. W. Hughes) since Budapest is nearly conjugate to Durban. [Dr. Gy. Tarcsai, Eötvös University]

Japan

Data from the conjugate experiment of the reception at Ceduna (Australia) of the Kharbarovsk (USSR)($L = 1.93$) VLF transmitter (15 and 23.9 kHz) are being analysed to study nonlinear wave particle interaction together with simultaneous wideband measurements at Ceduna. [Dr. M. Hayakawa, University of Electro-communications, Tokio]

New Zealand

An extended array of OMSKI type receivers for imaging WIEP using VLF paths from NWC and Ω transmitters in Australia. Currently the receiver array includes Dunedin, Swampy Summit, Tumai and Horse range, roughly collinear 9, 31 and 47 km respectively from Dunedin. Further receivers are at Oamaru, Mount John, Wellington and Kaeo, 90, 200, 300 and 1200 km from Dunedin respectively. [Prof. R. L. Dowden and Dr. C. D. D. Adams, Otago Univeristy, Dunedin]

United Kingdom

OMSKI type receivers are at the Antarctic Stations Halley and Faraday, operating again from early 1992 after a year's pause. During the winter 1993 a further receiver will be operated at Rothera station (68°S ; 69°W ; $L = 2.8$) as part of a meridional line of receivers at Faraday and Palmer stations on the Peninsular and Ferraz on King George Island. [Dr. A. J. Smith, British Antarctic Survey]

United States of America

Stanford University continues to operate an extensive network of trimpi receivers in North America (US, Canada, Puerto Rico) and in the southern hemisphere at Palmer station, Antarctica, which is suited to conjugate studies. [Dr. U. S. Inan, Stanford University]. Dr. B. Holzworth operates an OMSKI unit at Seattle.

South Africa

See section 8.3.1.

As can be seen from Figure 8.1 there is very good coverage over the Tasman Sea and North America. There is as yet no coverage over Europe, but the planned systems in Budapest will fill some of this gap. The SPRI-net fills a vital slot in over the southern ocean, and provides good coverage over the South Atlantic Geomagnetic Anomaly.

8.3.3 Other Uses for Trimpi-Nets

As trimpi networks become more comprehensive, virtually the whole globe will be covered with a grid of signal paths which are monitored on a regular basis. With analysis and interpretation methods of the effect of ionospheric disturbances on VLF becoming more refined, a range of other uses apart from trimpi work becomes possible.

The effects of solar flares on the ionosphere are known as sudden ionospheric disturbances (SID). This phenomenon was discovered by Dellinger and is now usually called a shortwave fadeout due to abnormal absorption of the radio signal. The responsible ionisation is in the D-region, which makes it detectable by VLF and is characterised by a sudden phase anomaly lasting about 35 minutes [Mitra, 1975]. These events normally affect the whole sunlit hemisphere of the Earth, and the trimpi-nets are ideally suited to the study of the dynamics of such events.

Solar proton events also cause additional ionisation in the D-region and are confined to higher latitudes, and are often called polar cap absorption events (PCA)

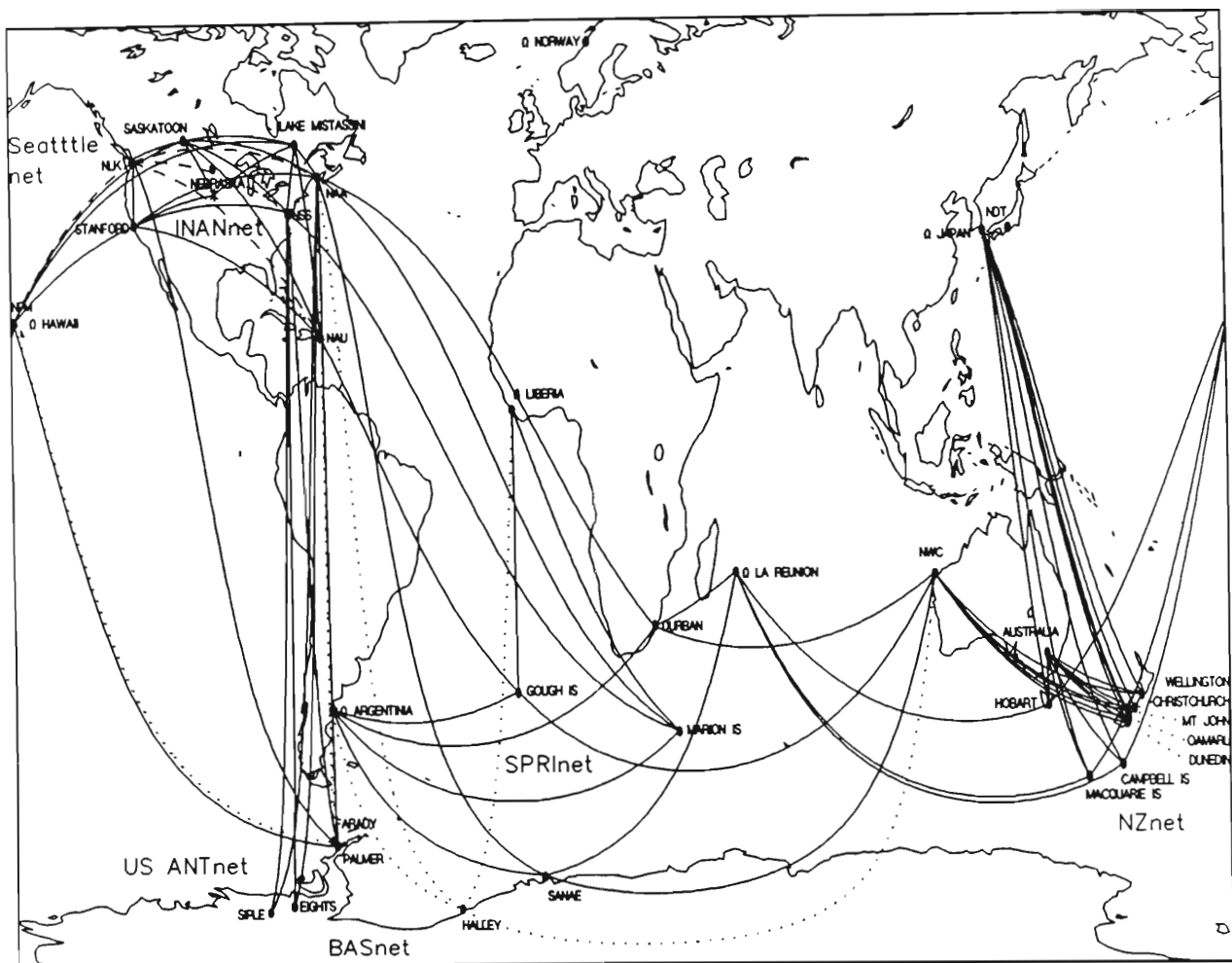


Figure 8.1: Great circle paths of the various world-wide trimpi networks. The network planned by the S.P.R.I. includes the stations Durban, Marion Is., Gough Is., and SANAE

[Zmuda and Poterma, 1972]. They normally occur in conjunction with very large solar flares, and have traditionally been measured with riometers which are locally confined. Trimpi-nets offer a much larger coverage but are limited due to the increased signal attenuation over ice.

Irregularities in the ionospheric E- and D-regions provide a useful method of measuring winds at those altitudes and can be measured by monitoring the reflected VLF signals [Kent, 1970]. Irregularities of large size can be tracked by this method, and are normally evidence of acoustic-gravity waves.

Meteors leave a trail of ionisation as they enter the Earth's atmosphere. These trails are traditionally tracked by radar reflections, but as long as the trails offer a large enough scattering cross section at VLF these waves can also be used to track meteors. With multi-signal path measurements it would be possible to track the path of the meteor quite accurately in order to determine its impact point.

These are a few examples of possible uses of trimpi-nets. Virtually any ionospheric disturbance in the D-region can be monitored using the techniques developed for trimpi work.

On a more global scale the combined trimpi networks can contribute to STEP (the Solar-Terrestrial Energy Program) by helping to estimate the worldwide contribution of precipitating particles to the “energy budget” of the magnetosphere.

Appendix A

Equations of Motion

The equations governing the motion of an energetic particle in a longitudinal whistler mode wave under cyclotron resonance are derived here. The basic assumption for this derivation is that the energetic particle motions do not significantly alter the propagation of the wave. This assumption is justified by the fact that the dispersion and propagation characteristics are governed entirely by the thermal or "cold" plasma component, and the fact that the total density of energetic particles is much less than the cold plasma density. The refractive index, n , is then given by (2.6), and the energetic particles can be considered as a beam of electrons against a cold background which supports the whistler mode wave.

A.1 Derivation of the Equations

For cumulative energy, momentum and pitch angle changes to occur the resonance condition (2.20) must be satisfied. Using the coordinate system in Figure A.1, where v_{\parallel} is the particle velocity along $-\mathbf{B}_o$, equation (2.20) with $m = 1$ is given by

$$\omega - \mathbf{k} \cdot \mathbf{v}_{\parallel} = \omega_H \quad (\text{A.1})$$

The unperturbed motion of energetic electrons trapped along field lines can be described by the following expressions which can be derived from the adiabatic invariant relation (2.13):

$$\left(\frac{dv_{\parallel}}{dt} \right)_u = -\frac{v_{\perp}^2}{2B_o} \frac{dB_o}{dz} \quad ; \quad \left(\frac{dv_{\perp}}{dt} \right)_u = +\frac{v_{\parallel}v_{\perp}}{2B_o} \frac{dB_o}{dz} \quad (\text{A.2})$$

where the subscript u stands for unperturbed motion. The force acting on the particles by the wave is the Lorenz force given by

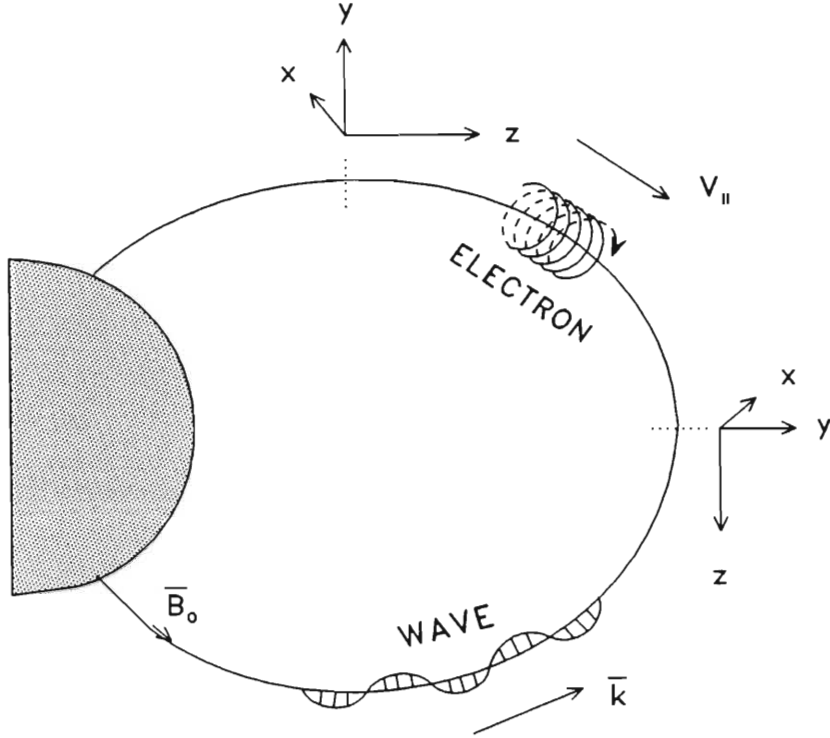


Figure A.1: Coordinate system for the equations of motion. The z-axis is everywhere aligned with the magnetic field

$$\mathbf{F} = q(\mathbf{E}_w \times \mathbf{B}_w) \quad (\text{A.3})$$

where $\mathbf{v} = \mathbf{v}_{\parallel} + \mathbf{v}_{\perp}$ is the total velocity of the particle. \mathbf{F} can be separated into its components parallel and perpendicular to \mathbf{B}_0 , and making use of the fact that both \mathbf{E}_w and \mathbf{B}_w are perpendicular to \mathbf{k} and \mathbf{B}_0 equation A.3 can be written

$$\mathbf{F}_{\parallel} = -e(\mathbf{v}_{\perp} \times \mathbf{B}_w) \quad ; \quad \mathbf{F}_{\perp} = -e(\mathbf{E}_w + \mathbf{v}_{\parallel} \times \mathbf{B}_w) \quad (\text{A.4})$$

With the coordinate system as given in Figure A.1 and using (A.4), the acceleration induced along \mathbf{v}_{\perp} and \mathbf{v}_{\parallel} by the wave can be written as

$$\left(\frac{dv_{\parallel}}{dt}\right)_{wave} = -\frac{e}{m} |\mathbf{v}_{\perp}| \times |\mathbf{B}_w| = \left(\frac{e}{m} B_w\right) v_{\perp} \sin \phi \quad (\text{A.5})$$

$$\left(\frac{dv_{\perp}}{dt}\right)_{wave} = -\frac{e}{m} |\mathbf{E}_w| - \frac{e}{m} |\mathbf{v}_{\parallel}| \times |\mathbf{B}_w| = \left(\frac{e}{m} E_w\right) \sin \phi - \left(\frac{e}{m} B_w\right) v_{\parallel} \sin \phi \quad (\text{A.6})$$

where ϕ is the angle between \mathbf{v}_{\perp} and $-\mathbf{B}_w$ as shown in Figure A.2.

The equations A.6 and A.5 completely describe the effect of the wave on the two particle velocity components. Both dv_{\parallel}/dt and dv_{\perp}/dt are proportional to $\sin \phi$,

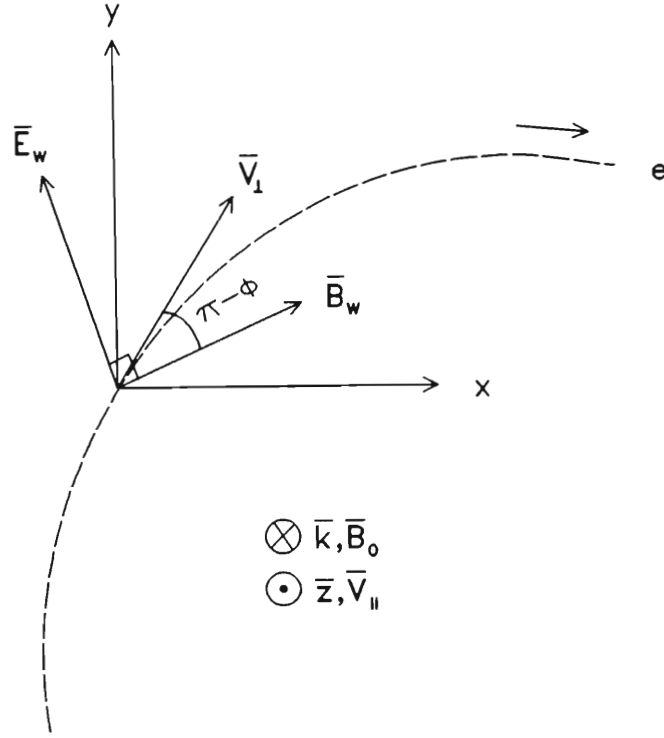


Figure A.2: Coordinate system for the orbit of an electron in the x-y plane

which shows that whether or not there is any integrated cumulative change in v_{\parallel} and v_{\perp} depends on the variation of ϕ . The equation for the rate of change of ϕ can be written as

$$\frac{d\phi}{dt} = (\omega_H - \omega - kv_{\parallel}) - \left(\frac{eB_w}{m}\right) v_{\parallel} \frac{\cos\phi}{v_{\perp}} - \left(\frac{eB_w}{m}\right) \frac{\cos\phi}{v_{\perp}} \quad (\text{A.7})$$

where the first term in the right in (A.7) is the difference between the doppler-shifted wave frequency and the particle's own gyrofrequency, which by definition is the rate of change of ϕ to first order. The second and third terms are the phase changes due to centripetal acceleration of the particle from $\mathbf{v}_{\parallel} \times \mathbf{B}_w$ and \mathbf{E}_w forces. This centripetal acceleration affects the gyromotion of the particle so that the angular frequency of oscillation about the magnetic field varies slightly from the gyrofrequency ω_H .

Equations (A.5) and (A.6) take account only of the wave induced variations in v_{\parallel} and v_{\perp} . These quantities however also vary due to their normal trapped motion along the ambient inhomogenous magnetic field, as given by (2.13) and (A.2). Superimposing these "ambient" variations on (A.5) and (A.6), using $B_o = \omega_H m/q$, $|E_w| = |\omega/k B_w|$ and combining terms the equations of motion are obtained:

$$\dot{v}_{\parallel} = \left(\frac{eB_w}{m} \right) v_{\perp} \sin \phi - \frac{v_{\perp}^2}{2\omega_H} \frac{d\omega_H}{dz} \quad (\text{A.8})$$

$$\dot{v}_{\perp} = \left(\frac{eB_w}{m} \right) \left(v_{\parallel} + \frac{\omega}{k} \right) \sin \phi + \frac{v_{\perp} v_{\parallel}}{2\omega_H} \frac{d\omega_H}{dz} \quad (\text{A.9})$$

$$\dot{\phi} = (\omega_H - \omega - kv_{\parallel}) - \left(\frac{eB_w}{m} \right) \left(v_{\parallel} + \frac{\omega}{k} \right) \frac{\cos \phi}{v_{\perp}} \quad (\text{A.10})$$

where “.” represents differentiation with respect to time. The quantities ω_H and k are functions of the magnetic field and hence z , the distance along the field line. The derivation presented here follows that of [Inan, 1977]. Equations (A.8) to (A.10) in whole or in part have been used to study VLF wave particle interactions by many authors (see [Inan et al., 1978] and references therein).

A.2 The Relativistic Correction

Equations (A.8) to (A.10) here are for the non-relativistic case. The relativistic correction to the resonance condition has been derived in section 5.1. ω_H in equation A.10 is replaced by ω_H/γ , but not in equations A.8 and A.9, since there ω_H refers to electrons of the cold background plasma. Further the first two terms in equations A.8 and A.9 and the last term in equation A.10 have to be modified, since they contain the wave force acting on the relativistic electron: m has to be replaced by $m\gamma$. The equations of motion can then be simply re-written

$$\frac{dv_{\parallel}}{dt} = \left(\frac{eB_w}{m\gamma} \right) v_{\perp} \sin \phi - \frac{v_{\perp}^2}{2\omega_H} \frac{d\omega_H}{dz} \quad (\text{A.11})$$

$$\frac{dv_{\perp}}{dt} = \left(\frac{eB_w}{m\gamma} \right) \left(v_{\parallel} + \frac{\omega}{k} \right) \sin \phi + \frac{v_{\perp} v_{\parallel}}{2\omega_H} \frac{d\omega_H}{dz} \quad (\text{A.12})$$

$$\frac{d\phi}{dt} = \left(\frac{\omega_H}{\gamma} \right) - \omega - kv_{\parallel} - \left(\frac{eB_w}{m\gamma} \right) \left(v_{\parallel} + \frac{\omega}{k} \right) \frac{\cos \phi}{v_{\perp}} \quad (\text{A.13})$$

A.3 Interpretation of Terms in Equations of Motion

The entire physics of the interaction is represented by equations (A.8) to (A.10).

The first terms in (A.8) and (A.9) are due to the wave-induced longitudinal and transverse forces ($\mathbf{v}_{\perp} \times \mathbf{B}_w$ and $\mathbf{v}_{\parallel} \times \mathbf{B}_w + \mathbf{E}_w$), while the additional terms give the adiabatic variations of v_{\parallel} and v_{\perp} which are superimposed on the wave perturbations.

The total changes in v_{\parallel} and v_{\perp} are strongly controlled by (A.10) which gives the variation of ϕ . Cumulative changes in v_{\parallel} and v_{\perp} can only occur when both $\dot{\phi}$ and $\ddot{\phi}$ are small.

The last term in (A.10) is the phase change due to the wave term (centripetal acceleration of the particle due to the $\mathbf{v}_{\parallel} \times \mathbf{B}_w + \mathbf{E}_w$ force), which for most magnetospheric parameters is negligible (especially for large pitch angles and small wave amplitudes) [Inan et al., 1978]. However for small wave amplitudes this term becomes dominant as $\alpha < 2^\circ$. It is possible for particles with pitch angles outside this range to be scattered down to these low pitch angles during the interaction. This term must thus be present to describe the physics correctly. “Small” wave amplitude here refers to the amplitude with respect to the background field.

A.4 Total Change in v_{\parallel} and v_{\perp}

To compute the change in pitch angle (and thus the chances of an electron precipitating) the overall changes Δv_{\parallel} and Δv_{\perp} in the motion of an electron has to be found. For given initial conditions ($v_{\parallel o}$, $v_{\perp o}$ and ϕ_o) the equations of motion (A.8) to (A.10) have to be properly integrated over time:

$$\begin{aligned}\Delta v_{\parallel} &= \int_o^{T_I} \dot{v}_{\parallel} dt \\ \Delta v_{\perp} &= \int_o^{T_I} \dot{v}_{\perp} dt\end{aligned}\tag{A.14}$$

Where the subscript o refers to initial time and T_I is the integration time. Ideally the integration should be carried out for $T_I \rightarrow \infty$, but since the resonance condition (2.20) is satisfied only locally for any given particle T_I can be defined over a limited interaction time. When (2.20) is not satisfied, $|\dot{\phi}|$ would be large as is apparent from (A.10), and the wave contributions to \dot{v}_{\parallel} and \dot{v}_{\perp} will be non-cumulative.

The changes in parallel and perpendicular velocity can be viewed as scatterings in velocity space. The point to point and thus total integrated scattering (from equations (A.8) to (A.10)) depend on $v_{\parallel o}$ and $v_{\perp o}$ and the initial phase ϕ_o between v_{\perp} and $-B_o$ at the time at which particles and wave first encounter each other. The scattering further depends on the wave parameters B_w , ω and k ; and the medium parameters ω_H and $d\omega_H/dz$. Away from the equator, for constant frequency, the interaction time is shortened since $d\omega_H/dz$ is large, and the total scattering is smaller. [Dysthe, 1971] has clearly shown that the variation of $d\omega_H/dz$ is the principal factor controlling the interaction time T_I . This justifies the assumption of an interaction region near the equator.

A.5 Method of solution

The equations of motion (A.8) to (A.10) are highly non-linear and it is difficult to evaluate the integrals (A.14) by analytical methods without making restrictive simplifying assumptions. A common approach is to use linear theory [Das, 1971, Ashour-Abdalla, 1972], which computes the perturbations in v_{\parallel} and v_{\perp} by using the field components of the wave at the position of the particle as given by the unperturbed ($B_o = 0$) motion. This approach is applicable for sufficiently low wave amplitudes. [Inan et al., 1978] gives exact criteria under which linear theory can be used.

A more complete approach to the solution of (A.8) to (A.10) is to use a test particle simulation of the interaction. The idea is that the perturbation of the full particle distribution can be inferred by computing the effect of the wave on a sufficient number of particles appropriately distributed in ϕ , v_{\parallel} and v_{\perp} . Although the precipitated flux is the quantity of most interest here, the study of single particle trajectories is important in illustrating the physics of the interaction, in particular, the conditions for strong pitch angle scattering can be established.

A comprehensive computer simulation of the equations of motion has been written which allows one to loop through a range of variables which affect the interaction. The program further allows the calculation of resonance conditions along a field line, keeping either the wave frequency or the particle energy constant. The main integration routine used is a Runge-Kutta 4th-order predictor-corrector algorithm, taken from [Press et al., 1986].

Bibliography

- [Adams, 1990] Adams, C. D. D., *Perturbations in Subionospheric Propagation at VLF*, PhD thesis, University of Otago, Dunedin, New Zealand, July 1990.
- [Adams and Dowden, 1990] Adams, C. D. D. and R. L. Dowden, VLF group delay of lightning-induced electron precipitation echoes from measurements of phase and amplitude perturbations at two frequencies, *Journal of Geophysical Research*, *95*, 2457–2462, March 1990.
- [Adams et al., 1990] Adams, C. D. D., J. B. Brundell, and R. L. Dowden, Trimpi detection and computer aided measurement, *XXIII General Assembly of the URSI, Prague, Czechoslovakia*, September 1990.
- [Angerami and Thomas, 1964] Angerami, J. J. and J. O. Thomas, The distribution of electrons and ions in the earth's exosphere, *Journal of Geophysical Research*, *69*, 4537, 1964.
- [Ashour-Abdalla, 1972] Ashour-Abdalla, M., Amplification of whistler waves in the magnetosphere, *Planetary and Space Science*, *20*, 639, 1972.
- [Barr et al., 1984] Barr, R., M. T. Rietveld, H. Kopka, and P. Stubbe, Effect of a heated patch of auroral ionosphere on VLF radio propagation, *Nature*, *309*, 534–536, June 1984.
- [Bracewell and Bain, 1952] Bracewell, R. N. and W. C. Bain, An explanation of radio wave propagation at 16 Kc/sec in terms of two layers below E layer, *Journal of Atmospheric and Terrestrial Physics*, 216, February 1952.
- [Brinca, 1981] Brinca, A. L., Enhancing whistler wave-electron interaction by the use of specially modulated VLF wave injection, *Journal of Geophysical Research*, *86*, 792–800, February 1981.
- [Brooker et al., 1970] Brooker, H. G., C. M. Crain, and E. C. Field, *Transmission of Electromagnetic waves through normal and disturbed Ionospheres*, Technical Report, Rand Corporation, Santa Monica, California, USA, November 1970.
- [Budden, 1961] Budden, K. J., *Radio Waves in the Ionosphere*, vol. , Cambridge University Press, Cambridge, England, 1st edition, 1961.

- [Carpenter, 1963] Carpenter, D. L., Whistler evidence of a “knee” in the magnetospheric ionisation density profile, *Journal of Geophysical Research*, *68*, 1675, 1963.
- [Carpenter and LaBelle, 1982] Carpenter, D. L. and J. W. LaBelle, A study of whistlers correlated with bursts of electron precipitation near L=2, *Journal of Geophysical Research*, *87*, 4427–4434, June 1982.
- [Carpenter and Park, 1973] Carpenter, D. L. and C. G. Park, On what ionospheric workers should know about the plasmopause-plasmasphere, *Reviews of Geophysics and Space Physics*, *11*, 133–154, February 1973.
- [Carpenter and Smith, 1964] Carpenter, D. L. and R. L. Smith, Satellite observations of equatorial electron densities, *Reviews of Geophysics*, *2*, 415, 1964.
- [Carpenter et al., 1968] Carpenter, D. L., F. Walter, R. E. Barrington, and D. J. McEwan, Alouette 1 and 2 observations of abrupt changes in whistler rate and VLF noise variations at the plasmopause - a satellite-ground study, *Journal of Geophysical Research*, *73*, 2929–2940, May 1968.
- [Carpenter et al., 1984] Carpenter, D. L., U. S. Inan, M. L. Trimpi, R. A. Helliwell, and J. P. Katsufakis, Perturbations of subionospheric LF and MF signals due to whistler-induced electron precipitation bursts, *Journal of Geophysical Research*, *89*, 9857–9862, November 1984.
- [Carpenter et al., 1985] Carpenter, D. L., U. S. Inan, E. W. Paschal, and A. J. Smith, A new VLF method for studying burst precipitation near the plasmopause, *Journal of Geophysical Research*, *90*, 4383–4388, May 1985.
- [Chang and Inan, 1983] Chang, H. C. and U. S. Inan, Quasi-relativistic electron precipitation due to interactions with coherent VLF waves in the magnetosphere, *Journal of Geophysical Research*, *88*, 318–328, January 1983.
- [Chang and Inan, 1985] Chang, H. C. and U. S. Inan, Lightning-induced electron precipitation from the magnetosphere, *Journal of Geophysical Research*, *90*, 1531–1541, 1985.
- [Chen, 1974] Chen, F. F., *Introduction to Plasma Physics*, vol. , Plenum Press, New York, USA, 1st edition, 1974.
- [Das, 1971] Das, A. C., A mechanism for vlf emissions, *Journal of Geophysical Research*, *76*, 6915, 1971.
- [Datlowe and Imhof, 1990] Datlowe, D. W. and W. L. Imhof, Cyclotron resonance precipitation of energetic electrons from the inner magnetosphere, *Journal of Geophysical Research*, *95*, 6477–6491, May 1990.
- [Doolittle, 1982] Doolittle, J. H., *Modification of the Ionosphere by VLF Wave-Induced Electron Precipitation*, Technical Report, Stanford University, Radioscience Laboratory, Stanford Electronics Labs., Stanford, California, USA, 1982.

- [Dowden and Adams, 1988] Dowden, R. L. and C. D. D. Adams, Phase and amplitude perturbations on subionospheric signals explained in terms of echoes from lightning-induced electron precipitation, *Journal of Geophysical Research*, *93*, 11543–11550, October 1988.
- [Dowden and Adams, 1989] Dowden, R. L. and C. D. D. Adams, Phase and amplitude perturbations on the NWC signal at Dunedin from lightning-induced electron precipitation, *Journal of Geophysical Research*, *94*, 497–503, January 1989.
- [Dowden et al., 1991] Dowden, R. L., C. D. D. Adams, and J. Brundell, Coherent reception of trimpis on a seven-element, 1200km array, *XXth General Assembly of IUGG, Vienna, Austria*, August 1991.
- [Dysthe, 1971] Dysthe, K. B., Some studies of triggered whistler emissions, *Journal of Geophysical Research*, *76*, 6915, 1971.
- [Ferguson, 1980] Ferguson, J. A., *Ionospheric Profiles for Predicting Nighttime VLF/LF Propagation*, Technical Report, Naval Ocean Systems, Command, San Diego, California, USA, 1980.
- [Friedel, 1987] Friedel, R. H. W., *Determination of Duct Exit Points using Goniometer Data*, Technical Report, University of Natal, Durban, South Africa, September 1987.
- [Friedel, 1991] Friedel, R. H. W., *The Durban OMSKI: System and Software*, Technical Report, University of Natal, Durban, South Africa, December 1991.
- [Friedel and Hughes, 1990] Friedel, R. H. W. and A. R. W. Hughes, Characteristics and frequency of occurrence of trimpis events recorded during 1982 at SANAE, Antarctica, *Journal of Atmospheric and Terrestrial Physics*, *52*, 329–339, May 1990.
- [Friedel and Smith, 1991] Friedel, R. H. W. and A. J. Smith, A standard format for VLF spectrographs: “VLF Quicklook” - a proposal to VERSIM, *IAGA/URSI Joint Working Group VERSIM Newsletter*, 10–12, October 1991.
- [Garrison, 1986] Garrison, J. D., Status of the worldwide OMEGA navigation system, *NAVIGATION: Journal of the Institute of Navigation*, *33*, 168–179, October 1986.
- [Hargreaves, 1979] Hargreaves, J. K., *The Upper Atmosphere and Solar-Terrestrial Relations*, vol. , Van Nostrand Reinhold Co. Ltd., Workingham, Berkshire, England, 1st edition, 1979.
- [Hayakawa and Tanaka, 1978] Hayakawa, M. and Y. Tanaka, On the propagation of low-latitude whistlers, *Reviews of Geophysics and Space Physics*, *16*, 111–123, February 1978.

- [Helliwell, 1965] Helliwell, R. A., *Whistlers and Related Ionospheric Phenomena*, vol. Stanford University Press, Stanford, California, USA, 1st edition, 1965.
- [Helliwell et al., 1973] Helliwell, R. A., J. P. Katsufakis, and M. L. Trimpi, Whistler-induced amplitude perturbations in VLF propagation, *Journal of Geophysical Research*, *78*, 4679–4688, August 1973.
- [Hurren et al., 1986] Hurren, P. J., A. J. Smith, D. L. Carpenter, and U. S. Inan, Burst precipitation induced perturbations on multiple VLF propagation paths in Antarctica, *Annales Geophysicae*, *4*, 311–318, May 1986.
- [Imhof et al., 1981] Imhof, W. L., E. E. Gaines, and J. B. Reagan, Observations of multiple, narrow energy peaks in electrons precipitating from the inner radiation belt and their implications for wave particle interactions, *Journal of Geophysical Research*, *86*, 1591–1595, March 1981.
- [Imhof et al., 1985] Imhof, W. L., E. E. Gaines, H. D. Voss, J. B. Reagan, D. W. Datlowe, J. Mobilia, R. A. Helliwell, U. S. Inan, J. Katsufakis, and R. G. Joiner, Results from the SEEP active space plasma experiment: Effects on the ionosphere, *Radio Science*, *20*, 511–518, May 1985.
- [Inan, 1977] Inan, U. S., *Non-Linear Gyroresonant Interactions of Energetic Particles and Coherent VLF Waves in the Magnetosphere*, Technical Report, Stanford University, Radioscience Laboratory, Stanford Electronics labs., Stanford, California, USA, August 1977.
- [Inan and Carpenter, 1987] Inan, U. S. and D. L. Carpenter, Lightning-induced electron precipitation events observed at $L \sim 2.4$ as phase and amplitude perturbations on subionospheric VLF signals, *Journal of Geophysical Research*, *92*, 3293–3303, April 1987.
- [Inan et al., 1978] Inan, U. S., T. F. Bell, and R. A. Helliwell, Nonlinear pitch angle scattering of energetic electrons by coherent VLF waves in the magnetosphere, *Journal of Geophysical Research*, *83*, 3235–3253, July 1978.
- [Inan et al., 1982] Inan, U. S., T. F. Bell, and H. C. Chang, Particle precipitation induced by short-duration VLF waves in the magnetosphere, *Journal of Geophysical Research*, *87*, 6243–6264, August 1982.
- [Inan et al., 1985] Inan, U. S., D. L. Carpenter, R. A. Helliwell, and J. P. Katsufakis, Subionospheric VLF/LF phase perturbations produced by lightning-whistler induced particle precipitation, *Journal of Geophysical Research*, *90*, 7457–7469, August 1985.
- [Inan et al., 1988a] Inan, U. S., W. C. Burgess, T. G. Wolf, D. C. Shater, and R. E. Orville, Lightning-associated precipitation of MeV electrons from the inner radiation belt, *Geophysical Research Letters*, *15*, 172–175, February 1988a.

- [Inan et al., 1988b] Inan, U. S., D. C. Shafer, W. Y. Yip, and R. E. Orville, Subionospheric VLF signatures of nighttime D region perturbations in the vicinity of lightning discharges, *Journal of Geophysical Research*, *93*, 11455–11472, October 1988b.
- [Inan et al., 1988c] Inan, U. S., T. G. Wolf, and D. L. Carpenter, Geographic distribution of lightning-induced electron precipitation observed as VLF/LF perturbation events, *Journal of Geophysical Research*, *93*, 9841–9853, September 1988c.
- [Inan et al., 1989] Inan, U. S., M. Walt, H. D. Voss, and W. L. Imhof, Energy spectra and pitch angle distributions of lightning induced electron precipitation: Analysis of an event observed on the S81-1(SEEPEX) satellite, *Journal of Geophysical Research*, *94*, 1379–1401, February 1989.
- [Inan et al., 1991] Inan, U. S., T. F. Bell, and J. V. Rodriguez, Heating and ionisation of the lower ionosphere by lightning, *Geophysical Research Letters*, *18*, 705–708, April 1991.
- [Kennel and Petschek, 1966] Kennel, C. F. and H. Petschek, Limit on stably trapped particle fluxes, *Radio Science*, *1*, 269, 1966.
- [Kent, 1970] Kent, G. S., Measurement of ionospheric movements, *Reviews of Geophysics, Space Physics*, *8*, 229, 1970.
- [Ladwig and Hughes, 1989] Ladwig, J. M. and A. R. W. Hughes, An asymmetry in the direction of arrival of whistlers at SANAE, Antarctica, *Journal of Atmospheric and Terrestrial Physics*, *51*, 61–65, February 1989.
- [Leyser et al., 1984] Leyser, T. B., U. S. Inan, D. L. Carpenter, and M. L. Trimpf, Diurnal variation of burst precipitation effects on subionospheric VLF/LF near L=2, *Journal of Geophysical Research*, *89*, 9139, 1984.
- [Liemohn, 1961] Liemohn, H. B., *Radiation Belt Particle Orbits*, Technical Report, Boeing Scientific Labs., June 1961.
- [Lohrey and Kaiser, 1979] Lohrey, B. and A. B. Kaiser, Whistler induced anomalies in VLF propagation, *Journal of Geophysical Research*, *84*, 5211–5130, September 1979.
- [Lyons and Thorne, 1973] Lyons, L. R. and R. M. Thorne, Equilibrium structure of radiation belt electrons, *Journal of Geophysical Research*, *78*, 2142–2149, May 1973.
- [Lyons and Williams, 1984] Lyons, L. R. and D. J. Williams, *Quantitative Aspects of Magnetospheric Physics*, vol. , D. Reidel Publishing Company, Dordrecht/Boston/Lancaster, 1st edition, 1984.
- [Maggs, 1976] Maggs, J. E., Coherent generation of VLF hiss, *Journal of Geophysical Research*, *81*, 1707–1724, April 1976.

- [Mitra, 1975] Mitra, A. P., D-region in disturbed conditions, including flares and energetic particles, *Journal of Atmospheric and Terrestrial Physics*, 37, 895, 1975.
- [Morfitt and Shellman, 1976] Morfitt, D. and C. H. Shellman, *MODESRCH, an Improved Computer Model for Obtaining ELF/VLF/LF Mode Constants in an Earth-Ionosphere Waveguide*, Technical Report, Naval Electronics Laboratory Center, San Diego, California, USA, October 1976.
- [Pappert and Snyder, 1972] Pappert, R. A. and F. P. Snyder, Some results of a mode-conversion programme for VLF, *Radio Science*, 7, 913, 1972.
- [Park, 1972] Park, C. G., *Methods of Determining Electron Concentrations in the Magnetosphere from Nose Whistlers*, Technical Report, Stanford University, Radioscience Laboratory, Stanford Electronics labs., Stanford, California, USA, 1972.
- [Pekrides, 1989] Pekrides, H., *Numerical Modelling of PC 4–5 Compressional Pulsations in the Magnetosphere*, Master's thesis, University of Natal, Durban, South Africa, January 1989.
- [Poterma and Rosenberg, 1973] Poterma, T. A. and T. J. Rosenberg, VLF propagation disturbances and electron precipitation at mid-latitudes, *Journal of Geophysical Research*, 78, 1572–1580, April 1973.
- [Poulsen et al., 1990] Poulsen, W. L., T. F. Bell, and U. S. Inan, Three-dimensional modelling of subionospheric VLF propagation in the presence of localised D-region perturbations associated with lightning, *Journal of Geophysical Research*, 95, 2355–2366, March 1990.
- [Press et al., 1986] Press, W. H., B. P. Flannery, S. A. Teukolsky, and W. T. Vetterling, *Numerical Recipes - The Art of Scientific Computing*, vol. , Cambridge University Press, Cambridge, United Kingdom, 1st edition, 1986.
- [Ratcliffe, 1959] Ratcliffe, J. . A., *The Magneto-Ionic Theory and its Application to the Ionosphere*, vol. , Cambridge University Press, Cambridge, England, 1st edition, 1959.
- [Ratcliffe, 1972] Ratcliffe, J. A., *An Introduction to the Ionosphere and Magnetosphere*, vol. , Cambridge University Press, Cambridge, England, 1st edition, 1972.
- [Rees, 1963] Rees, M. H., Auroral ionisation and excitation by incident energetic electrons, *Planetary and Space Science*, 1209–1218, November 1963.
- [Rees, 1969] Rees, M. H., Auroral electrons, *Space Science Reviews*, 413–441, October 1969.
- [Schulz and Lanzerotti, 1973] Schulz, M. and L. J. Lanzerotti, *Particle Diffusion in the Radiation Belts*, vol. , Springer Co., New York, 1st edition, 1973.

- [Singh, 1976] Singh, B., On the ground observation of whistlers at low latitudes, *Journal of Geophysical Research*, *81*, 2429, 1976.
- [Smith, 1961] Smith, R. L., Guiding of whistlers in a homogenous medium, *Journal of Research of the national Bureau of Standards, USA*, *64D*, 505–508, September 1961.
- [Smith and Cotton, 1990] Smith, A. J. and P. D. Cotton, The trimpi effect in Antarctica: observations and models, *Journal of Atmospheric and Terrestrial Physics*, *52*, 341–355, May 1990.
- [Smith et al., 1990] Smith, A. J., J. Robertson, P. D. Cotton, C. D. D. Adams, and R. L. Dowden, Simultaneous multi-frequency measurements of amplitude and phase trimpis on multiple paths over the South Atlantic, *XXIII General Assembly of the URSI, Prague, Czechoslovakia*, September 1990.
- [Smith et al., 1991a] Smith, A. J., D. L. Carpenter, Y. Corcuff, J. P. S. Rash, and E. A. Bering, The longitudinal dependence of whistler and chorus characteristics observed on the ground near L=4, *Journal of Geophysical Research*, *96*, 275–284, January 1991a.
- [Smith et al., 1991b] Smith, A. J., J. R. Robertson, and P. D. Cotton, Lightning-induced electron burst precipitation at L=2–4, in the vicinity of the Antarctic Peninsula, *XXth General Assembly of IUGG, Vienna, Austria*, August 1991b.
- [Stephenson, 1989] Stephenson, J. A. E., *SANAE Aurorae and Whistlers*, Master's thesis, University of Natal, Durban, South Africa, January 1989.
- [Thomson, 1976] Thomson, N. R., Electric fields from whistler-mode doppler shifts, *Planetary and Space Science*, *24*, 531–543, 1976.
- [Thorne et al., 1973] Thorne, R. M., E. J. Smith, R. K. Burton, and R. F. Holzer, Plasmaspheric hiss, *Journal of Geophysical Research*, *78*, 1581–1596, April 1973.
- [Tolstoy et al., 1986] Tolstoy, A., T. J. Rosenberg, U. S. Inan, and D. L. Carpenter, Model predictions of subionospheric VLF signal perturbations resulting from localised electron precipitation-induced ionisation enhancement regions, *Journal of Geophysical Research*, *91*, 13473–13482, December 1986.
- [Tsuruda et al., 1982] Tsuruda, K., S. Machida, T. Terasawa, A. Nishida, and K. Maezawa, High spatial attenuation of the Siple transmitter signal and natural VLF chorus observed at ground-based chain stations near Roberval, Quebec, *Journal of Geophysical Research*, *87*, 742, 1982.
- [Vampola, 1983] Vampola, A. L., Observations of VLF transmitter-induced depletions of inner zone electrons, *Geophysical Research Letters*, *10*, 619–622, August 1983.

- [Volland, 1982] Volland, H., *Handbook for Atmospheric*, vol. I & II, CRC Press, Inc., Boca Raton, Florida, USA, 1st edition, 1982.
- [Wait, 1970] Wait, J. R., *Electromagnetic Waves in Stratified Media*, vol. , Pergamon Press, New York, USA, 2nd edition, 1970.
- [Zmuda and Poterma, 1972] Zmuda, A. J. and T. A. Poterma, Bombardment of the polar-cap ionosphere by solar cosmic rays, *Reviews of Geophysics and Space Physics*, 10, 981, October 1972.